COMPUTATIONAL DESIGN OF COMPOSITIONALLY GRADED ALLOYS

A Dissertation

by

TANNER QUINN KIRK

Submitted to the Office of Graduate and Professional Studies of
Texas A&M University
in partial fulfillment of the requirements for the degree of

DOCTOR OF PHILOSOPHY

Chair of Committee,	Richard J. Malak
Co-Chair of Committee,	Raymundo Arróyave
Committee Members,	Ibrahim Karaman
	Douglas Allaire
Head of Department,	Andreas A. Polycarpou

December 2020

Major Subject: Mechanical Engineering

ABSTRACT

In this work, a new computational methodology is presented for the design of compositionally graded alloys. Compositionally graded alloys are a class of functionally graded materials, or materials which exhibit spatially varying properties. While the introduction of additive manufacturing has accelerated interest in these materials, there are many challenges that impede their development like the formation of deleterious phases and material compositions that are incompatible with manufacturing processes. Previous design methods have attempted to design gradients that avoid these issues, but such methods have been limited to the analysis and interpretation of two-dimensional diagrams and are therefore hindered by the limits of human visualization and ideation.

The proposed methodology is made possible by the novel formulation of gradient design as a path planning problem. This formulation allows the use of path planning algorithms to optimize gradient paths in composition space. Such algorithms can optimize gradients with any number of constituent elements to meet specified design requirements or objectives. To make the gradient design problem tractable for such algorithms, surrogate modeling techniques are employed to represent design constraints and objectives. Constraints, like deleterious phase formation, can be predicted by CALPHAD software and then modeled by a machine learning classifier. Similarly, regression models can be trained to evaluate cost functions in an efficient manner.

Several unique problem formulations are demonstrated to showcase the advantages of the methodology in gradient design. Among these are constraints to avoid deleterious phase regions and other regions of the state space with poor predicted manufacturability. Common cost functions in the path planning community, like path length and obstacle clearance, are shown to be useful for some problems, while including constraint violation as penalty term is demonstrated to satisfy constraints that might otherwise be unachievable. Lastly, a novel cost function is proposed to design gradients with monotonic properties, which can achieve nearly any bounded property distribution on a gradient part. All proposed problem formulations are demonstrated in the design of authentic compositionally graded alloys and experiments are used to validate predicted results.

ACKNOWLEDGMENTS

Thanks are owed to my advisors, Richard Malak and Raymundo Arróyave, for inspiring the design methodology presented in this dissertation and for their advise, support, and contributions to its creation. I would also like to thank Olga Eliseeva, Nick Barta, and Ibrahim Karaman for the challenging work of realizing the materials we designed and for invaluable input on the realities of manufacturing. Thanks also to Douglas Allaire and other members of the engineering and systems design community at Texas A&M for their input on many of the optimization and design methods contained in this dissertation.

I would like to thank collaborators at NASA JPL for sharing their unrivaled knowledge in compositionally graded alloys, including Richard Otis, Samad Firdosy, Peter Dillon, J.P. Borgonia, Scott Roberts, Doug Hofmann, Andrew Shapiro, and many others. Thanks also to collaborators at QuesTek Innovations LLC, including Dana Frankel, Pin Lu, Changning Niu, Marie Thomas, and colleagues, for contributing their experience in materials design.

Special thanks to my fellow graduate students, past and present, of which there are too many to name, who have inspired many facets of my research through their own work and our enlightening discussions. Finally, my sincere thanks to my friends and family for their endless support and encouragement.

CONTRIBUTORS AND FUNDING SOURCES

Contributors

This work was supported by a dissertation committee consisting of Professors Richard Malak [advisor], Raymundo Arróyave [co-advisor], Ibrahim Karaman, and Douglas Allaire of the Department of Mechanical Engineering. Professors Arróyave and Karaman also have appointments in the Department of Materials Science and Engineering.

Experiments discussed in Chapters 4, 5, and 6 were conducted and analyzed by Olga Eliseeva, Nick Barta, and colleagues in the Department of Materials Science and Engineering .

The Hot Cracking Susceptibility criterion used in Chapter 5 was provided by QuesTek Innovations LLC.

All other work conducted for the dissertation was completed by the student independently.

Funding Sources

Graduate study was partially supported by a fellowship from the National Science Foundation through the project NRT-DESE: Data-Enabled Discovery and Design of Energy Materials (D3EM), NSF-DGSE-1545403.

Work presented in Chapter 5 was partially funded by the U.S. Department of Energy under Award #DE-SC0020032.

Work presented in Chapter 6 was carried out at the Jet Propulsion Laboratory, California Institute of Technology, and was sponsored by the JPL Summer Internship Program, the JPL Space Technology Office, and the National Aeronautics and Space Administration (80NM0018D0004).

NOMENCLATURE

Abbreviations

BCC	Body Centered Cubic
BCT	Body Centered Tetragonal
BSE	Backscattered Electron
CALPHAD	CALculation of PHAse Diagram
CSA	Constraint Satisfaction Algorithm
CTE	Coefficient of Thermal Expansion
DED	Directed Energy Deposition
FCC	Face Centered Cubic
FGM	Functionally Graded Material
HCS	Hot Cracking Susceptibility
LOD	Lack of Decrease
LOI	Lack of Increase
LOM	Lack of Monotonicity
MMTO	Multi-Material Topology Optimization
PRM	Probabilistic Roadmap
RMSE	Root Mean Square Error
RRT	Rapidly-exploring Random Tree
SEM	Scanning Electron Microscopy
SS	Stainless Steel
SVM	Support Vector Machine

SVDD	Support Vector Data Description
TCHEA	Thermo-Calc High Entropy Alloy
WDS	Wavelength Dispersive Spectroscopy
XRD	X-ray Diffraction

Mathematical Symbols

c	Cost function that relates a path to a measure of quality
d	Dimensionality of the state space
d_{avg}	Average distance to the nearest obstacle boundary
f	Molar phase fraction
l	Length of a path in state space
N	Number of elements in the state space
N_{fn}	Number of false negatives
N_{fp}	Number of false positives
N_{tn}	Number of true negatives
N_{tp}	Number of true positives
n_{max}	Maximum number of nodes allowed before forced removal
n_{nodes}	Number of nodes in the tree
P	Arbitrary process parameter
p	Arbitrary material property
R^2	Coefficient of determination
r	The ratio of the length of path σ_1 to the length of the concatenation of paths σ_1 and σ_2
T	Temperature
w	Weighting parameter to control the effect of path length in the cost function
x_i	Composition of element i
y	Position on a gradient part
Z^d	State space of the path planning problem
Z_{free}	Obstacle-free region
Z_{near}	Nearby region in state space

Z_{obs}	Obstacle region
z	Point in the state space of the path planning problem
z_{init}	Initial point in path
z_{goal}	Goal point in path
z_{nearest}	Nearest sample in state space
z_{new}	New point to be added to the tree
z_{parent}	Parent node of point in tree
z_{rand}	Randomly generated sample in state space
α	Index of a point in the path
$\Delta T_{\text{solidification}}$	Solidification range
$\Delta y_{i \to i+1,\text{min}}$	The minimum length in physical space needed to print an arbitrary segment of a gradient, subject to constraints
λ	Allowable phase fraction
σ	Continuous path in the state space
σ_{best}	Feasible path that minimizes the cost function
τ	Tree composed of vertices and edges in state space

TABLE OF CONTENTS

Page

LIST OF FIGURES

FIGURE Page

LIST OF TABLES

TABLE Page

1. INTRODUCTION

1.1 Research Overview

This dissertation presents a novel computational methodology for the design of compositionally graded alloys. The presented methodology employs computational materials modeling along with algorithms from the machine learning and motion planning communities to address the common challenges associated with compositional gradients. Prior attempts at manufacturing compositionally graded alloys have been mired by the formation of deleterious phases, sharp changes in material properties, or gradient compositions that are ill-suited for additive manufacturing. While phase diagrams and designer intuition have been used to design gradients that avoid some of these issues, these approaches are limited by human visualization and ideation. The proposed methodology can overcome these limitations by leveraging computational techniques to plan gradients involving many constituent elements that satisfy any number of constraints and are optimized according to design objectives.

This chapter first introduces Functionally Graded Materials, explaining their attractive potential in engineering design and detailing many ways of achieving functional gradients. A thorough review is then given on the state-of-the-art of compositionally graded alloys, with special focus paid to the complications that motivate the present research and prior attempts at surmounting them. Lastly, the goals of this research and its contributions to the greater community are summarized.

1.2 Functionally Graded Materials

Functionally Graded Materials (FGMs) are materials that exhibit a change or gradient in their properties along their spatial dimensions [7]. These spatial property gradients can be exploited to satisfy conflicting performance requirements in the same part. Consequently, FGMs are promising materials for complex systems or extreme environments where demanding constraints on material properties like heat resistance, strength, ductility, density, and cost are unlikely to be met by a single material. In other words, material property requirements are often seen as global variables

for a single-material part, but FGMs enable multi-material solutions that can increase performance by optimizing material properties locally.

The first FGMs were metal-ceramic composites, developed in Japan in the 1980s for aerospace applications that required both ultraheat resistance and high mechanical strength [8, 9]. These metal-ceramic composites were created via various specialized coating, plating, and powder metallurgy processes [8], which did not easily translate to other material combinations. For over a decade, graded metal-ceramic composites were the only well-studied class of FGMs. However, the development of additive manufacturing techniques in the 2000s led to unprecedented control over material composition and geometry and, with that control, many new classes of FGMs [10, 11, 12, 13, 14]. By its very nature, the additive manufacturing process enables changes in material on a layer-by-layer basis. In these processes, material composition can be easily graded by incorporating multiple sources of materials (e.g. powder feeders) and controlling their mixture. Methods such as fused deposition modeling and directed energy deposition have been used to demonstrate functional grading in this manner [14].

Similar to metal-ceramic composites, other graded composites in ceramics and polymers have also been studied [14]. Graded composites like these maintain distinct separation in material phases throughout the graded region. This phase separation is less distinct in materials like compositionally graded alloys [1]. Due to the tendency of metals to be mutually soluble, new phases are formed in the gradient regions of these materials which can often present challenges to functional grading.

In addition to grading material composition, functional grading can also be achieved by changing the geometry, porosity, or lattice structure of a material [11, 12, 13, 15]. While consisting of a single material composition, structurally graded materials offer the capability to increase strength and stiffness where needed while minimizing density elsewhere. Such materials are commonly seen in nature within the cellular structure of bones, but researchers have recently developed architected materials with structures controlled at even the microscale [15].

The rest of this section reviews the major classes of FGMs, other than compositionally graded alloys, and some associated design methods. Given their history as the first engineered FGMs,

graded composites, in which material phases remain distinct, are reviewed first, including graded metal-ceramic, ceramic and polymer composites. Examples of structural grading are then given, including architected materials and structural variation induced through process control. A more thorough review of compositionally graded alloys can be found in Section 1.3.

1.2.1 Graded Composites

1.2.1.1 Metal-Ceramic Composites

The first use of the term "Functionally Graded Material" is often credited to the work of Niino et al. in the 1980s [8, 9]. These earliest FGMs combined the thermal and corrosion resistant properties of ceramics with the high strength and ductility of metals in order to survive in extreme aerospace and nuclear environments. Previous coating technologies produced a discrete boundary between ceramic and metal and consequently a step change in material properties. This discontinuity often led to crack initiation which comprised the integrity of the bond and resulted in delamination. To solve this problem, Niino et al. demonstrated that a gradient composite with a smooth change in properties between two materials will reduce the maximum stress [8]. In the formulation of the stress distribution, the graded properties were assumed to be a rule-of-mixtures combination of the pure material properties.

In Niino et al.'s 1988 patent three examples of composite FGMs were given [8]. The first example is a ceramic gradient between C and SiC with dispersed TiC particles in the interlayers. A second example is presented of a graded coating between $ZrO_20.9Y_2O_3$ and Ni16Cr6Al0.6Y deposited on a nickel-based superalloy substrate. Lastly, an FGM between Ni and PSZ ceramic is created by sintering powders mixed in graded ratios. All of these examples involve particulates of one material embedded in a matrix of a different material and, consequently, discrete separation between constituent materials in all regions. As such, the properties in the graded regions of these composites can be easily predicted from the volume fraction of each material.

In the years after the introduction of these FGMs, many more examples of graded metal-ceramic composites were produced [16, 17, 18, 19]. As interest in these materials grew, much

work was done to model the thermomechanical behavior of FGMs [20, 17, 21]. Later works used these models and Finite Element Analysis to optimize the distribution of volume fraction within an FGM of fixed geometry [22, 23]. However, optimized designs remained largely unidirectional as they were constrained by limited manufacturing methods. The emergence of additive manufacturing greatly expanded manufacturing capabilities and therefore the design space available for functional grading. With this expansion, design methods were developed to optimize volume fraction in two and three dimensions [24, 25, 26, 27].

1.2.1.2 Graded Ceramic Composites

In addition to grading ceramics with metals, many researchers have investigated graded composites between multiple ceramic materials [28, 29, 30, 31]. Mott and Evans [28] used ink jet printing to print a gradient between zirconia and alumina. Mohebi and Evans [29] expanded on the technique to develop an ink jet system capable of printing a variety of graded ceramic compositions in three dimensions. Leu et al. [30] developed a novel freeze form extrusion method to manufacture graded ceramics from blended pastes and demonstrated another gradient between zirconia and alumina. Other examples of graded ceramics have been used to create thermal coatings, turbine blades, lightweight armors, and biomedical devices [31].

1.2.1.3 Graded Polymer Composites

As one of the first and most easily accessible additive manufacturing techniques, polymer 3D printing has been widely studied for over two decades. Polymer materials have also been commonly used as the matrix materials in many composites (e.g. carbon fiber reinforced polymers). Additionally, polymers are not often mutually soluble and can be cured by a variety of stimuli like heat or light. These characteristics trivialize the coexistence of distinct material phases and therefore the manufacturing of multimaterial parts. It is no surprise then that researchers have explored functional grading in polymers extensively [13, 14, 32, 33].

Chung et al. [32] used selective laser sintering to print functionally graded nylon by controlling the volume fraction of embedded silica nanoparticles. A stereolithography technique based on

masking was developed by Zhou et al. [33] to produce multimaterial parts that can grade in color, mechanical properties, or electrical conductivity. Material jetting systems, like the Stratsys PolyJet systems, are capable of printing a wide array of various polymers in a single part. These materials range in color, transparency, and mechanical properties, and enable a diverse set of potential FGMs [34].

1.2.2 Structural Grading

1.2.2.1 Graded Cellular or Architected Materials

In addition to changing material composition, material structure can also be used to grade the properties of a material. Cellular materials are found in bone structures, woods, corks, corals, honeycombs, and countless other natural structures. Engineered foams and honeycombs, also known as architected materials, have been designed for decades to replicate the relatively low density and high stiffness of these cellular materials [35]. Additive manufacturing provides unprecedented control over part geometry at the micro and even nanoscale. As such, much research has been dedicated to the additive manufacturing of architected materials [7, 15].

While traditional architected materials like honeycombs or sandwich panels repeat a single unit cell, some researchers have used multiple cell configurations to grade the properties of a material [36, 37, 38, 39, 40]. By controlling the cell architecture at a material point, designers can easily dictate the stiffness at that point in each direction. As such, gradient cellular materials can be used to provide designed compliance or produce an optimal dynamic response.

For example, Lira et al. [39] optimized the dynamic response of a gradient architected material to design an aeroengine fan blade. Similarly, Khanoki et al. [40] designed the gradient cellular structure of a bone implant to optimize bone reabsorption and interface stress. Niknam et al. [41] performed a systematic study to compare optimized gradient cellular structures to structures of a single cell type. The authors observed an over 50% increase in bending stiffness can be achieved in an optimized gradient cellular structure compared to a uniform cellular structure of the same mass. In all of these examples, prototypes were constructed out of polymers via fused deposition

modeling.

1.2.2.2 Other Methods of Grading Structure

Aside from specifically designing architected cells or lattices, there are numerous other methods for grading the structure or microstructure of a material. Since the early 2000s, researchers have demonstrated that local control of properties and therefore functional grading can be achieved in polymers by changing process parameters like raster orientation, width, and deposition density [42, 43]. Steuben et al. [44] developed a slicing algorithm that can spatially design the infill pattern and consequently grade in stiffness and density.

Though functional grading has not been widely demonstrated in this manner for metals, it is known that laser properties like power, speed, and hatch spacing have a strong effect on properties and could conceivably be used to functionally grade [45]. For example, List et al. [46] varied electron beam parameters to change the elastic properties of Inconel 625 lattice structures by up to an order of magnitude. In addition to grading laser parameters, metal FGMs have also been created through the use of acid etching to produce pores and channels within the microstructure and consequently control the stiffness of the material [47].

1.3 Compositionally Graded Alloys

Functional gradients in metals provide unique promise given the proliferation of metals as high-performance materials in engineering applications. Graded metals introduce a new canvas of potential material properties that graded polymers or ceramics cannot provide. And while metal FGMs have been achieved through various structural grading techniques, structure alone is limited in its capacity to influence material properties. Compositionally graded alloys enable potential property gradients across the entire range of properties exhibited by any metal alloy. Composition also facilitates control over some of the most exceptional properties of metals, like density; ductility; thermal or electrical conductivity; and temperature, corrosion, or oxidation resistance.

The welding of dissimilar metals, either by laser or by friction, is a decades-old process that produces a sharp compositional gradient, but such welds are known to produce deleterious phases,

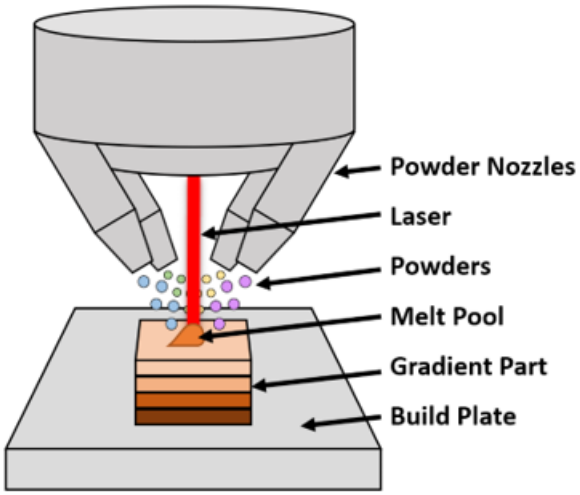

Figure 1.1: A schematic of how a Directed Energy Deposition (DED) process can be used to create a compositionally graded metal part.

as compositions diffuse, and sharp property gradients which in turn lead to points of failure and cracking [48, 49, 50, 51]. While traditional welding is seen mostly as a joining process, laser cladding has been used since the 1990s to create sharp functional gradients, like protective surface coatings [52, 53, 54]. However, laser cladding can also suffer from the same sharp gradients in properties, like coefficient of thermal expansion and hardness, that can lead to induced stresses and mechanical failures. These issues can be avoided by more gradually varying composition, but true compositional grading within metals was not widely researched until the development metal additive manufacturing, particularly Directed Energy Deposition (DED) [55].

Unlike more mature powder-bed processes, powder is deposited directly onto a substrate and instantly solidified with a high-powered laser during the DED process. Because powder does not have to be pre-allocated in bulk, like in a bed system, powders can be drawn from separate powder feeders and mixed just before solidification, either in a mixer before the nozzles or directly on the substrate. By carefully controlling the ratio of powders during this mixing process, powders of different compositions can be used to change composition layer-by-layer. Figure 1.1 depicts this process of creating a compositional gradient in a simplified schematic.

Directed energy deposition processes were used to create compositionally graded alloys shortly after their inception in the late 1990s and early 2000s. In 2003, Collins, Banerjee et al. [56, 57] created compositional gradients from pure titanium to up to 25 atomic percent molybdenum or vanadium. In the 2010s, as additive manufacturing grew in popularity, numerous researchers used DED to produce compositional gradients between a wide array of alloys [58, 59, 60, 61, 62, 63, 64, 65]. Alloys that are commonly used in additive manufacturing have been particularly prevalent in attempted gradients. Notable examples include stainless steel, Ti-6Al-4V, Invar and Inconel. While recent years have seen a notable increase in interest towards compositionally graded alloys, relatively few such alloys have been used in applications or even successfully manufactured [60, 64]. This is because compositional gradients in metals are prone to numerous issues that complicate their manufacturing and inhibit the realization of their full potential.

1.3.1 Common Issues

1.3.1.1 Formation of Deleterious Phases

The formation of secondary phases with deleterious properties is the most prominent issue when creating a compositionally gradient between most alloys. For example, both Carrol et al. [59] and Chen et al. [60] observed crack-forming secondary phases when manufacturing a linear gradient between 304L stainless steel and Inconel 625. Similarly, Bobbio et al. [61] and Meng et al. [62] observed similar cracks induced by brittle intermetallic phases in the linear gradient from Ti-6Al-4V to Invar and Inconel 625, respectively. These examples and others are listed in Table 1.1.

These phases form because metals readily diffuse and form new phases to reach equilibrium, as is well known in the welding of dissimilar metals [49, 50, 69]. While phases in graded composites in polymer or ceramic systems often stay separate throughout their graded regions, most binary phase diagrams between metals show the formation of new phases and do not have mutually soluble solid phases for the entire composition range. Consequently, it is difficult to find compositions from two unique alloy systems for which a linear composition gradient would not contain

Table 1.1: Selected compositionally graded alloys and associated secondary phases

Linear Gradient	Deleterious secondary phases	Reference
Steel to Inconel	• Metal monocarbides (MoC, NbC)	[59, 60, 66, 67]
Steel to Ti-6Al-4V	• Intermetallic (FeTi) • Sigma phase	[63]
Ti-6Al-4V to Invar	• Intermetallics (FeTi, Fe_2Ti, Ni_3Ti, $NiTi_2$)	[61]
Ti-6Al-4V to Inconel	• Intermetallics (Ti_2Ni, TiNi, $TiNi_3$) • Metal monocarbide (NbC) • Unidentified Cr and Mo phases	[62]
Inconel to Copper	• Intermetallic (Cr_2Nb)	[68]

secondary phases

The formation of secondary phases is not inherently harmful to a gradient material. However, the deleterious phases that often form in compositionally graded alloys, like those listed in Table 1.1, tend to be significantly more brittle or hard than the matrix material [64]. Deleterious phases therefore lead to sharp changes in properties, or property discontinuities, which in turn produce stress concentrations and initiate cracks.

1.3.1.2 Property Discontinuities

It is well known in the welding community that large differences in the properties of the base materials will produce problematic property variations across the joint [49]. Compositionally graded alloys were partly conceived to combat these sudden variations by smoothly grading composition, and thus properties, over many layers of material. However, when properties change drastically or suddenly within the gradient, like when secondary phases form, compositionally graded alloys can be similarly problematic.

Consider the Coefficient of Thermal Expansion (CTE), which describes how much a material

expands or contracts with changes in temperature. If the CTE across a gradient has a sharp change or discontinuity residual stress will build when the material experiences large changes in temperature. The additive manufacturing process occurs near melting temperatures and is fast cooling, so any additively manufactured graded alloy will necessarily experience large temperature gradients. Therefore, CTE discontinuities can be catastrophic to compositionally graded alloys and often lead to cracking during manufacturing [61]. Discontinuities in ductility, like those introduced by brittle intermetallics, will induce similar residual stresses and also lead to failure.

Steep changes in other types of properties can also be detrimental to gradient materials. The parameters that control the additive manufacturing process, like laser power or speed, are dependent on intrinsic material properties, like absorptivity, thermal conductivity, and melting temperature. If these properties change significantly within a gradient, then process parameters need to be changed during the build to successfully print the material without defects. If property changes are too steep, it might be impossible to change process parameters with sufficient detail. Large differences in thermal conductivity and melting temperature can also affect the heat flow within the material and prevent the fusion of one section of the gradient without vaporizing another section.

1.3.1.3 Other Manufacturing Challenges

The manufacturing of compositionally graded alloys is also complicated by the fact that finding material compositions that are suitable for additive manufacturing is often a difficult task [70]. In fact, many common alloys have not been successfully printed and have instead been replaced by printable counterparts in the additive manufacturing community. Perhaps the most well known example of this is the adoption of AlSi10Mg over traditional aluminum alloys, which have been extremely difficult to print without defects [71]. The problem of finding a printable composition is only compounded when designing a compositionally graded alloy, as the gradient region represents a continuous range of compositions, each of which must be printable by additive manufacturing techniques.

There are many properties which influence how successfully a material can be additively manufactured [72]. One such property is the difference between the solidus or liquidus temperatures of

a material, otherwise known as its solidification range. A large solidification range can mean the solidification process takes relative longer, prolonging the coexistence of liquid and solid phases. When these phases coexist for extended periods, particularly during the end of solidification, materials become susceptible to a phenomena known as hot-tearing, which leads to crack initiation during manufacturing [73, 74, 75]. For this reason, most printable alloys have relatively small solidification ranges.

A robustly designed compositional gradient should contain only compositions that are well suited for manufacturing, but the compositions of a gradient can change significantly during the manufacturing process. This diffusion process poses another significant challenge to the manufacturing of any compositionally graded alloy [64]. Because such alloys are manufactured from elemental powder blends at elevated temperatures, the driving forces for compositional diffusion are generally favorable. This can mean that the deposited powder composition might not match the final composition of the manufactured part as the material equilibrates after cooling. This process can be mitigated by ensuring compositional gradients are sufficiently smooth or, in other words, composition changes slowly between layers. In this way, the driving forces for diffusion can be minimized.

1.3.2 Previous Design Methods

1.3.2.1 Interlayers in Dissimilar Welds

Many of the issues that have been described for compositionally graded alloys are also prevalent in the welding community when joining dissimilar metals. In that community, discrete interlayer materials have often been used as potential solutions [76]. For example, if two dissimilar metals tend to form brittle intermetallics together, a third metal that has better compatibility with both base metals can be placed between them. Likewise, if two base metals have large property discrepancies, then a third metal with intermediate property values can be used to mitigate property discontinuities across the joint. For example, copper interlayers are commonly used when welding stainless steel and titanium alloys [77, 78, 79]. Similarly, zinc interlayers have been used

to improve the properties of welds between aluminum and magnesium alloys [80, 81].

Dissimilar welds with an interlayer material do not represent truly compositionally graded alloys, as only three discrete compositions are present instead of a continuous range. However, the notion of using a third material that is not present in either base metal (e.g. copper or zinc) is an important concept in the design of compositionally graded alloys. Such materials can be used to realize otherwise unattainable gradients between two incompatible alloys. The added flexibility of additive manufacturing makes it even easier to add new elements to a compositionally graded alloy. Another powder feeder can be easily incorporated into the mixing process to introduce new elements into a gradient build. Powders can even be intelligently combined to change composition non-linearly.

1.3.2.2 Planning Gradients with Phase Diagrams

While deleterious phases are a significant issue when designing a gradient alloy, the formation of phases in metal alloys is a mature and well-studied field. Phase diagrams are common tools for material scientists to visualize which phases form as a function of thermodynamic conditions. In fact, thermodynamic principles can be used to predict the equilibrium phase fractions of a material given models of phase free energies. This method is commonly referred to as CALculation of PHase Diagrams or the CALPHAD method [82]. The CALPHAD method originated in the 1950s [83] and, in the decades since, has developed into an active community [82].

In 2014, Hofmann et al. [1] originated the idea of using phase diagrams produced via the CALPHAD method to plan compositionally graded alloys. In their approach, ternary phase diagrams are used to determine which phases a linear gradient between two compositions is predicted to produce, and then new paths can be planned that avoid deleterious phases. Ternary phase diagrams typically visualize phases in a composition space formed by three elements at a single temperature. Figure 1.2 depicts how a ternary phase diagram can be used to design compositionally graded alloys in ternary space formed by the hypothetical elements X, Y, and Z. In Fig. 1.2, the linear gradient between candidate alloys 1 and 2 are predicted to form the fictional γ phase, which has been deemed deleterious in this example. Because the ternary phase diagram enables easy visualization

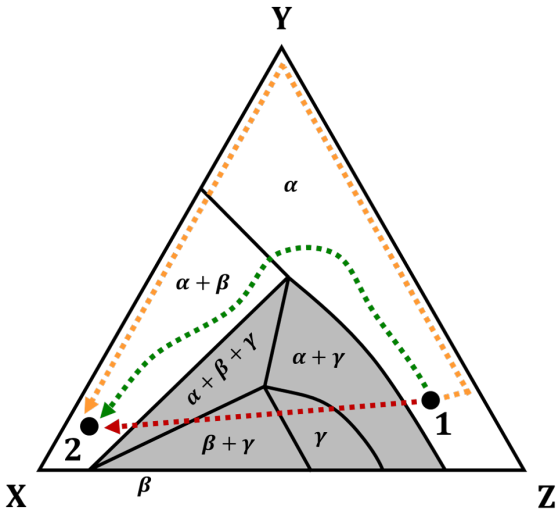

Figure 1.2: An example of how an isothermal ternary phase diagram can be used to design compositionally graded alloys, as proposed by Hofmann et al. [1]. The linear gradient (shown in red) between alloy 1 and 2 will develop a significant amount of detrimental phase γ, while a gradient (shown in yellow) that follows the Y-Z and X-Y binaries will not develop any γ phase. Some other gradient (shown in green) might also avoid γ phase, while requiring less deviation from the linear gradient. Reprinted with permission from Eliseeva et al. (2019) [2].

of the ternary space, it becomes clear that adding more of element Y to the gradient can help avoid γ phase. The binary edges of the space can be navigated from alloy 1 to the pure element Y and then to alloy 2, as shown by the yellow path. A shorter, non-linear path can also avoid γ phase by adding a smaller amount of Y, as shown in green in Fig. 1.2.

The strategy developed by Hofmann et al. [1] was employed by their collaborators in Reichardt et al. [63] to design a gradient from Ti-6Al-4V to 304L stainless steel. The authors first attempted a path from Ti-6Al-4V to pure vanadium to stainless steel, but the formation of a brittle deleterious phase led to cracking during the manufacturing process. Examination of the isothermal Fe-V-Cr ternary phase diagram at 850 °C revealed that the deleterious phase was the sigma phase, common to many Cr-rich steels. The authors then used the same ternary phase diagram to replace the V to stainless steel portion of the original gradient. This new path instead varied compositions from V to Fe45Cr55 [wt%] to stainless steel. While this new path was not printed, it was predicted to avoid the sigma region of the phase diagram entirely and should be simple to manufacture with a

DED process.

1.3.2.3 Limitations

Despite enabling a means of avoiding deleterious phases, there are several limitations to the aforementioned design method for compositionally graded alloys. One significant limitation is that this method relies on the visualization of two-dimensional diagrams. For conventional ternary phase diagrams, this means that only spaces formed by three elements at a single temperature can be visualized. Although, it is possible to represent more than three elements in a phase diagram by using fixed ratios of elements instead of pure elements on the axes. Regardless, any phase diagram can only visualize two or, at a maximum, three degrees of freedom (i.e. dimensions) at a time.

Another limitation is that conventional phase diagrams represent equilibrium predictions at a single temperature, and additive manufacturing is known to be a non-equilibrium process due to rapid cooling rates [64]. To address this specific issue, Moustafa et al. [84] have recently developed Scheil Ternary Projections or STeP diagrams specifically for the design of compositionally graded alloys. These diagrams display the phases predicted by Scheil solidification simulations [85], which are known to be more accurate representations of the phases that form during the additive manufacturing process [64]. Bocklund et al. [86], applied such simulations to the investigation of a gradient between titanium alloys and Invar-36 and observed increased accuracy compared to traditional equilibrium calculations.

While more accurate diagrams can improve these previous approaches, any design methodology that relies on visualization will be inhibited by the limits of human perception. This means that the design space must be projected into some combination of two or three-dimensional depictions. These visualizations can help designers understand how design variables will affect their desired outcome, but they can not provide a design independently. The designers domain knowledge is critically important in these techniques as knowing which diagrams will be most effective and which design decisions to make is non-obvious.

Even domain experts can and likely will have difficulty designing feasible gradients in the multi-dimensional spaces formed by most gradient alloys. Consider a gradient between stainless

steel and Ti-6Al-4V. The principal elements in stainless steels are Fe, Ni, and Cr, therefore the minimum number of total elements involved a potential gradient is six (Fe, Ni, Cr, Ti, Al, and V) without considering the addition of other elements to aid in constraint avoidance or design performance. This 5-dimensional space (one element as balance) contains ${}_6C_3 = 20$ ternary subspaces by simple combinatorics. Each one of these twenty ternaries could contain relevant phase information or potential gradient paths, but none of them can help visualize the four, five, or six-element phases that might form in the gradient region. It is therefore impossible to visualize such a large space in any meaningful way and most compositionally graded alloys involve base alloys with at least as many elements.

1.4 Research Objectives

Given the size and complexity of the navigable composition space, it is unlikely that the optimal path through this space can be reached without computational techniques in most gradient design problems. While others have demonstrated computational techniques in the production of diagrams to aid in the design process [1, 59], no prior research has presented a computational methodology to directly optimize the compositional gradient path. The goal of this research is *to create a computational methodology that will produce compositional gradient paths that satisfy design requirements and optimize performance objectives*.

1.4.1 Plan Gradients in Higher Dimensions

The primary motivation in pursuing a computational methodology is to avoid the need to visualize a higher dimensional composition space. As discussed in Section 1.3.2.3, thoroughly visualizing a composition space with more than three elements is largely intractable, even though it is necessary for most gradient design problems. Computational techniques, however, do not suffer from the same set of limitations as human designers and can design in spaces that humans cannot visualize.

One technique that is particularly well suited to the gradient design problem is path or motion planning. Originated in the 1970s [87], motion planning initially involved planning the paths

of points in two dimensional space, but has evolved to planning the complex motions of robotic manipulators with many degrees of freedom [88, 89]. These algorithms can be naturally extended to plan paths through composition space and, consequently, became one of the cornerstones in the proposed methodology.

The ability of path planning algorithms to overcome the limits of visualization will be validated by planning gradient paths in spaces of more than three dimensions. Although the scalability of these algorithms is well known, another research objective is to quantify their scalability in the context of gradient design. Further, it will be shown that the scale of most gradient path design problems is tractable with the proposed methodology.

1.4.2 Design Gradients to Satisfy Constraints

Many of the qualities desired in compositionally graded alloys can be expressed as satisfied or not satisfied by a given gradient path, such as the presence of deleterious phases. Such quantities can be used as hard constraints to classify gradient paths as feasible or infeasible.

Focus is given in this research to constraints that can be represented as constrained regions in composition space. For example, the formation of deleterious phases can be readily predicted as a function of composition and temperature. Similarly, suitability for additive manufacturing can also be assessed as a function of composition. As such, regions of composition space that violate specified constraints on phase formation and manufacturability can be identified and avoided. These regions are analogous to obstacles in conventional motion planning and, therefore, can be easily avoided by common path planning algorithms.

The formulation of *deleterious phase formation* and *manufacturability requirements* as design constraints in a path planning context will be presented. The ability of the proposed methodology to satisfy such constraints will be demonstrated in real gradient design case studies. As many of these constraints require surrogate modeling to evaluate efficiently, the accuracy and scalability of associated surrogate models will also be demonstrated.

1.4.3 Optimize Gradients for Design Objectives

Some characteristics of a gradient exist on a continuous scale of value and are best treated as design objectives. These are quantities that designers seek to minimize or maximize for a given a gradient, like those associated with performance or cost. Other quantities which could be represented as constraints are not easily met by hard constraints and are better formulated as soft constraints or penalty objectives. A unique benefit of a computational technique is the ability to find gradient paths that optimize these quantities in large, complex spaces.

Four **objective functions**, or **cost functions** as they are called in the path planning community, will be used to optimize gradient paths in this research:

- *Minimization of path length*
- *Maximization of obstacle clearance*
- *Minimization of constraint violation*
- *Minimization of property non-monotonicity*

The first two objectives are common in motion planning. In gradient design, path length in composition space is correlated with both the minimum number of layers and the amount of excess material needed to print a gradient part. Maximizing obstacle clearance, or separation from the constraint boundaries, produce paths that are robust to compositional variance or errors in constraint modeling and are therefore less likely to violate constraints.

Minimizing constraint violation or including a penalty function in the objective is a common tactic in optimization. In the current methodology, it is sometimes necessary to treat constraints this way if constrained regions occupy too much of composition space and prevent the discovery of feasible paths. Constraints of this type often occur when deleterious phases are prevalent, as will be shown with aluminum intermetallics in aluminum-rich alloys.

The last cost function incorporates the properties of the gradient material into the design process. As discussed in Section 1.3.1.2, property discontinuities are a major source of failure in

gradient materials. Additionally, most functionally graded materials are designed to achieve a desired gradient in properties. It is a non-trivial task to formulate all possible property preferences into a single cost function. However, in this research, a novel cost function is presented to prioritize property monotonicity. It will be shown that property monotonicity ensures that gradients can be transformed to minimize property discontinuities or achieve any bounded spatial distribution of properties, subject to manufacturing capabilities. To the authors' knowledge, this is the first application of monotonicity as both an objective for gradient design and as a cost function for a path planning algorithm.

The value of these cost functions to gradient design will be further explained in detail later in the dissertation. The path planning algorithm used in the methodology provides guarantees of probabilistic completeness and asymptotic optimality for compatible cost functions. The conditions for compatibility will be discussed and shown to be met for each of the four cost functions. Each cost function will also be demonstrated in a real gradient design problem, where the ability of the path planning algorithm to find the globally optimal solution will be discussed.

1.5 Contributions and Scope

The fundamental contribution of this research is the formulation of compositionally graded alloy design as a path planning problem and the creation of a computational design methodology to solve that formulation. The methodology is demonstrated for a variety of constraint formulations and objective functions to produce four new compositionally graded alloys in various systems. The primary contributions of this research are summarized below:

1. Formulation of gradient material design as a path planning problem
2. Creation of a novel computational methodology for the design of compositionally graded alloys that enables:
    (a) Planning gradient paths in large multi-component spaces that are not possible to visualize
    (b) Adherence of gradient paths to specified design constraints

(c) Optimization of gradient paths for user-defined objectives

3. Demonstration of deleterious phases as a potential constraint in the design of a gradient path between steel and chromium in the Fe-Ni-Cr space

4. Demonstration of manufacturing metrics as a potential constraint in the design of a gradient path between steel and tungsten in the Fe-Ni-Cr-W space

5. Demonstration of the minimization of constraint violation as a potential objective in the design of a gradient path between steel and aluminum in the Fe-Ni-Cr-Al-Ti-Temperature space

6. Novel formulation of property monotonicity as a potential design objective and demonstration in the optimization of a gradient path in the Fe-Co-Cr space for Coefficient of Thermal Expansion

The first formulation of gradient design as a path planning problem is presented in the next chapter. Next, a summary is given of the methodology and the computational tools used therein. An illustrative example of deleterious phases as a constraint is shown in the planning of gradient paths in the Fe-Ni-Cr system. For this case study, two cost functions are considered: minimization of path length and maximization of obstacle clearance. Simple studies of stochastic variation and time complexity are also given in this system. The use of manufacturing metrics, like solidification range and cracking susceptibility criteria, is shown in another case study in the Fe-Ni-Cr-W system. To showcase the use of constrain violation as a cost function, a gradient path between steel and aluminum was planned in Fe-Ni-Cr-Al-Ti-Temperature space, which also exhibits the advantage of the methodology in higher dimensional spaces. Lastly, the value of property monotonicity is discussed and a novel cost function to optimize for property monotonicity is presented. The use of this cost function is illustrated in a synthetic case study and applied to a real gradient design problem in Fe-Co-Cr space.

2. GRADIENT DESIGN AS A PATH PLANNING PROBLEM

The compositions in a compositionally graded alloy can be modeled as a path through composition space. Consequently, algorithms that have been developed for path planning can be naturally adapted to plan gradient paths. Motion planning is the field of study dedicated to planning the motion of autonomous vehicles. This chapter reviews the structure of the motion planning problem as well as motion planning terminology. The problem of designing a gradient alloy is then adapted to this structure and formulated as a path planning problem.

2.1 The Motion Planning Problem

The motion planning problem, also known as the Piano Mover's Problem, is the problem of finding a feasible path from one location to another without colliding into obstacles [90]. Motion planning or path planning came from the field of artificial intelligence in the 1960s, but it was the work of Lozano-Perez and Wesley in the late 1970s [87] that introduced the configuration space and ushered in the modern era of motion planning. This section describes the motion planning problem and provides a general mathematical formulation that will be adapted to the design of compositionally graded alloys.

2.1.1 Motion Planning Terminology

This section defines terms from the motion planning community that are relevant to all motion planning problems.

Definition 1. (Configuration). *A set of parameters that characterize the state of the object in motion (e.g. the x-y coordinates of a vehicle's location).*

Definition 2. (Configuration or State Space). *The set of all possible configurations or states.*

Definition 3. (Path). *A curve in configuration space.*

Definition 4. (Path Index). *A continuous variable that corresponds to a specific configuration in the path.*

Definition 5. (Obstacle Region). *The subset of configuration space occupied by obstacles. Feasible paths do not intersect this space.*

Definition 6. (Free Space). *The subset of configuration space that is not occupied by obstacles. The complement of the obstacle region in the configuration space.*

Definition 7. (Collision). *The intersection of a path with the obstacle region.*

Definition 8. (Feasible Path). *A path that is collision-free and connects the initial and goal configurations.*

Definition 9. (Cost Function). *Function that relates a path to a scalar cost. Generally minimized by the optimal path.*

2.1.2 A General Motion Planning Problem Formulation

The following problem formulation was adapted from the work of Karaman and Frazzoli [91], who introduced a mathematical framework to describe the behavior of sampling-based path planning algorithms, which was later extended by Adiyatov and Varol [3]. Although it was intended for these algorithms, it can be applied to the optimal motion planning problem in general.

Let Z^d represent the *configuration space* or *state space* of the environment, where $d \in \mathbb{N}, d \geq 2$ is the dimensionality of the space. The *obstacle region*, $Z_{\text{obs}} \subset Z^d$, is the region occupied by obstacles or otherwise to be avoided. The *free space* is defined as $Z_{\text{free}} = Z \setminus Z_{\text{obs}}$ and represents the space available for path planning. The *initial state*, $z_{\text{init}} \in Z_{\text{free}}$, and *goal state*, $z_{\text{goal}} \in Z_{\text{free}}$, define the endpoints of the path being sought and must be elements of the free space for a solvable problem.

Let the continuous function $\sigma : [0, 1] \to \mathbb{R}^d$ represent a *path*. Let $\alpha \in [0, 1]$ represent a *path index* that scales with the Euclidean distance traversed by the path in $\mathbb{R}^d$ (i.e. path length), l, in state space. Equation 2.1 represents the scaling of α where α is defined as the path length up to a position $\sigma(\alpha)$ along the path normalized by the total length of the path.

$$\alpha := \frac{l(\sigma(0), \sigma(\alpha))}{l(\sigma(0), \sigma(1))} \, \forall \, \alpha \in [0, 1] \tag{2.1}$$

A path is *collision-free* if $\sigma(\alpha) \in Z_{\text{free}} \; \forall \, \alpha \in [0,1]$. A path is *feasible* if it is collision-free, $\sigma(0) = z_{\text{free}}$, and $\sigma(1) = z_{\text{goal}}$. In probabilistic algorithms, the final condition is often stated as $\sigma(1) \in \text{cl}(Z_{\text{goal}})$, where $\text{cl}(Z_{\text{goal}})$ is the closure of the *goal region*, Z_{goal}.

Let $c : \sigma \rightarrow R$ represent a *cost function* that relates a path to a scalar path. The goal of the *optimal motion planning problem* is to find the feasible path that minimizes this cost function, σ_{best}. Note that for many path planning algorithms, guarantees of optimality are only assured if the cost function satisfies certain additional criteria. The optimal motion planning problem formulation is summarized below:

$$
\begin{aligned}
\textbf{Find} \quad & \sigma_{\text{best}} = \textbf{arg}\min_{\sigma} \; c(\sigma) \\
\textbf{subject to} \quad & \sigma(\alpha) \in Z_{\text{free}} \; \forall \, \alpha \in [0,1], \\
& \sigma(0) = z_{\text{init}}, \\
& \sigma(1) = z_{\text{goal}}.
\end{aligned}
$$

Algorithms that solve this problem formulation will be discussed in Section 3.2.

2.2 Gradient Design Problem Formulation

Materials are often defined by a list of parameters which specify their state. For example, metal alloys are typically defined by their composition: a list of elements and their relative proportions within the material. A Functionally Graded Material (FGM) is composed of several material states (e.g. composition or structure), each with their own associated properties. If the functional gradient is continuous, then it can be represented by a function that relates some index to material state. In this way, continuous FGMs can be thought of as paths through state space, where the state space contains all possible material states.

Compositionally graded alloys in particular can be thought of as paths through composition space, as the composition changes continuously in the graded region. However, the state at any point in a compositionally graded alloy can be described by more than just composition. There are numerous processing conditions that can also affect the state of the material, like temperature,

temperature history, or laser parameters. Equation 2.2. represents a point in the state space of a compositionally graded alloy, where x_i represents the composition of the ith element and P represents additional process variables.

$$z = \left\{ x_1, ..., x_N, P : \sum_{i=1}^{N} x_i = 1 \text{ and } x_i \geq 0 \ \forall \, i \right\} \tag{2.2}$$

The nature of the composition variables require additional constraints on the state space. As seen in Eqn. 2.2, these are that all compositions must sum to unity and all compositions must be greater than or equal to zero. These constraints mean that the composition of one element can be left out of the state space during path planning, as it can be treated as a balance element and computed from the compositions of the other elements. This results in the state space described by Eqn. 2.3. If there are no processing variables P, this space results in a standard simplex, which has unique consequences for computational techniques that will be discussed in Chapter 3.

$$z = \left\{ x_1, ..., x_{N-1}, P : x_N = 1 - \sum_{i=1}^{N-1} x_i \text{ and } x_i \geq 0 \ \forall \, i \right\} \tag{2.3}$$

Because compositionally graded alloys can be represented as paths through a state space, they can be optimized for design using the path planning problem formulation discussed in Section 2.1.2. This enables the use of path planning algorithms to design gradients that optimize cost functions, subject to constraints on the state space.

Many of the challenges associated with compositionally graded alloys can be represented as constraints on the state space and used to define the obstacle region, Z_{obs}. For example, deleterious phases can be predicted for a given composition and temperature using the CALPHAD method. These predictions can be used to construct the constraint region shown in Eqn. 2.4, which includes any composition that produces a deleterious phase fraction, $f_{\text{deleterious}}$, above some constant, λ, for at least one temperature between some minimum and maximum temperature, T_{min} and T_{max} respectively. This constraint formulation is useful for avoiding deleterious phase formation at any temperature a gradient part might experience. Given that the additive manufacturing process

involves large fluctuations in temperature, this approach is reasonable, if mildly conservative. Although this formulation of Z_{obs} can help avoid a major issue with compositionally graded alloys, it is but one of many possible ways to incorporate gradient design requirements as constraints in state space. Once the obstacle region is defined, the compositions within the obstacle region will be treated as hard obstacles and avoided by feasible paths.

$$Z_{\text{obs}} = \left\{ z : f_{\text{deleterious}}(z, T) \geq \lambda \; \exists \, T \in [T_{\text{min}}, T_{\text{max}}] \right\} \tag{2.4}$$

The obstacle region can also be used to define the free space, Z_{free}, which is the complement of the obstacle region in state space. For example, the free space associated with the obstacle region defined in Eqn. 2.4 is shown in Eqn. 2.5. These are the compositions that produce deleterious phase concentrations below the specified maximum limit at all temperatures in the specified range.

$$Z_{\text{free}} = \left\{ z : f_{\text{deleterious}}(z, T) < \lambda \; \forall \, T \in [T_{\text{min}}, T_{\text{max}}] \right\} \tag{2.5}$$

Cost functions, $c(\sigma)$, that incorporate common gradient objectives can also be used to optimize gradient alloys. For instance, the most common cost function in path planning is path length. The limiting factor when minimizing the size of a gradient part (i.e. the number of layers in the gradient) is often the magnitude of the composition change. As such, minimizing the path length of a compositionally graded alloy in composition space will minimize the minimum number of layers needed to print the gradient. Alternative cost functions can embody other aspects of gradient alloys that designers might wish to optimize, as will be demonstrated later in this dissertation.

Figure 2.1 depicts a simplified illustration of how a hypothetical gradient material can be represented as a path in composition space. The path is shown in a state space formed by the compositions of three elements: A, B, and C. A rectangular gradient part is also shown to emphasize how each point in the path corresponds to a specific composition along the gradient. A computational methodology to design such paths is the main contribution of this research and will be discussed in detaile in Chapter 3.

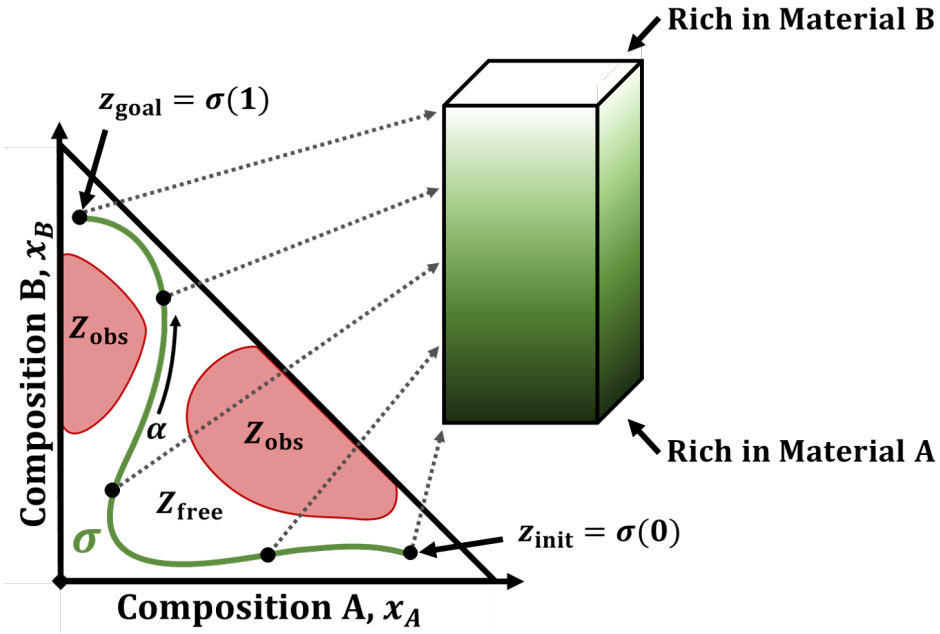

Figure 2.1: A simplified example of how a gradient material from an initial composition rich in Material A to a goal composition rich in Material B can be represented as a path in a ternary (three element) composition space. While not explicitly labeled, the composition of the third element can be inferred as the remainder (100% at the origin).

3. COMPUTATIONAL METHODOLOGY

This chapter details the original computational methodology that serves as the main contribution of this research, which solves the gradient design problem formulation described in Chapter 2. It was created to be as efficient as possible while being scalable to high dimensions and adaptable to a diverse set of potential constraints and cost functions. The first section describes the general framework and following sections detail each component. Specific focus is paid to the rationale behind the structure of the methodology and the computational tools used therein.

3.1 General Framework Summary

The foundation of the computational methodology is a *path planning algorithm* that solves the gradient design problem formulation presented in Chapter 2. While many such algorithms exists, the algorithm chosen in this methodology is an optimal Rapidly-exploring Random Tree (RRT*) algorithm, originally developed by Karaman and Frazzoli [91]. Specifically, Adiyatov and Varol's Fixed Nodes implementation of RRT* (RRT*FN) [3] was chosen because designers can limit the occupied memory during the search process. Section 3.2 provides a detailed description of this algorithm and explains why it was chosen over other common path planning algorithms.

In order to design feasible compositionally graded alloys, the path planning algorithm needs a model of the obstacle region in state space. *CALculation of PHAse Diagram (CALPHAD)* software is the primary modelling tool in the methodology due to its ability to accurately predict phase formation and physical properties from thermodynamic conditions (e.g. composition and temperature). Many of the constraints and objectives that are relevant to graded alloy design can be stated in terms of quantities that CALPHAD can predict. Examples include phase formation, solidification properties, density, thermal expansion, and other physical properties.

Although CALPHAD modelling is essential to the methodology, its computational expense is relatively large. Because most path planning algorithms require many evaluations of the obstacle region and cost function, if these processes are inefficient they can render path planning intractable

for realistic problems. Surrogate modeling is used to reduce the computational expense of sampling CALPHAD directly during the path planning process. For representation of the obstacle region, machine learning *classifiers* are trained on CALPHAD data. These classifiers make a simple binary prediction for any point in the state space: whether it lies within the obstacle region or the free space. The use of classifiers has the added benefit of representing multiple constraints in one model, so that only one model needs to be evaluated to determine obstacle collision.

The final key component to the methodology is the *cost function*. This function defines the optimality of gradient paths during the search process and express the objectives of the designer, like cost, manufacturability, or performance. Like the obstacle model, the cost function should also be made as efficient as possible to reduce the overall processing time and to keep the path planning process tractable. As such, the surrogate models are also created to predict the cost or its dependent variables over the state space. In the cost case, machine learning *regression* is used for surrogate modeling because cost is traditionally a continuous variable over the state space.

Figure 3.1 is a flow diagram that illustrates how the general framework of the computational methodology solves a gradient design problem formulation. The methodology begins with the computational models that provide relevant information about the state space. For example, CALPHAD can be used to predict phase fractions and physical properties, but other models that predict relevant quantities can also be used. These are sampled throughout state space to train two surrogate models: a classifier to model the obstacle region and a regressor to model the cost function. The details of these models (e.g. the decision boundary of the classifier) are dependent on the constraints and cost function defined in the problem formulation. After the surrogate models have been trained, the path planning algorithm, RRT*FN [3], plans a path through state space by sampling the obstacle model and cost function to determine collision and optimality respectively. Eventually, the path planning algorithm arrives at the optimal gradient path that solves the problem formulation.

3.2 Path Planning Algorithm

This section first reviews common motion planning algorithms and discusses their advantages and disadvantages in the context of gradient design. A rationale is given for sampling-based plan-

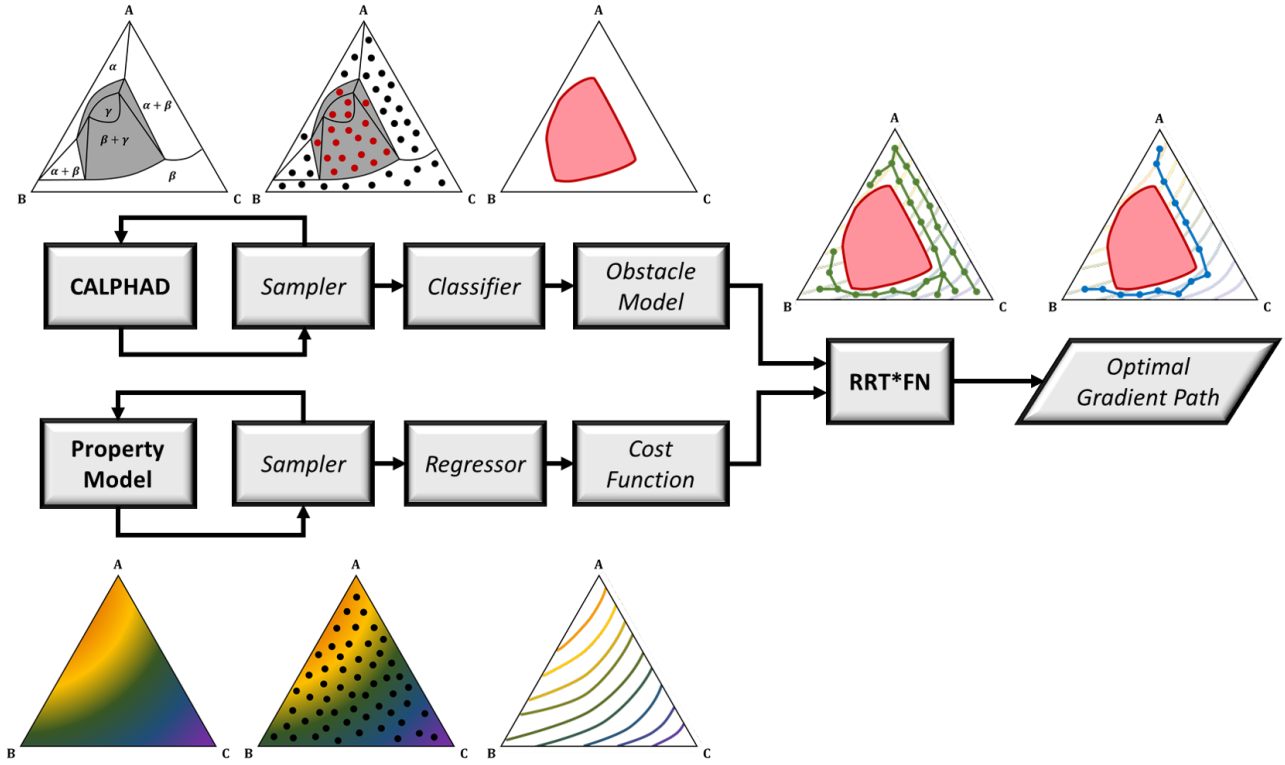

Figure 3.1: Simplified flow diagram of the general methodology. First, relevant models of phase information and properties are sampled. These samples are used to construct surrogate models for the obstacle region and cost function, based on design constraints and objectives. The path planning algorithm (RRT*FN [3]) uses these to produce an optimal gradient path.

ners as a promising class of algorithms for gradient path problems. Of these algorithms, the optimal Rapidly-exploring Random Tree (RRT* [91]) algorithm is one of the most prominent because of its computational efficiency. This section concludes with a detailed description of the specific implementation of RRT* used in the methodology (RRT*FN [3]).

3.2.1 Common Algorithms

Motion planning is a diverse field that includes the planning of any object through space. These can be objects as simple as point robots, but also includes three-dimensional vehicles, robotic manipulators, legged robots, or many robots planned at the same time [92]. The configuration spaces occupied by these objects scale with the degrees of freedom possessed by the object and, consequently, can range from just two dimensions to tens to well over a hundred [93]. The configuration

spaces themselves can also vary with time or change as the robot moves through its environment. The diversity of the problem set and recent advances in robotics and artificial intelligence have led to rapidly expanding interest and thousands of papers in the past few decades [88, 89].

In this section, common motion planning algorithms will be reviewed and their efficacy in solving a gradient material design problem will be assessed. Due to the nature of the gradient design problem, special focus is given to those algorithms that plan paths for a single point robot in time-invariant spaces. Priority is given to algorithms that scale well with the dimensionality of the space and can therefore plan gradient paths with many constituent elements. Algorithms that can optimize a variety of cost functions are also desired in that they can incorporate many types of design objectives.

3.2.1.1 Exact Algorithms

The first class of algorithms are deemed to be *exact* because of the guarantees they offer. The first guarantee these algorithms provide is that they are *complete*. A complete algorithm terminates in finite time and returns a feasible path, if one exists, and reports failure otherwise [91]. The presented algorithms are also guaranteed to return the globally optimal path for their respective cost functions.

One of the simplest methods of planning a path around obstacles is by constructing a *visibility graph*. These graphs can be formed in two-dimensional spaces with polygonal obstacles by connecting each obstacle vertex to every other visible obstacle vertex and goal point [87]. Similar graphs can be constructed for non-polygonal obstacles by connecting lines to the features and edges where visibility ends. The constructed visibility graph represents a map of the feasible free space that can be safely traversed without intersecting an obstacle. This graph can be searched to find the shortest path between the goal points, which due to the nature of the visibility graph, is guaranteed to be the shortest feasible path between the goal points.

An obvious issue that arises when traversing a visibility graph is that some points in the graph necessarily lie on constraint boundaries (e.g. the boundary vertices). If obstacle avoidance is a priority, then these paths are likely not desirable. A *Voronoi diagram* is a different type of graph

constructed to maximize the separation from the obstacles. By definition, a Voronoi diagram is the set of points that are equidistant from two or more obstacle boundaries. These points form a graph that partitions the configuration space into regions occupied by each distinct obstacle. This graph can be searched to find the shortest path that maximum obstacle clearance (i.e. distance from the obstacles).

While these two approaches offer guarantees of completeness and optimality they each solve a very specific cost formulation and do not offer optimality for other cost functions. They also do not scale well to more than two dimensions. For example, in three dimensions the Voronoi diagram becomes a group of two-dimensional faces instead of a set of points and cannot be easily searched for the shortest path. For these reasons, these algorithms are used almost exclusively for two-dimensional problems [92].

After the development of exact algorithms, motion planning research has largely transitioned to *heuristic* algorithms that sacrifice guarantees of completeness and optimality for improved practical performance [88, 89]. Although the definition of heuristic is not completely agreed upon, the rest of the algorithms presented in this section are heuristic in that they rely on user-defined parameters and offer no strict guarantees.

3.2.1.2 Classic Algorithms

Aside from the exact algorithms, there are other so-called *classic* algorithms developed early in the field of motion planning that solve the motion planning problem in relatively straightforward ways. One such example, is the creation of artificial *potential fields* that locally guide a point through the configuration space. Popularized in the 1970s and 1980s, these methods rely on potential functions with a minimum at the goal point and maximums at the obstacles [94]. The negative gradients of these potential functions can be followed to guide a point towards the goal and away from the obstacles, analogous to a ball rolling downhill. Although simple to implement, these methods are highly prone to local minima which trap the point robot [92]. As such, they typically require some method to escape local minima and have generally decreased in usage.

Another common "classic" approach is *cell decomposition*. In cell decomposition, the free

space is partitioned into discrete subspaces called cells. This partitioning can be performed irrespective of obstacle position (e.g. from a regular grid) or obstacle information can be used to ensure obstacle boundaries form cell edges [92]. After the cells are established, the obstacle occupancy is determined to define which cells make up the free space. The adjacency of the cells in space is then used to find the shortest feasible sequence of cells from the initial to the goal point. The algorithm possesses *resolution completeness* meaning that a feasible path, if one exists, will be found if the resolution of the cells is fine enough, though fine resolutions can lead to high computational complexity. Because there is no explicit representation of a path, paths cannot be finely optimized for a cost function.

3.2.1.3 Artificial Intelligence

Because "machine planning" is well known to be a type of *artificial intelligence*, the concept of motion or path planning originally arose from that community [90]. As such, there have been many path planning algorithms that employ traditional artificial intelligence techniques [90, 88, 89].

Neural networks have become one of the most popular techniques in artificial intelligence in all scientific fields and have been especially popular in motion planning. A neural network path planner was first conceived in the late 1980s [95]. Since then, many neural networks have been applied to motion planning to solve a diverse set of problems. Due to their adaptability, they often exceed the performance of traditional motion planning algorithms when handling complex tasks like interpreting sensor data, navigating dynamic spaces, or dealing with uncertainty [89].

Motion planning can easily be conceived of as a decision making process [90]. For example, an autonomous vehicle might sense data about its environment and decide which turn to make, when to stop, or when to change lanes. Under this framework, *reinforcement learning* has often been used to train autonomous agents which decisions to make under certain circumstances. Reinforcement learning has also been applied to path planning, specifically in cases where autonomous robots need to learn how to make complicated movements by sensing their environment [96].

Artificial intelligence could be applied to train a computer agent how to design compositionally graded alloys. However, the primary difficulty in applying the aforementioned methods or any

similar technique to gradient design is a lack of significant training data. Both methods require examples of good and bad paths in order to train models. Unfortunately, there are not enough examples of compositionally graded alloys to adequately train such a model. And while computational tools can be used to model potential compositionally graded alloys, their computational expense is such that testing hundreds or thousands of such paths is not an efficient solution.

3.2.1.4 Traditional Optimization

Though many motion planning algorithms exploit the specific characteristics of the path planning problem, traditional optimization methods can also be used to solve the path planning problem formulation. At a basic level, one only needs to parameterize the path into a discrete number of design variables and then represent the cost function and constraints in terms of those variables. Any optimization algorithm can then attempt to minimize the cost function while satisfying the constraints. Such methods have the added benefit of considering nearly any type of cost function or constraint formulation, as long as they can be represented in terms of the design variables.

Parameterized curves have been used extensively to optimize the paths of autonomous vehicles [97]. Unlike traditional motion planning algorithms, these techniques employ parameterizations that produce smooth paths like Bézier curves, polynomials, or splines. This added smoothness provides benefits to comfort, vehicle dynamics, and fuel efficiency. However, most applications of these planning techniques are for simple actions like lane changes or parking assistance, with few obstacles in relatively small spaces [97, 98, 99, 100]. Optimizing parameterized curves becomes more difficult when there are many complex obstacles in a large space. In this case, finding a feasible solution can be non-trivial and gradient-based optimizers will be unlikely to escape infeasible solutions or local minima.

Genetic algorithms have been applied to a wider set of path planning problems because they are well known for finding globally optimal solutions in complex spaces [89]. Genetic algorithms use nature-inspired operations like mutation, cross-over, and reproduction to selectively breed optimal solutions. For path planning, such operations need to be modified to maintain path connectivity. For example, Hu and Yang [101] developed problem-specific operators that produced solutions

with half the cost in half the generations of traditional genetic algorithms. Even with these specialized operations, genetic algorithms often require large populations and many generations to find a globally optimal solution.

Traditional optimization techniques are powerful in that they can be applied to nearly any path planning problem formulation. However, they are often prone to local minima and must be parameterized carefully to maintain path connectivity. They also typically require many evaluations of the cost function and obstacle models for the entire path, whereas other path planning algorithms need only evaluate the cost or collision of a path on a segmented basis. This means that general optimization techniques tend to be less efficient, less scalable, and suboptimal for large, complex planning spaces.

3.2.1.5 Graph Search Algorithms

Some of the most well known path planning algorithms search a predefined graph of paths for one that is optimal to a given cost function, such as searching a road map for the fastest route. These *graph search* algorithms offer a guarantee of finding the optimal path through the provided graph, if it exists. One of the earliest such techniques is Dijkstra's algorithm, published in 1959 [102]. Dijkstra's algorithm can find the shortest path from one to point in a graph to another. The A-star (A*) family of algorithms improves on Dijstra's implementation by providing faster solutions to a wider set of problems [97].

Because costs are computed on a segment-wise basis, cost functions must be commutative. In other words, the cost of an arbitrary path divided into segments must equal the sum of the costs of its segments. However, the primary restriction of graph search algorithms is the fact that they must be provided with a pre-computed graph. This is not a problem for navigation tasks where road maps are readily available, but becomes an issue when navigating unknown state spaces. Creating such a graph can be computationally intensive if the space is large and evaluating cost and collision is expensive. Because the entire graph must be stored in memory, graph search algorithms also have high space complexities which further reduce their scalability.

3.2.1.6 Sampling-Based Planners

Sampling-based planners overcome the primary limitation of graph search algorithms by creating a graph structure during the planning process. Due to their flexibility and scalability, they have become one of the most popular classes of algorithms in the motion planning community [103]. In short, sampling-based planners take samples of the environment (i.e. state space) to build a graph that can be searched for an optimal path.

Probabilistic Roadmaps (PRMs) are one of two major types of sampling-based planners and have been used extensively in motion planning [103]. PRMs randomly sample the state space to find candidate nodes. Nodes are connected to form a graph if the connection does not collide with an obstacle. The cost of the connection is also stored and the graph can be searched for an optimal path from any one node to another. Because the whole graph is stored, PRMs are useful when multiple path planning queries are going to made in the same environment. However, this feature also increases space complexity and therefore memory usage.

Rapidly-exploring Random Trees (RRTs) are the other major type of sampling-based planner and operate similarly to PRMs but offer a key distinction. RRTs are intended to be a single-query solution and build a tree instead of a graph. A tree contains only the lowest cost connections between nodes, storing a single connection between a node and one parent node. This means that trees contain less connections and occupy much less memory than roadmaps. While this a benefit for single-query problems, if a different path is to be planned in the same environment, the environment must be resampled to make new optimal connections.

PRM and RRT are proven to be *probabilistically complete* in that the probability of failing to find a feasible path, if it exists, decays to zero as the number of samples increases [91]. Nonetheless, sampling-based planners were widely seen to be suboptimal to other path planners due to their reliance on random samples. However, in 2011, Karaman and Frazzoli [91] presented novel formulations of PRM and RRT that retained probabilistic completeness and were also proven to be *asymptotically optimal*. Asymptotic optimality ensures the algorithm converges to the globally optimal solution as the number of samples increases. These new optimal algorithms, PRM* and

RRT*, have quickly become widespread in the motion planning community [103].

Because of their reliance on nodal structures, PRM* and RRT* have similar cost restrictions to those imposed on A* algorithms, which will be discussed further in Section 3.2.2. Despite this limitation, PRM and RRT are known to be flexible and easily scalable [103]. They have even be applied outside traditional motion planning in the computational structural biology community [104]. Here they have been used to simulate protein folding [105], transitions between molecular conformations [106], and protein-ligand interactions [107].

3.2.1.7 Summary

Table 3.1 summarizes the advantages and disadvantages of each of the path planning algorithms discussed above. *Exact* algorithms offer convenient guarantees, but are not scalable beyond two dimensions and were developed to optimize specific cost functions. Other *classic* algorithms, like potential fields and cell decomposition, offer techniques that are simple to implement, but are no longer widely used because they provide suboptimal solutions. Algorithms that employ *artificial intelligence* are adaptable to a wide variety of problems and are generally highly scalable. However, these techniques, like neural networks or reinforcement, require a significant amount of training data which is simply not available for compositionally graded alloys. *Traditional optimization* techniques parameterize paths into a discrete number of design variables and can optimize virtually any cost function, but they typically do not easily satisfy constraints and require numerous cost and collision evaluations to provide globally optimal solutions. *Graph search* algorithms, like A*, are popular, but require pre-computed graphs that are likely prohibitively expensive to construct for a gradient design problem. *Sampling-based planners* build graphs iteratively by sampling the environment and have been shown to provide guarantees of probabilistic completeness and asymptotic optimality. They are also highly flexible and have been applied in fields outside of the motion planning community.

For these reasons, sampling-based planners were chosen as the best class of algorithms to implement into a design methodology for compositionally graded alloys. They can be easily implement by simply providing models for the cost function and obstacle model that can be sampled

Table 3.1: Advantages and disadvantages of common path planning algorithms

Category	Algorithm	Advantages	Disadvantages
Exact	Visibility Graph	Minimizes path length, complete and optimal	Not scalable, no cost flexibility
	Voronoi Diagram	Maximizes clearance, complete and optimal	Not scalable, no cost flexibility
Classic	Potential Fields	Simple implementation, some cost flexibility	Highly prone to local minima, no guarantees
	Cell Decomposition	Simple implementation, resolution complete	Poorly defined paths, no optimality
Artificial Intelligence	Neural Networks	Highly scalable and adaptable, high cost flexibility	Requires substantial training data, no guarantees
	Reinforcement Learning	Adaptable to many actions, high cost flexibility	Requires substantial training data, no guarantees
Traditional Optimization	Parameterized Curves	Solvable by many optimizers, cost flexibility	Prone to local minima, cannot easily avoid obstacles, no guarantees
	Genetic Algorithms	High cost flexibility, can find global optima	Requires many cost and collision evaluations, no guarantees
Graph Search	A*	Complete and optimal for given graph, faster than Dijkstra's	Requires precomputed graph, high space complexity, some cost restrictions
Sampling-based	PRM*	Multi-query, probabilistically complete and asymptotically optimal	High space complexity, some cost restrictions
	RRT*	Memory efficient, probabilistically complete and asymptotically optimal	Single-query, some cost restrictions

as functions of the state space. In this dissertation, an implementation of RRT* was chosen over PRM* because of its lower space complexity. Because gradient design problems can involve large, complex spaces of many dimensions, storing an entire connected graph could reach memory limitations or be prohibitively expensive to search for an optimal path. On the other hand, a tree stores only the optimal connections and connects nodes in an optimal fashion, such that the optimal path is much simpler to retrieve. The primary limitation of RRT is that it is a single-query process so if new gradient paths are to be designed in the same state space (e.g. alloy system) a completely new tree will need to be built from scratch. However, with the use of surrogate models, the computational time of RRT is minimized and new surrogate models will not have to be trained for the same system under the same constraints and costs. The specific implementation of RRT* employed in this methodology is detailed in the next section.

3.2.2 Rapidly-exploring Random Tree

*3.2.2.1 Fixed Nodes Implementation of the Optimal Rapidly-exploring Random Tree (RRT*FN)*

Sampling-based path planning algorithms, like PRM and RRT, were developed in the late 1990s to plan paths in large or high dimensional spaces where explicit representation of the obstacles might be difficult. However, these algorithms were considered to be sub-optimal until, in 2011, Karaman and Frazzoli developed optimal versions, PRM* and RRT*, that they proved to be probabilistically complete and asymptotically optimal [91]. Two years later, in 2013, Adiyatov and Varol developed a fixed-node version of RRT* that sacrifices these guarantees for computational efficiency by limiting the number of nodes added to the tree [3]. This implementation was chosen for the gradient design methodology because it can offer the same guarantees as RRT* when the node limit is not active and can also allow larger problems to remain tractable within computer memory limitations.

Algorithm 1 describes the basic procedure of RRT*FN. It begins by defining an initial start point z_{init} and initializing a tree object, τ, which will store the vertices or nodes of the tree as well as the edges that connect them. A *Sample* routine then generates a new random sample in the state

space, z_{rand}. The node in the tree that is closest in state space to z_{rand} is known as z_{nearest} and is determined by the *Nearest* function ($z_{\text{nearest}} = z_{\text{init}}$ at the first iteration). The *Steer* step ensures the new point is close to z_{nearest} by finding the point z_{new} along the line formed between z_{nearest} and z_{rand} that is within a predefined distance from z_{nearest}.

Algorithm 1: RRT*FN [3]

$\tau \leftarrow$ **InitializeTree**(z_{init})
for *i = 1,...,n* **do**
  $z_{\text{rand}} \leftarrow$ **Sample**
  $z_{\text{nearest}} \leftarrow$ **Nearest**(τ, z_{rand})
  $z_{\text{new}} \leftarrow$ **Steer**$(z_{\text{rand}}, z_{\text{nearest}})$
  if ObstacleFree$(z_{\text{new}}, z_{\text{nearest}})$ **then**
    $Z_{\text{near}} \leftarrow$ **Near**(τ, z_{new})
    for $z_{near} \in Z_{near}$ **do**
      if Cost$(z_{\text{near}}, z_{\text{new}}) < c_{\text{min}}$ **and ObstacleFree**$(z_{\text{near}}, z_{\text{new}})$ **then**
        $z_{\text{parent}} \leftarrow z_{\text{near}}$
        $c_{\text{min}} \leftarrow$ **Cost**$(z_{\text{near}}, z_{\text{new}})$
      end
    end
    $\tau \leftarrow$ **InsertNode**$(z_{\text{new}}, z_{\text{parent}}, \tau)$
    $\tau \leftarrow$ **Rewire**$(Z_{\text{near}}, z_{\text{new}}, \tau)$
    if $n_{nodes} = n_{max}$ **then**
      $\tau \leftarrow$ **ForcedRemoval**(τ, Z_{goal})
    end
  end
end
return τ

Once the new candidate point, z_{new}, has been found it can be added to the tree, τ. This process begins by first checking if the straight line path between z_{new} and z_{nearest} is *ObstacleFree* or does not collide with an obstacle. While the previous steps relied on simple and efficient calculations, this step requires the evaluation of an obstacle model. In general, obstacle collision can be detected by sampling the obstacle model at z_{new}, z_{nearest}, and several samples between them. If any sample is found to be in the obstacle region, then the connection is not deemed to be obstacle-free. Because evaluating the obstacle model is generally much more computationally intensive than distance calculations, collision detection can often be a significant portion of the total runtime of RRT*.

If the connection between a candidate node and its nearest node is obstacle-free, then a parent node needs to be chosen. First, all the nodes in the tree that are within a predefined radius of the new point, Z_{near}, are identified with the function Near. Each of these nearby points $z_{\text{near}} \in Z_{\text{near}}$ is then analyzed to determine which forms the minimum cost path to z_{new} while also forming an obstacle-free connection. Evaluating the *Cost* of a connection can be relatively efficient if the cost function is path length. However, if a more complex cost function or a regression model are used, then the contribution of cost evaluation to the total runtime can rival collision detection. This node becomes the parent node, z_{parent}, that the new node will be connected to in the tree. The *InsertNode* method updates the tree by storing the new node, the new connection to its parent node, and the cost to the new node.

After the new node has been added to the tree, the *Rewire* routine determines if connections in the tree can be optimized to minimize their cost. This is done by checking if the costs to any of the nodes $z_{\text{near}} \in Z_{\text{near}}$ will be cheaper if z_{new} was that point's parent node. If z_{new} is the cheaper parent node and the connection between z_{near} and z_{new} is obstacle-free , than the connections in the tree are updated.

Lastly, the novel contribution of RRT*FN is the introduction of a *ForcedRemoval* method to remove excess nodes. If the number of nodes currently added to the tree, n_{nodes}, exceeds a set limit, n_{max}, then a node with no children is removed. If more than one node has no children, then one is randomly selected. This prioritizes nodes with high associated costs and prevents the deletion of a

path that reaches the goal.

Figure 3.2 depicts some of the major steps of RRT*FN in a simplified example.

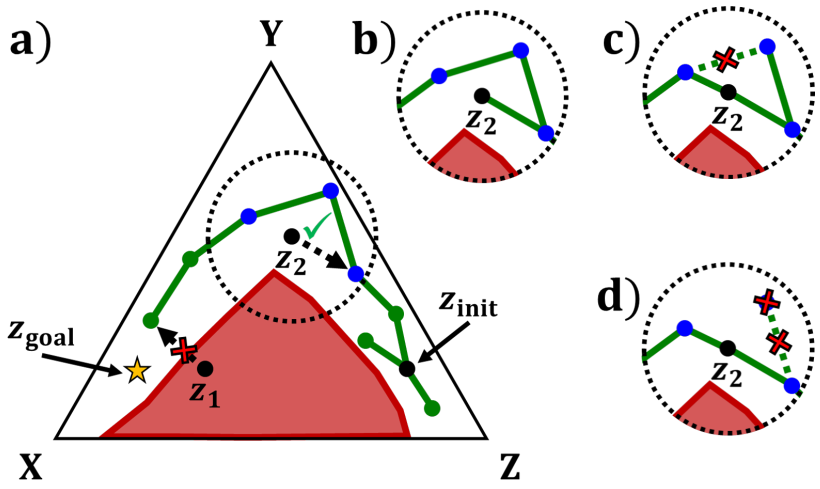

Figure 3.2: a) A simplified example of the RRT*FN algorithm planning a path in a hypothetical X-Y-Z composition space. Random sample z_1 is not connected to the tree because it lies in the obstacle region. Random sample z_2 however can form collision-free connections to any of three neighboring nodes in a predefined radius (shown as a dashed circle). b) The node that minimizes path cost (e.g. path length) to z_{init} is chosen to connect with z_2. c) During *rewiring*, a new connection is made to z_2 that reduces the cost of the path to another node in the tree. d) If the fixed number of allowed nodes is exceeded in the tree, extraneous nodes are removed during the *removal* step. Reprinted with permission from Eliseeva et al. (2019) [2]

3.2.2.2 Complexity

The complexity of many of the most common sampling-based planners, including PRM and RRT as well as PRM* and RRT*, was characterized by Karaman and Frazzoli [91].

PRM, PRM*, RRT, and RRT* share the same time complexity of the processing phase: $O(n \log(n))$, where n is the number of samples or, alternatively, iterations. The processing phase of each algorithm is the phase where the map or tree is constructed by sampling the space, checking for obstacles, computing costs and connecting nodes. The complexity of this phase will scale with the complexity of the collision checking and cost evaluation procedures. So if these operations are

more complex, or scale worse with the number of samples, then they can increase the complexity of the processing phase.

The query phase is the phase where the map or tree is searched for the optimal path. The time complexity of the query phase for PRM* is $O(n \log(n))$, but the time complexity of the same phase for RRT* is $O(n)$, because trees have fewer edges that need to be searched.

The space complexity, or the scaling of occupied memory, of both the PRM and RRT families of algorithms is equivalent to the number of edges stored. For PRM*, the space complexity is $O(n \log(n))$, however the space complexity of RRT* is $O(n)$. As with the time complexity of the query phase, this reduction in space complexity is also due to a reduction in the number of stored edges.

3.2.2.3 Restrictions on the Cost Function

As discussed by Karaman and Frazzoli [91], for any optimal sampling-based path planning algorithm (e.g. PRM*, RRT*, RRT*FN) to be asymptotically optimal, cost functions must be *strictly positive*, *monotonic* and *bounded*. To be strictly positive the cost of a path can only be zero if and only if the path never moves from its starting position (i.e. $c(\sigma) = 0$ if and only if $\sigma(\alpha) = \sigma(0),\ \forall \alpha \in [0, 1]$). A monotonic cost function satisfies the condition that $c(\sigma_1) \leq c(\sigma_1|\sigma_2)$ for all $\sigma_1, \sigma_2 \in \Sigma$, where $\sigma_1|\sigma_2$ represents the concatenation of paths. The concatenation of paths is an operation performed on paths $\sigma_1, \sigma_2 \in \Sigma$ where $\sigma_1(1) = \sigma_2(0)$. The concatenated path is defined by Eqn. 3.1, where $r = \frac{l_{\sigma_1}}{l_{\sigma_1}+l_{\sigma_2}}$ is the ratio between the length of path σ_1 and the combined lengths of paths σ_1 and σ_2. This definition of concatenation remains consistent with the definition of path index as a normalized length, as seen in Eqn. 2.1.

$$(\sigma_1|\sigma_2)(\alpha) := \begin{cases} \sigma_1\left(\frac{\alpha}{r}\right) & \forall\, \alpha \in [0, r] \\ \sigma_2\left(\frac{\alpha - r}{1 - r}\right) & \forall\, \alpha \in [r, 1] \end{cases} \tag{3.1}$$

The current implementation of RRT*FN and many other tree- or map-based planners also require cost functions to be *additive*. For a cost function to be additive, it must satisfy the condition

that $c(\sigma_1|\sigma_2) = c(\sigma_1) + c(\sigma_2)$ for all $\sigma_1, \sigma_2 \in \Sigma$. In other words, the planner stores segment costs independently and then sums the cost of each segment in a path to compute the total path cost. This is not however a strict requirement for the guarantee of asymptotic optimality. The algorithm could be modified to store costs in some other manner if a non-additive cost function were desired.

3.2.2.4 Sampling a Simplex

As discussed in Section 2.2 and Eqn. 2.3, the typical state space of a gradient path design problem is a composition space. Because the total composition at any point in an N-dimensional composition space must sum to unity, one element can be removed and considered a balance element to form an $(N-1)$- simplex. Generating uniform random samples on a simplex can be a non-obvious task. One naive approach would be to generate an N-dimensional sample from some uniform pseudo-random sampling method (e.g. Halton sequence) and then normalize the sample by its sum. However, this tends to generate samples that are biased towards the center of the composition space [108, 109]. Uniformly distributed samples on the $(N-1)$-simplex follow an N-dimensional Dirichlet or multivariate Beta distribution, as shown by Woronow [108]. Such a distribution can be generated from a uniform random distribution, U, via the inverse transformation $-\ln(U)$. The following procedure, described by Otis [109], exploits this property to produce random samples, x^N_{simplex}, that are uniform on the unit $(N-1)$-simplex :

1. Let N represent the number of elements in the composition space
2. Generate an N-dimensional sample, x^N, from a uniform pseudo-random technique
3. Transform each element in the sample to be exponentially distributed: $x_{i,\text{exp}} = -\ln(x_i)$
4. Divide each element in the exponentially distributed sample by the sample's sum:

$$x_{i,\text{simplex}} = \frac{x_{i,\text{exp}}}{\sum_{i=1}^{N} x_{i,\text{exp}}}$$

This procedure is used throughout the methodology whenever random samples of composition space are generated, as in the *Sample* method of RRT*FN. It is also used to generate uniform random samples to train surrogate models for both constraints and costs.

3.3 Constraint Models

The presented methodology offers the ability to impose constraints or design requirements on potential gradient paths. These constraints are manifested as functions of the state space (e.g. composition and/or temperature) that can be used to identify obstacle regions. In order for the path planning algorithm to evaluate collision with these obstacles, some function or model must be made to predict if a point in the state space lies within the obstacle region. This section details how CALPHAD can be used to predict many types of design requirements. Furthermore, it outlines how surrogate models can be used to reduce the computational cost of constraint evaluation or collision checking.

3.3.1 CALPHAD Modeling

The primary modelling tool used in the presented methodology to predict the properties or performance of potential gradient alloys is CALculation of PHAse Diagram or CALPHAD software [82]. The CALPHAD method offers the unique ability to predict phase formation, solidification characteristics, temperature-dependent behavior, and certain physical properties for arbitrary alloy compositions. The basic idea of CALPHAD is the monitoring and optimization of Gibbs energy. Equations for the Gibbs energy of a material phase can usually be constructed in terms of composition, temperature, and pressure. The typical procedure of the CALPHAD method begins by producing equations of this nature for the Gibbs energies of all phases a system might encounter. These equations often involve parameters that must be fit to empirical information derived from experiments or high fidelity simulations. The fitting of parameters to empirical data is commonly known as a CALPHAD *assessment*. A CALPHAD *database* consists of phase free energy models and the parameters that were fit to construct them.

The Gibbs energy functions represented in a CALPHAD database can be used to determine quantities like equilibrium phase fractions and thermodynamic properties. For example, equilibrium phase fractions can be determined from the convex hull of phase Gibbs energies at a given thermodynamic condition (e.g. composition and temperature). This concept can be taken further

to construct entire phase diagrams in composition-temperature space, which depict the boundaries at which phases enter or leave the convex hull. Similarly, thermodynamic properties like solidus or liquidus temperature can also be extracted from phase Gibbs energies. Other quantities like diffusivity and thermal conductivity can be represented in functional forms similar to those used to model Gibbs energies. Adding these quantities to CALPHAD databases expands the capability of CALPHAD to predict non-equilibrium kinetics and additional relevant properties [82]. Software tools, like Thermo-Calc [110], use CALPHAD databases to predict phase formation as well as a diverse set of thermodynamic properties.

A key innovation that has enabled the use of CALPHAD techniques for gradient design is the development of large, multi-component CALPHAD databases. The development of these databases has largely been driven by interest in high entropy alloys, which have multiple principal elements and often exhibit favorable properties. For example, Thermo-Calc's TCHEA series of databases [111] is used many times in this dissertation. While other CALPHAD databases are often limited to a few elements, TCHEA1 introduced a database with 15 relevant elements and 163 modeled phases that were assessed for 105 binaries and 200 ternaries [111]. Nearly two decades later, TCHEA3 expanded the database to 26 elements and 400 ternaries [112]. In order for a CALPHAD database to be trusted, it is traditionally assessed for all relevant binary and ternary combinations of its constituent elements. Due to the combinatorics of these assessments, it requires a substantial effort to obtain sufficient empirical data and fit models in such large spaces. As such, large, multi-component CALPHAD databases are rare and have, to date, only been released as proprietary components of commercial software.

Large, multi-component databases like TCHEA often do not assess every ternary combination of constituent elements. For example, in TCHEA3 400 ternaries are at least partially assessed, but only 136 are assessed in the full range of composition and temperature [112]. However, there are ${}_{26}C_3 = 2600$ relevant ternary or three-element systems that could be assessed in the total 26-element space. Consequently, there is a large portion of composition-temperature space where models have not been fit to empirical data and could be inaccurate. This is a current limitation of

CALPHAD modeling in large spaces, but spaces near common alloys should be well-assessed and the published list of assessed ternaries [112] can be used to approximate accuracy.

Another limitation of CALPHAD modeling in multi-component databases is the computational efficiency of calculations. Because many phases could be present at a given thermodynamic condition, each phase Gibbs energy function must be considered when calculating the phases present at equilibrium. While equilibrium phase calculations at a single condition typically only take a fraction of a second, this calculation must be preformed hundreds of thousands or millions of times if used directly in the collision checking or cost evaluation procedures of a path planning algorithm, which are often limited by the time spent in these procedures. The replacement of a CALPHAD model by a suitable surrogate model can reduce the computation time of these procedures and drastically reduce the total runtime of the presented methodology.

3.3.2 Surrogate Models: Classification

The surrogate modelling technique that best represents design constraints is machine learning classification. Classifiers predict a discrete category or label for a new input. As such, they can be naturally trained to predict whether a point in the state space satisfies or violates specified design constraints. The general procedure of training a surrogate classifier begins by first gathering samples of relevant CALPHAD data (e.g. equilibrium phase fractions predicted at various compositions for a constant temperature). Design constraints, like maximum allowable fractions of each phase, are then applied to each sample to generate a label of *satisfactory* or *unsatisfactory* for each composition. This labeled data is then used to train a machine learning classifier that can predict if a composition violates the constraints. This model can then be implemented into a simple collision checking procedure to determine if a path through composition space collides with the obstacle region.

This section presents two methods of training classifiers on CALPHAD data: *active* and *a priori* sampling. Both methods offer unique advantages and are used in case studies in this dissertation.

3.3.2.1 Active Sampling

To minimize the number of CALPHAD samples or calls to a CALPHAD model, a sampling procedure could be devised to choose samples intelligently. Such a scheme could reduce the total runtime of the methodology, if it could accurately model the constraints in a minimal number of CALPHAD samples. Many so-called active sampling schemes exist to iteratively choose samples based on a trained surrogate model and then use them to update the model. One such scheme that has been applied to model phase regions is the *Constraint Satisfaction Algorithm (CSA)* developed by Galvan et al. [5, 113].

The CSA trains a Support Vector Data Description (SVDD) [114] (with a radial basis function kernel and a kernel parameter of 0.5) that represents the regions in the design space that satisfy or violate a given set of constraints. Similar to Support Vector Machines [115, 116], SVDD is a nonprobabilistic machine learning classifier that explicitly represents the decision boundary in feature space. However, SVDD is a one-class classifier that requires less samples to accurately model constraint regions that are small relative to the total space.

The CSA begins with an initial dataset, provided either from prior knowledge, a sparse exploratory sampling, or a conventional optimization routine. This initial data is used to train a crude SVDD around the points that satisfy the constraints. New samples of the design space are then taken perpendicular to the SVDD boundary in the region where the boundary is least defined. A root-finding method is used to guide these samples to a point that lies on the true boundary. This active or adaptive sampling scheme allows the CSA to find desired boundaries more efficiently than traditional space-filling techniques. This process is repeated and the SVDD is grown until a specified maximum number of samples has been taken.

Active sampling techniques like the CSA offer the benefit of computational efficiency because they tend to only sample in areas that will improve the surrogate model. Because sampling is more dense near the decision boundary, these methods can also produce more accurate classifiers than sparse a priori sampling of the entire design space. However, if the obstacle region is disjoint in the design space, active sampling techniques might miss some regions entirely. Also, active sampling

techniques require a fixed definition of the constraints. If the constraint formulation changes, a new decision boundary is needed and new active sampling process must begin. While the samples from previous constraint formulations can be reused, they are likely to be biased towards the old decision boundary and might negatively impact the accuracy of a new model. These limitations inhibit the efficacy of active sampling techniques for larger, more complex problems where obstacles might be missed or constraint formulations might change.

3.3.2.2 A Priori Sampling

In contrast to active sampling, classifiers can also be trained on samples gathered before the training process, or a priori. While this process can be less efficient than active sampling, it also offers benefits to flexibility and global accuracy that make it more attractive to most gradient design problems.

Training a classifier from a priori sampling first requires a uniform sampling of the design space. Several space-filling sampling techniques exist for such a sampling scheme, such as Latin hypercube sampling. Many techniques could be viable, but most case studies in this dissertation employ uniform pseudo-random Halton sequence samples that are transformed by the procedure described in Section 3.2.2.4 to be uniform in composition space. Once a space-filling sampling of CALPHAD data (e.g. equilibrium phase fractions or thermodynamic properties) has been obtained, design constraints can be applied to determine which samples violate the constraints. Anytime constraint formulations are updated, samples can simply be relabeled without needing to resample expensive CALPHAD models.

After labeling the sampled data, almost any machine learning classifier is capable of training a surrogate model to predict constraint violation. In this dissertation, simple k-Nearest Neighbors ($k = 3$) classifiers are used because they are simple to train and predict, can represent nearly any shape of obstacle region, and are scalable to large dimensions. In k-Nearest Neighbors classification, an input is assigned a label based on the plurality vote of its k nearest neighbors. By limiting k to 3, the time taken to classify a new input and the tendency to smooth decision boundaries is decreased. Because the classifier is a surrogate model of trusted CALPHAD models, overfitting to

local data is not a significant concern in this application.

One limitation of an a priori sampling approach is deciding on the number of samples to take. If too few samples are taken, then trained classifiers could be inaccurate or miss obstacle regions entirely. For this reason, it is generally recommended to take dense samplings of the total space. As a general rule, at least 10^d samples should be taken in a d-dimensional state space, though hundreds of thousands of CALPHAD samples could take days to calculate and more samples might be required if the accuracy of the constraint boundaries is important. Statistics on the nearest neighbor distance of the samples can be used to approximate the resolution and accuracy of a surrogate classifier before training.

3.3.2.3 Model Validation

Surrogate models should be validated after training to ensure they accurately represent the obstacle region. Cross validation is a popular validation technique in which training data is randomly split into folds. Each fold is then used as a test set to measure the accuracy of a model trained on the remaining data. If the training input is a uniformly distributed random variable, cross validation can be a suitable validation technique as each randomly selected subset or fold should be somewhat representative of the total dataset.

Popular metrics for measuring the accuracy of a classifier are misclassification rate, precision, and recall [5]. These metrics are used to validate the classification of phase regions in Section 4.2.2.

3.4 Cost Functions

In addition to constraints, design goals can also be represented as cost functions in the presented methodology. Cost functions best represent goals or objectives that offer a continuous scale of design improvement. These should be performance metrics that a designer wishes to minimize or maximize as opposed to design requirements with hard thresholds. In the motion planning community, the most common cost function is path length as shorter paths are generally always better. However, another popular cost function is obstacle clearance which maximizes the path's separation from obstacles in order to minimize the likelihood of a collision. These cost functions

offer similar benefits to gradient design and are relatively straightforward to implement.

While conventional motion planning cost functions can be useful to gradient design, it is possible to formulate a wide variety of gradient design objectives as cost functions. One of the most important considerations when designing a functional gradient is its properties. Later in this dissertation, in Chapter 7, a novel cost function is presented that designs gradients to optimize their properties. However, this cost function and any other cost functions that involve gradient-dependent quantities require models to predict those quantities. For example, CALPHAD modeling can predict properties as a function of state that can then be given to a cost function to compute a cost. However, like with constraint modeling, these models are often too expensive to sample millions of times if sampled directly by the path planning algorithm. As such, surrogate models of these quantities will need to be made to reduce computational expense.

3.4.1 Surrogate Models: Regression

Unlike constraint models, the models of cost functions or the continuous variables on which they depend require surrogate modeling techniques that can model continuous output. These techniques are collectively referred to as *regressors*. In machine learning regression, a model is trained on continuous data instead of the discretely labeled data that a classifier could be trained on.

To train surrogate models for a cost function, the natural solution might be train a model on the cost directly, but it might also be better to train a model on relevant quantities, like material properties, instead. For instance, if a cost function applies only simple operations to a material property then the computational expense of those operations is likely dwarfed by the expense of sampling the surrogate model. This means that creating a model of the property instead of the cost will not increase expense. Furthermore, the property might be more well behaved for regression modeling than the cost itself, like when costs have limits towards infinity or are have many plateau regions. Lastly, some costs can be path dependent, like the maximum value of property over a path, and cannot be modeled directly as a function of state space.

Creating a regression model begins with the collection of training data. If the relevant properties can be predicted by CALPHAD, it might be best to gather cost-relevant data (e.g. material

properties) at the same time as constraint-relevant data (e.g. material phases). If a composition space is being sampled, the same procedure described in Section 3.2.2.4 for producing uniform random samples in a simplex is also recommended for property sampling. However, some properties that cannot be modeled by CALPHAD may require training on experimental data that is not uniformly distributed. Regression models can still be made on this data, but special precautions should be to account for training or validation biases.

Many machine learning regression models could be chosen to model costs or cost-relevant data. To be suitable for path planning, regression models should minimize evaluation time as much as possible. They should also be valid and somewhat accurate for the entire free state space if the entire free state space is to be searched for an optimal path. Two types of machine learning regressors that generally meet these requirements of efficiency and scalability are *support vector machine regression* and *Gaussian process regression*. Support vector machine regression is easily scalable to high dimensions and is relatively memory efficient as only a subset of the training data is stored. On the other hand, Gaussian process regression uses more memory as all the data needs to be stored, but also interpolates between training data (i.e. does not mispredict trusted data) and can naturally provide uncertainty estimates. Both modeling techniques are demonstrated in this dissertation to model properties.

3.4.1.1 Model Validation

As with surrogate models for the constraints, regression models should also be validated after being trained. As discussed previously, cross validation can be a useful method to measure the accuracy of a regressor if a test set is not readily available. The most common metrics to measure the accuracy of a regressor are the coefficient of determination (R^2) and Root Mean Square Error (RMSE). Both of these metrics are used to validate regression models in this dissertation.

4. CONSTRAINTS FOR DELETERIOUS PHASES *

The most common issue with compositionally graded alloys is deleterious phase formation. This chapter describes how undesirable phase regions can be treated as obstacles in the presented methodology. CALPHAD modeling is used to predict equilibrium phase formation and then machine learning classifiers are used to create surrogate models of the obstacle region. Designers must decide how to formulate phase constraints by considering the relevant temperatures or solidification processes, but the methodology can consider any combination of constraint formulations. A simple illustrative case study is given in the Fe-Ni-Cr system to show how the methodology can be used to avoid phases at a range of temperature. Experimental evidence validates that the designed gradient successfully avoids deleterious phases.

4.1 Deleterious Phases

Deleterious phase formation is likely the single most prominent issue facing the development of compositionally graded alloys. As discussed in Section 1.3.1.1 and shown in Table 1.1, linear compositional gradients between most alloys form new phases, like brittle intermetallics, that can significantly harm the integrity of the build, even causing it to crack during manufacturing.

Phases can naturally be grouped into regions in the state space of gradient alloys. A very common example is a phase diagram, which shows regions occupied by various phases in composition-temperature space. As such, phase regions can be easily represented as obstacle regions to be avoided by a path planning algorithm. Treating phases as constraints in this way also aligns well with gradient design intuition: the ideal gradient path would contain zero deleterious phases or phase fractions below a specified threshold.

*Contains material reprinted with permission from T. Kirk, E. Galvan, R. Malak, and R. Arróyave, "Computational Design of Gradient Paths in Additively Manufactured Functionally Graded Materials." *Journal of Mechanical Design.* 140, no. 11 (November 1, 2018) [4] and O. V. Eliseeva, T. Kirk, P. Samimi, R. Malak, R. Arróyave, A. Elwany, and I. Karaman. "Functionally Graded Materials through Robotics-Inspired Path Planning." *Materials & Design.* 182 (November 15, 2019) [2].

4.1.1 Modeling Deleterious Phases

To consider deleterious phases as constraints in the presented methodology, they must be modeled in some function that can be checked for collision. The general process of modeling constraints described in Section 3.3 can be easily applied to the modeling of deleterious phases. In short, CALPHAD samples are taken and then a surrogate classifier is trained that be cheaply sampled to check paths for obstacle collision.

One complication of modeling phase regions is the important of temperature as a state variable. Inherently, compositionally graded alloys do not need to be designed for temperature, as only composition truly defines the gradient path. Nevertheless, temperature is essential to determining the equilibrium phase at a given composition. How to consider temperature in the constraint formulation for deleterious phases is an important consideration the designer must make. A simple approach is to consider a wide range of temperatures and avoid any deleterious phases at any of these temperatures. This approach is conservative, as it is unlikely the material will remain at all of these temperatures long enough to reach equilibrium, but it is likely to capture whichever phases will form during the manufacturing process.

When considering a range of temperatures, it is necessary to distribute CALPHAD samples in both composition and temperature space. If the path is to be planned in just composition space, the final obstacle model must accept only composition as input. One solution is to train a surrogate model in composition-temperature space and then sample that model in for many compositions and for many temperatures at each composition. Those compositions that intersect the obstacle region at at least one temperature can then be used to construct an obstacle model in only composition space. This method is much cheaper than using calculating the equilibrium phases at all temperatures for every sampled composition, but could be less accurate.

Another approach to forming phases constraints is to consider only phases that are likely to form during solidification. This can be done with solidification simulations that are described in more detail in Section 5.1. Equilibrium solidification simulations will give the equilibrium phases at the compositions solidus temperature, while Scheil solidification simulations can more

accurately predict the phases that form during the rapid solidification of the additive manufacturing process.

Lastly, phases could be considered at just a single temperature. This approach could be useful if the gradient is to be subjected to a well controlled post-processing technique like annealing or hot isostatic pressing. If the temperature of this process is well known and the gradient is held at the temperature long enough to allow kinetics to reach equilibrium, then equilibrium phases at this temperature could be indicative of the final phases in the gradient. However, deleterious phases that form during additive manufacturing could still negatively impact the build or induce cracks even if they are not predicted to appear after post-processing.

Any or all of these constraint formulations for deleterious phases could be used in combination. A single sample set of compositions could be tested for any combination of temperatures or simulations and then subjected to the desired constraints to arrive at a single obstacle model in composition space. Also, a surrogate classifier model could be created for each individual constraint formulation and then tested by a sample set of compositions to construct a single model. This method of using nested surrogate models could be more prone to error propagation, but is also more flexible to changing constraint definitions. For this reason, the nested surrogate model is used more commonly in this dissertation.

4.2 Case Study: Steel to Chromium

The following case study demonstrates the use of the presented methodology to design a gradient path that avoids deleterious phases at a range of temperatures. For this example, a simple ternary composition space so that each step of the methodology could be visualized and more easily understood. Two cost functions, path length and obstacle clearance, are used to show how each affects the optimal path. The stochastic variance of paths planned by both cost functions is studied, as is the number of constraint model evaluations as a function of algorithm iterations.

4.2.1 Problem Description

The iron-nickel-chromium (Fe-Ni-Cr) system was chosen for this case study given its wide spread use in the steel, additive manufacturing, and functionally graded materials communities [1, 59]. In this system, two phases have been identified as detrimental to the manufacturing and performance of additively manufactured parts. The first of these is the so-called sigma phase, which is a complex ordered crystal structure that is generally found at high temperatures and has been shown to decrease toughness, elongation and corrosion resistance [117, 118]. The other identified deleterious or undesirable phase is $CrNi_2$, which occurs at relatively low temperatures. As an intermetallic, this phase is likely to embrittle the gradient and generally decrease part performance [58, 59]. The allowable limit of both phases was set to one mole percent to avoid any significant concentration of either phase. The temperature range for the case study was set to between room temperature (approx. 300 K) and an estimate of the manufacturing temperature of an additive manufacturing process (1100 K). The two-dimensional state space of the gradient design problem can be seen in Eqn. 4.1.

$$z = \left\{ x_{\text{Fe}}, x_{\text{Ni}} : x_{\text{Cr}} = 1 - \sum_{i=1}^{2} x_i \text{ and } x_i \geq 0 \ \forall \, i \right\} \tag{4.1}$$

Given its popularity in industry and close proximity to sigma phase, 316L Stainless Steel (316L SS) was chosen as one of the target compositions. More than 50 percent of the linear gradient path from 316L SS to pure Cr lies in the sigma phase region. As such, pure Cr was chosen as the second target composition of the FGM candidate. Additional manufacturing constraints were imposed on the problem to simulate manufacturing conditions. These constraints restrict the composition space to ensure the gradient path can be made from only three powders: pure Cr, pure Ni, and 316L SS. For the purposes of this case study, 316L SS was approximated by ignoring trace elements (<1%) and considering its composition to be 72% Fe, 12% Ni, and 16% Cr [at%]. The optimization problem formulation is summarized below:

$$
\begin{aligned}
&\textbf{Find} && \sigma_{\text{best}} = \underset{\sigma}{\textbf{arg min}}\ c(\sigma) \\
&\textbf{subject to} && \sigma(\alpha) \in Z_{\text{free}}\ \forall\, \alpha \in [0,1], \\
& && Z_{\text{free}} = \Big\{ z : f_{\text{sigma}}(z,T), f_{\text{CrNi}_2}(z,T) < 0.01\ \forall\, T \in [300K, 1100K], \\
& && \qquad\qquad 0.12x_{\text{Fe}} \leq 0.72x_{\text{Ni}},\ 0.16x_{\text{Fe}} \leq 0.72(1 - x_{\text{Fe}} - x_{\text{Ni}}) \Big\}, \\
& && \sigma(0) = z_{\text{init}} = \big\{ x_{\text{Fe}} = 0, x_{\text{Ni}} = 0 \big\}, \\
& && \sigma(1) = z_{\text{goal}} = \big\{ x_{\text{Fe}} = 0.72, x_{\text{Ni}} = 0.12 \big\}.
\end{aligned}
$$

4.2.2 Phase Modeling

An approximation of the locations of the deleterious phases in composition-temperature space can be seen in Fig. 4.1. This approximation was obtained from a dense full factorial sampling of CALPHAD via the Thermo-Calc TCHEA1 database [110, 111] and was used to validate the surrogate model's approximations of undesirable phase regions. Figure 4.1 also displays the maximum phase fraction found along the temperature dimension at each composition for each phase. Note that in both regions the phase fraction decreases to a minimum at the edges that face the center of the composition space. In Fig. 4.1, the $CrNi_2$ phase and sigma phase are shown to exist at two separate temperature regimes. It would therefore be impossible to use a single isothermal analysis to plan a path that avoids these two phases.

The Constraint Satisfication Algorithm (CSA) described in Section 3.3.2.1 was used to create a surrogate model of deleterious phase regions by actively sampling CALPHAD directly. To avoid representing a multivolume region with a single Support Vector Data Description (SVDD), the CSA was run independently for each of the two undesirable phases. In each case, ten points at a constant temperature (600 K for $CrNi_2$ and 1000 K for sigma phase) were given to initialize the algorithm. The CSA was then run for multiple total maximum CALPHAD evaluations until the CSA approximation agreed well with the full factorial sampling of 505,000 samples shown in

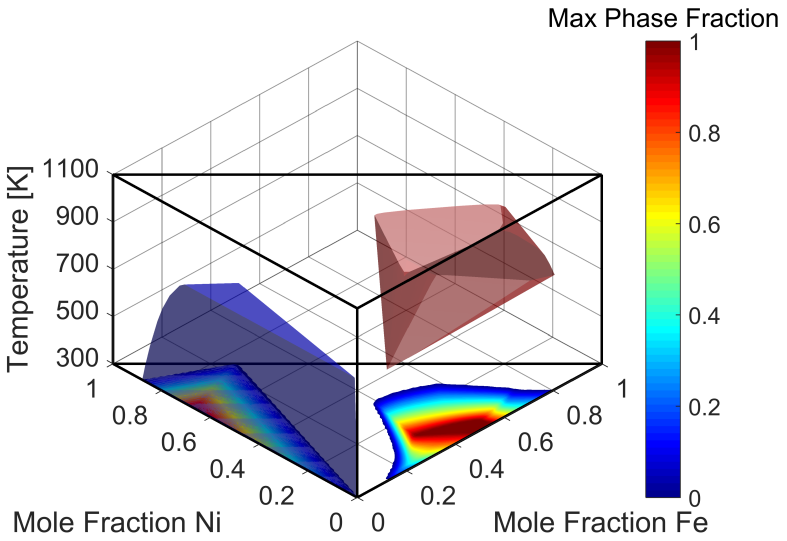

Figure 4.1: Approximate locations of $CrNi_2$ phase (blue) and sigma phase (red) are shown in three-dimensional composition-temperature space as determined from an evenly discretized (100 intervals in each dimension) grid of 505,000 samples of CALPHAD. The maximum amount of each phase along the temperature dimension is also projected below the displayed phase regions on to the same two-dimensional composition space. Reprinted with permission from Kirk et al. (2018) [4].

Fig. 4.1. Figure 4.2 displays the results of this exercise and the points used to initialize the CSA. In Fig. 4.2, it is shown that the CSA estimate of the constraint boundary approaches the “ground truth" around 1000 function evaluations. This execution of the CSA took about 10 minutes to complete on a standard quad-core, 3.40 GHz processor with 12 GB RAM.

To further validate these results, several performance metrics were calculated for each CSA constraint boundary by comparing the approximated boundaries to 505,000 samples of CALPHAD. Equation 4.2 represents the misclassification rate [119], where N_{fp}, N_{fn}, N_{tp}, and N_{tn} are the number of *false positives*, *false negatives*, *true positives*, and *true negatives* respectively. In this context, the terms *true* and *false* refer to whether a sample of the CSA agrees with the ground truth as predicted by CALPHAD (*true*) or not (*false*). The terms *positive* and *negative* indicate whether a sample lies within the CSA boundary (*positive*) or not (*negative*). Misclassification rate can therefore be interpreted as the probability of obtaining a false result from the CSA boundary.

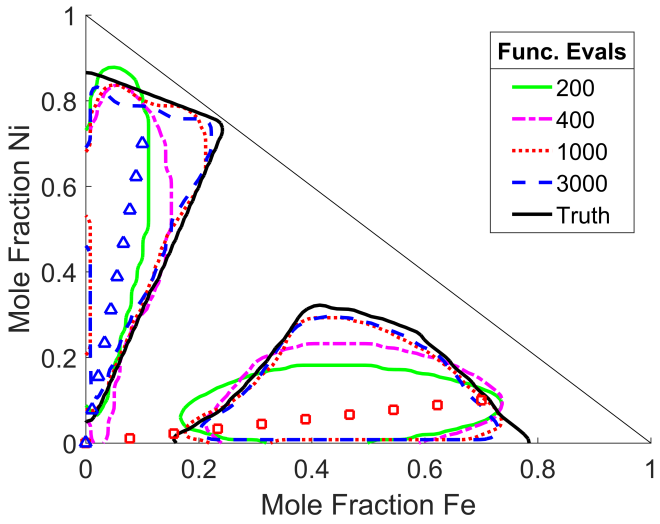

Figure 4.2: Undesirable phase boundaries determined from multiple runs of the CSA with various maximum function evaluations. The solid black line represents the boundary obtained from a 505,000 sample, full-factorial grid sampling of CALPHAD considered here as the "ground truth". The points used to initialize the CSA for the $CrNi_2$ phase at 600 K (blue triangles) and the sigma phase at 1000 K (red squares) are also shown. Reprinted with permission from Kirk et al. (2018) [4].

$$\text{Misclassification Rate} = \frac{N_{\text{fp}} + N_{\text{fn}}}{N_{\text{fp}} + N_{\text{fn}} + N_{\text{tp}} + N_{\text{tn}}} \tag{4.2}$$

Two metrics popular in the pattern recognition community, precision and recall [120], were calculated by comparing the CSA boundaries to 505,000 samples of CALPHAD. Equation 4.3 represents precision or the probability a *positive* result from the CSA boundary actually represents a sample with unallowable phase concentration. As shown in Eqn. 4.4, recall estimates the probability that a randomly selected sample with unallowable phase concentration will lie within the constraint boundary. Geometrically, precision can be thought of as the portion of the CSA boundary that is actually inside the truth region while recall can be seen as the portion of the truth region that is captured by the CSA boundary.

$$\text{Precision} = \frac{N_{\text{tp}}}{N_{\text{tp}} + N_{\text{fp}}} \tag{4.3}$$

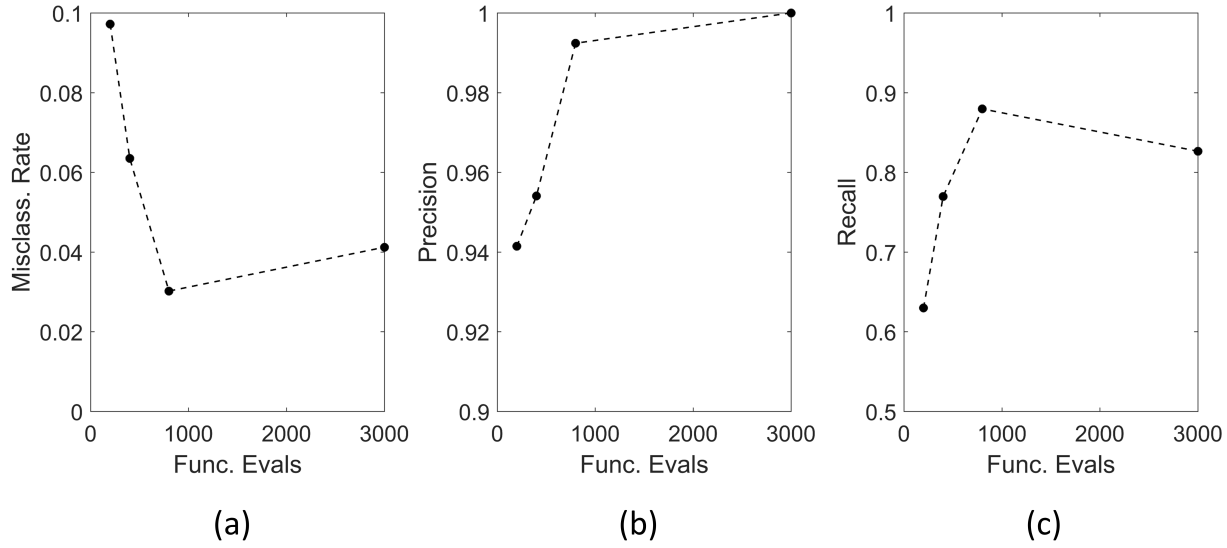

Figure 4.3: The effect of the number of function evaluations on the performance of the Constraint Satisfaction Algorithm (CSA) [5] as measured by (a) misclassification rate, (b) precision, and (c) recall. Reprinted with permission from Kirk et al. (2018) [4].

$$\text{Recall} = \frac{N_{\text{tp}}}{N_{\text{tp}} + N_{\text{fn}}} \tag{4.4}$$

Each of these metrics can be seen plotted for every run of the CSA in Fig. 4.3. In every case, misclassification rate is below 10% and precision is above 90%. However, at 1000 function evaluations misclassification rate is below 5%, precision is above 99%, and recall is above 85%. For this reason, this CSA model was chosen to be used with the path planning algorithm. Note that the phase boundary was modeled relatively accurately by the CSA with only 1000 samples. It is unlikely that the phase regions could have been modeled as accurately in three-dimensional space with so few samples by more naive approaches.

In Fig. 4.2, it can be seen that the boundary drawn by the CSA grows to a maximum around 1000 samples and then gets slightly smaller as the number of samples increases to 3000. Because the boundary gets smaller, it covers less of the true region and therefore increases the number of false negatives. This increase leads to the increase in misclassification rate and recall rate seen in

Fig. 4.3. One possible explanation is the heuristic nature of the SVDD [114] used in the CSA. Because the SVDD is meant to classify real data, it accommodates outliers with the inclusion of slack variables that are penalized by a factor (set to 1 in the current work). This could mean the SVDD boundary in the CSA shrinks because it determines some data on the boundary are outliers that should be excluded. The SVDD also has an associated kernel parameter that adjusts how tightly the boundary is fit to the data. In the present work, which uses an RBF kernel, this parameter is set to a standard 0.5. These parameters could potentially be optimized to improve the performance of the CSA.

Because the CSA draws boundaries from known samples and then grows the boundary by sampling outward, it tends to underestimate the "true" obstacle region, even if only by a few percent composition. This could be an issue if designed paths are very close to the CSA boundaries, as is the case when minimizing path length. However, as seen in Figure 4.1, the areas of the "true" region that are not captured by the CSA (typically the edges of the region that face the center of composition space) have relatively small concentrations of undesirable phases ($\leq$20%). If total avoidance of undesirable phases is an important design requirement, a small "buffer" could be created around the edges of the obstacle region by expanding it by a few percent composition. Furthermore, a more robust cost function, like maximizing obstacle clearance or distance from the obstacles, could be used to minimize the possibility of impacting phase regions that are underestimated by the CSA.

4.2.3 Cost Function: Minimize Path Length

With the phase regions and target compositions identified, paths were planned considering each of two cost functions using a MATLAB implementation of RRT*FN [3]. The first cost function is simply path length in composition space. Computationally, this cost is calculated by summing the length of each segment along a path, as seen in Eqn. 4.5. Minimizing path length is potentially desirable to both manufacturers and designers as fewer layers and less material will be needed to form the gradient region.

$$c_1(\sigma) = \sum_{k=1}^{n} l_k \tag{4.5}$$

Figure 4.4 displays a path optimized to minimize path length, as calculated in Eqn. 4.5. From visual inspection, the path seems to be a very good estimate of the shortest path between the two target compositions. By comparing the paths in Fig. 4.4 to the “true" region in Fig. 4.2 it can be observed that the portion of the path with 40 to 60% Fe likely penetrates the “true" undesirable phase region due to inaccuracies in the CSA model. However, as demonstrated in Fig. 4.1, the phase fraction of sigma in this region is relatively small. It can also be observed that the edges of the tree grown by RRT*FN are near parallel. This is because each node is connected to the parent node that minimizes the user-defined cost function. Since all edges seek to minimize the same cost function, they tend to have similar orientations.

As the RRT*FN algorithm is dependent on random sampling, the algorithm was run ten times with various random seeds to gain insight on its stochastic variability. In Fig. 4.5, each of the best paths obtained from these runs are plotted along with their respective costs. The mean cost of these paths (path length in composition space) is reported as 0.866 with a standard deviation of 0.00639 or less than 1% of the mean. From these results, it can be concluded that paths planned to minimize length are rather robust to variability in random sampling. This result is not surprising as this cost formulation meets the conditions for asymptotic optimality with RRT*FN and is common in the motion planning community.

4.2.4 Cost Function: Maximize Obstacle Clearance

The second cost function attempts to maximize the distance in composition space from the undesirable phase regions. Part composition is often difficult to control in additively manufactured parts due to evaporation, powder kinetics, and other confounding variables. Difficulty in compositional control is only compounded as the number of powders used in the process is increased. A path that maximizes the compositional distance from undesirable phases is less likely to form those phases if composition does vary and is therefore conceivably desirable to manufacturers. In the

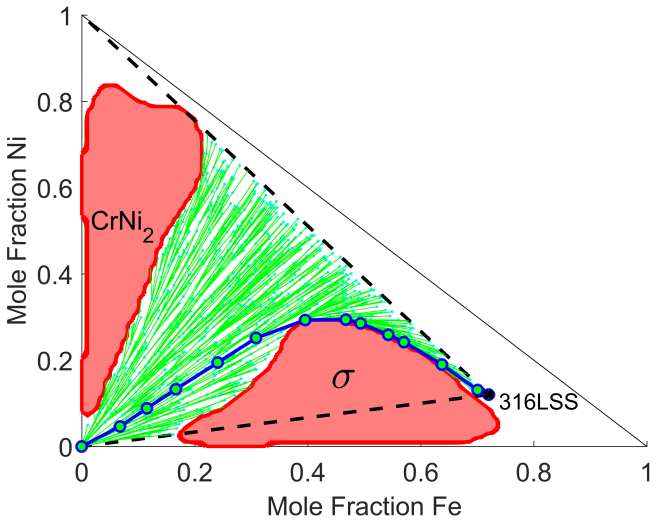

Figure 4.4: Rapidly-exploring random tree (green) created to plan a path between Pure Cr and 316L SS that minimizes path length. Optimal path shown in blue. Reprinted with permission from Kirk et al. (2018) [4].

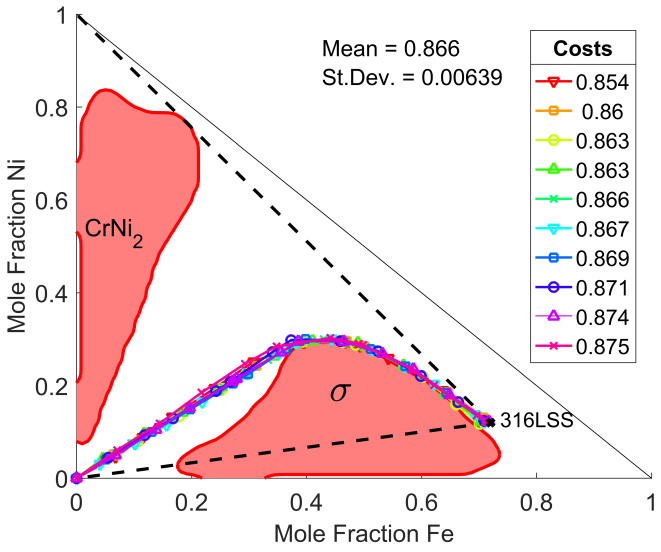

Figure 4.5: Ten runs of the path planning algorithm with various random seeds and their respective costs. All attempt to plan a path between Pure Cr and 316L SS that minimizes path length, as calculated in Eqn. 4.5. Reprinted with permission from Kirk et al. (2018) [4].

motion planning community, this goal of maximizing distance from the obstacles is often referred to as maximizing obstacle clearance [121].

The obstacle clearance cost function is calculated by first finding the average euclidean distance from the nearest obstacle boundary for each segment in a path. The reciprocals of these distances are then summed to arrive at a total cost, as seen in Eqn. 4.6. The additive form of this cost function is dictated by the employed implementation of RRT*FN. A cost function where the average clearance of the total path is used instead of the sum of segment averages might produce paths with more separation, but is not compatible with the current implementation of the path planning algorithm.

$$c_2(\sigma) = \sum_{k=1}^{n} \frac{1}{d_{\text{avg},k}} \tag{4.6}$$

A second set of paths was planned to optimize this second cost function. One such path and its corresponding tree can be seen plotted in Fig. 4.6. A similar stochastic study was conducted to determine the sensitivity of the paths to random sampling. The paths obtained from this study and their respective costs can be seen in Fig. 4.7. The mean cost of these paths, as calculated from Eq. 4.6, was 198.4 with a standard deviation of 11.2 or 5.6% of the mean. While these path achieve separation from the undesirable phase regions, the stochastic sensitivity of these paths is higher than that of the paths that minimize path lengths. This sensitivity can be partially attributed to the formulation of the cost function. As seen in Eqn. 4.6, the cost function is a summation of each segment's individual cost. Because this cost cannot be negative, it then follows that, generally speaking, path cost increases with the number of segments. The minimization of this cost function thus prioritizes paths with fewer segments. This bias towards fewer segments is desirable when minimizing path length, but inherently contradictory to the objective of maximizing distance from the obstacles as paths that maximize clearance tend to be longer than other paths. The inverse nature of the cost function also causes segments that are closer to the obstacle to dominate the cost. This can be problematic given the target compositions' close proximity to the obstacles. Even small variations in the segments nearest the obstacles can cause substantial changes in the value of

the cost function. These features of the cost function combine to increase the stochastic sensitivity and therefore decrease the optimality of paths that maximize distance from the obstacles.

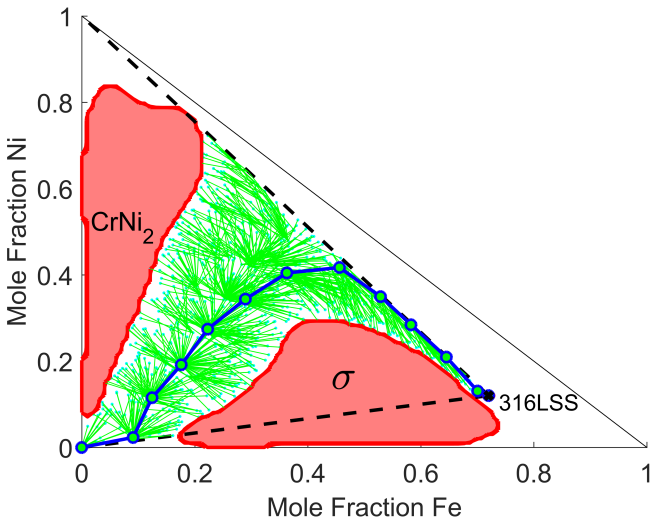

Figure 4.6: Rapidly-exploring random tree (green) created to plan a path between Pure Cr and 316L SS that maximizes distance from the undesirable phase regions. Optimal path shown in blue. Reprinted with permission from Kirk et al. (2018) [4].

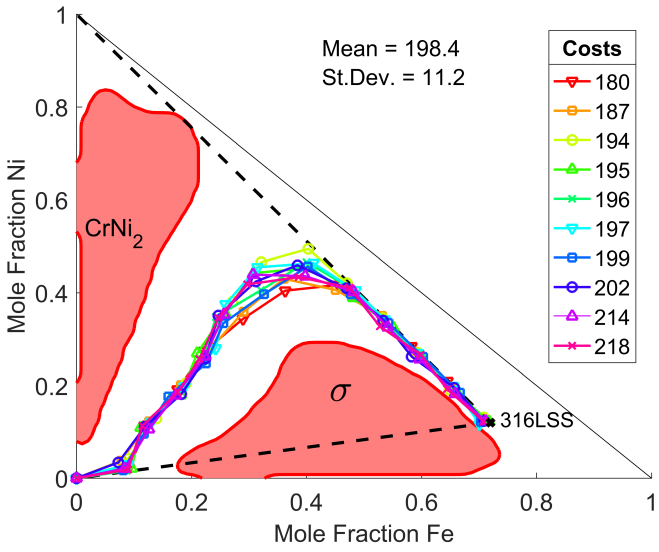

Figure 4.7: Ten runs of the path planning algorithm with various random seeds and their respective costs. All attempt to plan a path between Pure Cr and 316L SS that maximizes distance from the undesirable phase regions, as calculated in Eqn. 4.6. Reprinted with permission from Kirk et al. (2018) [4].

To combat the problematic characteristics of maximizing clearance, several parameters of the motion planning algorithm (RRT*FN) were modified from their initial values and another series of paths was planned. First the maximum distance in composition space between nodes in the path was decreased from 0.1 to 0.05. To accommodate the increased number of nodes required in the path, the number of algorithm iterations (randomly sampled nodes) was increased from 2000 to 5000. This increased the computational time from about 15 minutes to about 40 minutes on a standard quad-core, 3.40 GHz processor with 12 GB RAM. A single path planned with these new parameters can be seen in Fig. 4.8. Figure 4.9 displays the paths planned with the new parameters for ten different random seeds. The mean cost of these paths was 381.7 with a standard deviation of 7.85 or 2.1% of the mean. As desired, the paths have noticeably less variability than those planned with the old parameters, indicating a decrease in stochastic sensitivity. However, as these paths consist of about twice as many segments, the mean cost was significantly larger than the cost of the paths planned in Fig. 4.7. Visually, the paths achieve similar or better separation from undesirable

phase regions, despite the increased cost. This indicates the chosen cost function does not perfectly represent clearance from the undesirable phase regions. Formulation and implementation of a more effective cost function, like a non-additive cost that considers the maximum clearance of a path, would likely improve these results.

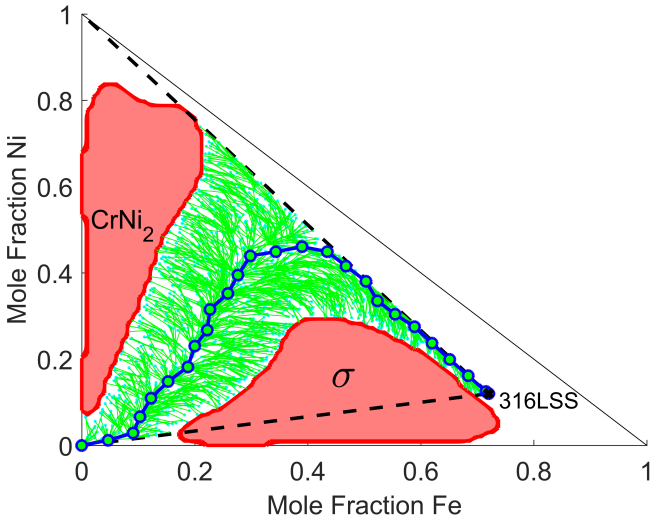

Figure 4.8: Rapidly-exploring random tree (green) created to plan a path between Pure Cr and 316L SS that maximizes distance from the undesirable phase regions. Maximum nodal separation restricted to 0.05. Optimal path shown in blue. Reprinted with permission from Kirk et al. (2018) [4].

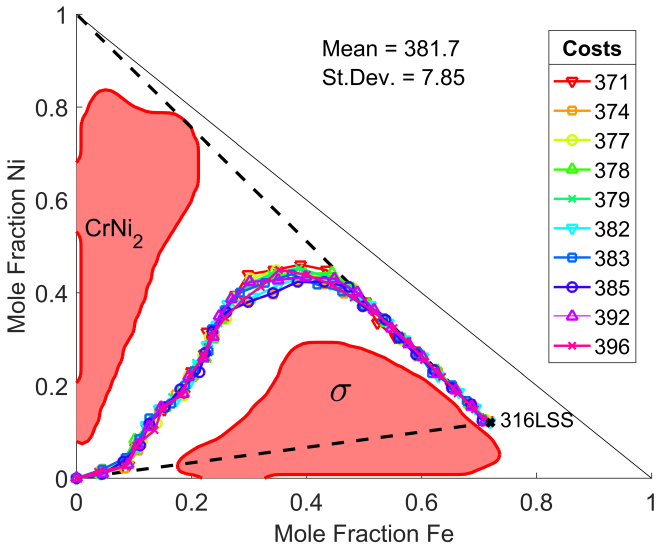

Figure 4.9: Ten runs of the path planning algorithm with various random seeds and their respective costs. All attempt to plan a path between Pure Cr and 316L SS that maximizes distance from the undesirable phase regions, as calculated in Eqn. 4.6, and were planned with a maximum nodal separation of 0.05. Reprinted with permission from Kirk et al. (2018) [4].

4.2.5 Computational Complexity

Each of the paths presented in Figs. 4.4, 4.6, and 4.8, had a different computational expense, as measured by the number of function evaluations of the constraint model. The number of constraint model evaluations was recorded as a function of RRT*FN iterations for each path, where each iteration represents the addition of a new randomly sampled node. The results of this study can be seen in Fig. 4.10. In all cases, the algorithm sampled the constraint model hundreds of thousands of times. The number of evaluations would have increased dramatically if CALPHAD was sampled directly and the temperature dimension were not collapsed. In this case, checking for collision in the segment between nodes would require a full search of not just the segment itself, but the plane formed by extending the segment in the temperature dimension. As shown in Figs. 4.2 and 4.3, the number of CALPHAD evaluations needed to form an adequate CSA boundary is only 1,000. Consequently, it can be concluded that the use of the CSA significantly reduces the number of

CALPHAD evaluations necessary to plan an optimal path.

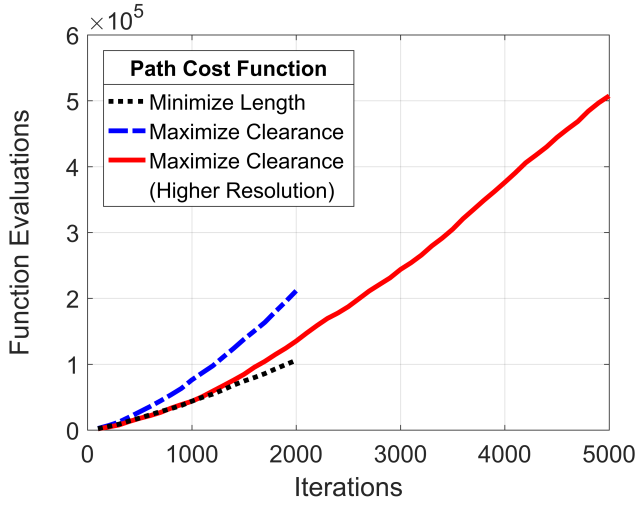

Figure 4.10: The number of constraint model evaluations performed by the path planning algorithm (RRT*FN) as a function of algorithm iterations for paths that minimize length, maximize clearance (distance from the undesirable phase regions), and maximize clearance at a higher resolution (nodal separation restricted to 0.05). Reprinted with permission from Kirk et al. (2018) [4].

4.2.6 Experimental Results [†]

To test the efficacy of the design methodology, several compositionally graded alloys were printed with an Optomec LENS® MR-7 Directed Energy Deposition (DED) system by colleagues at Texas A&M University. Each gradient was printed by carefully controlling the mixing of three powders: pure Ni powder, pure Cr powder, and a premixed 316L stainless steel powder. The linear gradient between 316L stainless steel and pure Cr was printed first as a baseline for comparison. A second gradient was planned with the presented methodology to minimize the cost function in Eqn. 4.6 (i.e. maximize obstacle clearance). This objective was chosen because accurately mixing three powders in a DED system to achieve non-linear gradients is a non-trivial task that pushes the state of the art. As such, some compositional variance is to be expected. The compositions

[†]Experiments and analysis conducted by Olga Eliseeva, Prof. Ibrahim Karaman, and colleagues

of the linear gradient, the planned gradient, and the experimental approximation of the planned gradient are shown in Fig. 4.11a. The compositions in the experimental gradient were obtained using wavelength dispersive spectroscopy (WDS).

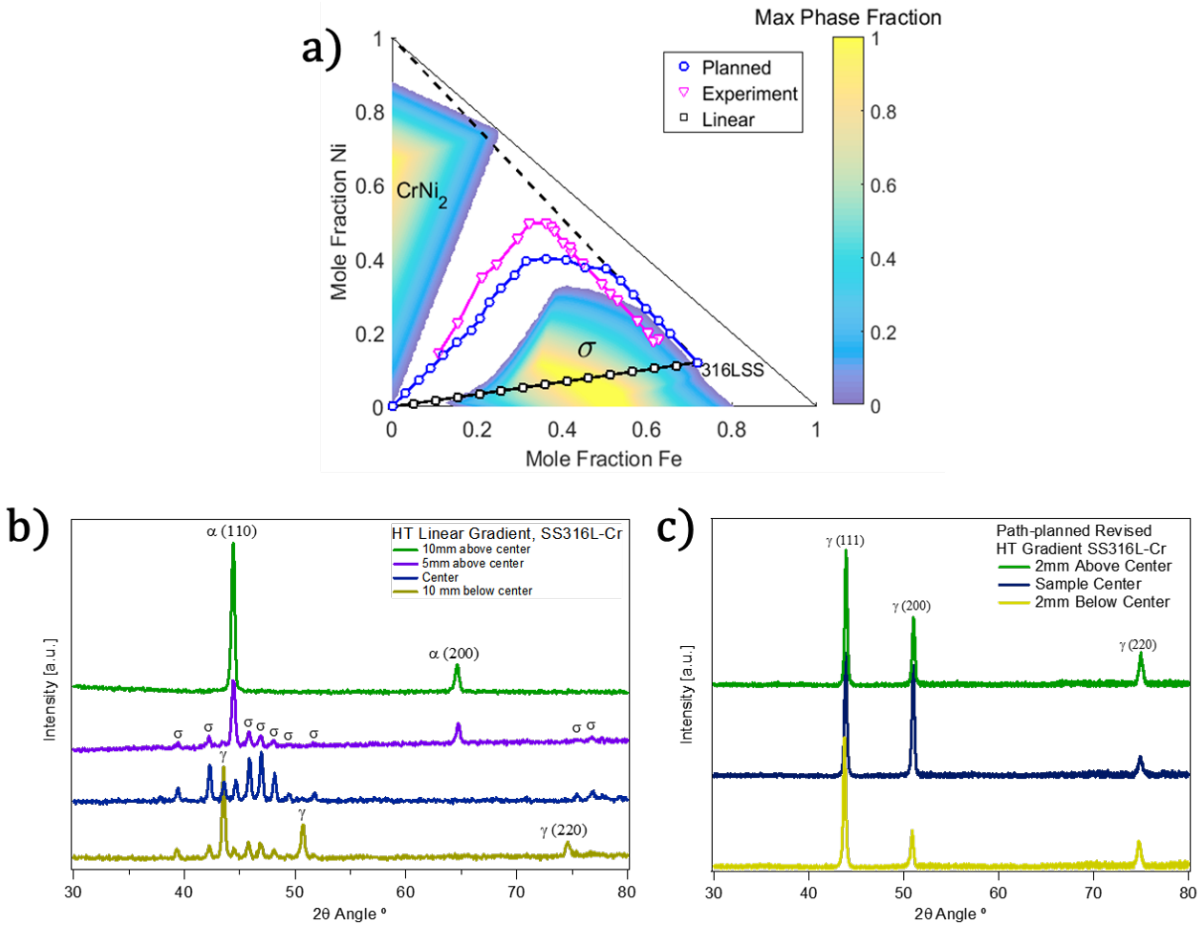

Figure 4.11: a) The compositional gradient paths of the planned gradient, its experimental approximation, and the linear gradient between 316L stainless steel and pure Cr. Maximum predicted phase fractions of deleterious phases from 300 to 1100 K are also shown in the color scale. b) XRD phase analysis of the heat treated (900 °C for 8h) linear gradient. c) XRD phase analysis of the heat treated (900 °C for 8h) experimental approximation of the planned gradient. Reprinted with permission from Eliseeva et al. (2019) [2].

During printing, the linear gradient produced a crack along the build direction that spanned nearly half of the gradient part. It was hypothesized that the presence of the brittle sigma phase in

the linear gradient, as predicted in Fig 4.11a, was unable to accommodate the thermal stresses of the additive manufacturing process. Although phase analysis via X-ray diffraction (XRD) did not detect sigma phase in the as-built part at room temperature, XRD did detect significant amounts of sigma phase after a heat treatment of 900 °C for 8 hours, as shown in Fig. 4.11b. This heat treatment was chosen by examining the kinetics of sigma phase formation in similar steels.

Although its compositions deviated slightly from the planned gradient, the experimental approximation of the planned gradient did not experience cracking at any point. XRD analysis conducted at both room temperature and after the specified heat treatment (900 °C for 8 hours) did not detect any sigma phase. The XRD results of the heat treated sample can be seen in Fig. 4.11c. These results validate the CALPHAD phase models and also demonstrate the effective use of the presented methodology to avoid deleterious phases. More details on the experimental results can be found in Eliseeva et al. [2].

4.3 Chapter Summary

One of the most common issues when designing or manufacturing compositionally graded alloys is the presence of deleterious phases. The presented methodology can design gradients that avoid these phases according to user specified constraints. Constraints on phase formation should carefully consider temperature, either by defining a range of temperatures, a single temperature, or phases formed during solidification, though the methodology can accommodate any combination of these constraints. CALPHAD modeling is the fundamental tool that predicts phase formation as a function of composition and temperature. Surrogate models are constructed from CALPHAD data to create models that are efficient enough to use in a path planning algorithm.

A case study in the Fe-Ni-Cr system is used to demonstrate the effectiveness of the methodology in avoiding deleterious phases. Paths were planned from 316L stainless steel to pure Cr while avoiding the $CrNi_2$ phase and the sigma phase. Two cost functions were used to optimize gradient paths: one to minimize path length and another to maximize obstacle clearance. If obstacles lie in the linear path between the initial and goal composition, paths that minimize path length necessarily lie next to obstacle boundaries. If obstacle clearance is used as a cost function, optimal paths lie

away from obstacle boundaries and are more robust to compositional variance or obstacle uncertainties. The stochastic variance and computational complexity (in terms of function evaluations) of both cost functions were quantified. Experimental evidence validates that the linear gradient produces sigma phase after heat treatment while the planned gradient does not.

5. CONSTRAINTS FOR MANUFACTURING

Aside from deleterious phases, the largest challenge facing compositionally graded alloys is satisfying the stringent criteria needed to successfully print them with an additive manufacturing process. It is therefore paramount that a design methodology for such alloys consider an alloy's manufacturability, or printability as it is called in the additive manufacturing community. This chapter exhibits how common manufacturing metrics can be implemented into the design methodology. First, some metrics for alloy printability are given, along with various methods of calculating them. A case study then demonstrates the use of these metrics in the constraint formulation of a gradient design problem from steel to pure tungsten. The high melting temperature of tungsten provides a unique challenge for manufacturing that requires the consideration of printability metrics.

5.1 Manufacturing Metrics

There are numerous defects that have been observed to occur in metal additive manufacturing process. These include gas entrapment, keyholing, balling, lack-of-fusion, and hot tearing [70]. Many of these defects can be mitigated through proper selection of processing parameters like laser power, scan speed, or layer thickness. Several researchers have proposed optimizing these parameters using thermal models that accurately predict the evolution of the melt pool [72, 122]. However, these models are typically solved via finite element methods and using them to predict the processability of an entire composition space could be prohibitively expensive.

Although processing parameters can sometimes be optimized to find feasible printing conditions for a given composition, many compositions have inherent properties that make them much more difficult to print successfully. Predicting these properties is much more computationally efficient than seeking feasible process conditions with a thermal model. These properties can be used as *manufacturing metrics* that can predict the printability of a composition. Constraints on these metrics can then be used to ensure that the optimized gradient paths do not include compositions

that are fundamentally difficult to print. The rest of this section details some of these metrics and their relevance to alloy printability.

5.1.1 Equilibrium Solidification

The solidification characteristics of an alloy are known to be some of the most critical in determining its printability. In particular, large solidification ranges can lead to a phenomenon familiar to the casting community known as hot tearing or hot cracking [73, 74, 75]. Hot tearing is experienced by a solidifying metal when sufficient time is spent at the end of solidification, allowing the liquid slurry to penetrate the mushy zone between solidified dendrites. These regions then experience large thermal strains as the material solidifies, which initiates cracks. When solidification range is large, the solidification process takes more time and there is more opportunity for hot tearing.

The solidification range of an alloy can be easily predicted from its phase diagram. When cooling from a liquid phase, the temperature at which a solid phase first appears is known as the *liquidus temperature*. As the temperature is decreased and the material solidifies, the temperature at which no liquid phase appear and only solid phases remain is known as the *solidus temperature*. The difference between these temperatures is the *solidification range* or the temperature range at which solidification takes place.

The CALPHAD method can be used in a straightforward manner to predict solidification range. In a naive way, the solidus and liquidus temperatures of a given composition can be approximated by calculating the equilibrium phase fractions at many temperatures in a wide range and looking for the temperatures where the solid phases and liquid phases are initiated. These predictions can be refined by instituting a root finding method, like bisection. However, modern CALPHAD tools allow accurate and efficient prediction of the solidus and liquidus temperatures [110]. In these tools, phase free energy functions can be optimized to find the precise conditions where the liquid phase enters or leaves equilibrium. In this way, equilibrium solidification ranges can be computed relatively efficiently for any composition.

5.1.2 Scheil Solidification

While equilibrium solidification simulations are relatively efficient, the rapid cooling of the additive manufacturing process does not always satisfy equilibrium conditions. As such, equilibrium simulations can have some inaccuracies when predicting phase formation in additively manufactured materials. Scheil-Gulliver or Scheil simulations have been shown to be more accurate for non-equilibrium, rapid cooling processes like welding and additive manufacturing [85, 84, 86]. In these simulations, the liquid-solid interface is assumed to be in equilibrium, however the compositional diffusion of the liquid phase is assumed to be infinite, while the diffusion in solid phases is assumed to be zero. Practically, this means that the composition of the liquid phase changes during solidification as solidified phases deplete certain elements. This can mean that phase fractions can differ from equilibrium simulations and entirely new phases can appear that are not predicted from equilibrium. Due to the assumptions of a Scheil simulation, the solidification ranges predicted by Scheil will always be larger than those predicted by equilibrium. This means that Scheil simulations can be considered more conservative than equilibrium for this metric.

Recently, both Bocklund et al. [86] and Moustafa et al. [84] applied Scheil simulations to investigate compositionally graded alloys. They both show differences when compared to equilibrium, including some phases that appear in Scheil simulations, but are absent in the equilibrium simulations. In Bocklund et al., Scheil simulations performed on a compositionally graded alloy between Ti-6Al-4V and Invar-36 were also shown to be more accurate when compared to experiments [86].

Scheil simulations have been integrated into many CALPHAD modeling tools, including Thermo-Calc [110]. While they tend to be more accurate than equilibrium solidification for additive manufacturing, they also can take two to three orders of magnitude longer to compute for complex compositions. This reduced efficiency means Scheil simulations are less suitable for predicting over large, complex composition spaces. Nevertheless, a more sparse sampling of Scheil simulations is still practical for problems of a limited size.

5.1.3 Hot Cracking Susceptibility Criteria

As mentioned previously, hot tearing or hot cracking is a significant issue when printing new compositions. Several metrics to predict hot tearing have been developed in casting and additive manufacturing literature [123, 74]. One of the most common is the Clyne and Davies criterion [124], developed in the 1970s for casted metals. As shown in Eqn. 5.1, this Hot Cracking Susceptibility (HCS) criterion is the ratio of vulnerable time, t_v, to time when stress relaxation occurs, t_r. Both times are defined by the fraction of solid, f_s, (e.g. $t_{99} = 99\%$ solidified) and can be estimated from solidification simulations. The larger the value of HCS, the more susceptible a given alloy is to hot cracking.

$$\text{HCS}_{\text{Clyne}} = \frac{t_v}{t_r} = \frac{t_{99} - t_{90}}{t_{90} - t_{40}} \tag{5.1}$$

Easton et al. [73] developed another hot cracking susceptibility criterion, or hot tearing indicator, that expands upon the Clyne criterion by introducing coherency and coalescence temperatures, T_0 and T_{co} respectively. The coherency temperature represents the point at which the solid phase forms dendrites and pulls from the interdendritic liquid phase ($f_s \approx 0.9$). While the coalescence temperature represents the point at which the material can be considered solidified and act as a solid ($f_s \approx 0.98$). The exact determination of these temperatures often requires experiments [73]. Equation 5.2 represents Easton et al.'s Hot Cracking Susceptibility (HCS) criterion, where $f_s(T)$ represent the fraction solidified as a function of temperature, which can be easily computed from a CALPHAD solidification simulation. Its form magnifies the effect of the last portion of solidification, when f_s is high, as compared to the Clyne criterion in Eqn. 5.1 [73].

$$\text{HCS}_{\text{Easton}} = \int_{T_0}^{T_{\text{co}}} f_s(T) dT \tag{5.2}$$

Lastly, Kou [125] developed yet another hot cracking susceptibility criterion that depends on the solidification behavior of the alloy. Shown in Eqn. 5.3, this criterion is defined as the maximum absolute value of the slope of the T *vs* $\sqrt{f_s}$ curve up to the coalescence point, $f_{s,\text{co}}$.

$$\text{HCS}_{\text{Kou}} = \max\left|\frac{dT}{d\sqrt{f_s}}\right| \forall\, f_s \leq f_{s,\text{co}} \tag{5.3}$$

Benoit et al. [75] compared the criteria shown in Eqns. 5.2 and 5.3 in the susceptibility of aluminum alloys to hot cracking during additive manufacturing. They found good agreement with experimental results, though they also warned that accurate determination of the coherence and coalescence points might require experimentation.

All three of the aforementioned hot cracking susceptibility criteria depend heavily on predicting the fraction of solidified phases as a function of temperature. Consequently, they can be reasonably predicted with CALPHAD techniques. Both equilibrium and Scheil solidification simulations can be used to generate the required curves, but Scheil simulations are more likely to be accurate given rapid solidification conditions.

5.2 Case Study: Steel to Tungsten *

5.2.1 Problem Description

5.2.1.1 Motivation

The following case study presents the use of manufacturing metrics in the constraint formulation of a gradient design problem. Specifically, metrics are used to design a gradient from steel to tungsten, which presents significant manufacturing challenges due to a drastic difference in melting temperatures. This case study was the result of a collaborative effort with QuesTek Innovations LLC. Funded by the U.S. Department of Energy, the project goal was to design a compositional gradient for plasma facing components in nuclear fusion devices. Such components require materials with high melting temperatures, such as tungsten, to withstand the extreme temperatures of the fusion process. However, the preferred heat sinks for these components are made from materials with much lower melting points, like steel. If these components are joined discretely, as with bolts or welds, then large gradients in coefficient of thermal expansion as well as melting temperatures

*Material is based upon work done in collaboration with QuesTek Innovations LLC and funded by the U.S. Department of Energy under Award #DE-SC0020032

will create significant stresses and cracking. A compositional gradient has the potential benefit of smoothing these properties and mitigating the associated issues.

5.2.1.2 Problem Definition

The initial and goal compositions of the designed gradient were determined to be Fe9Cr and pure tungsten. Unfortunately, the linear compositional gradient between Fe9Cr and pure W, shown in Fig. 5.1a, is rife with undesirable, deleterious phases. Figure 5.1b shows equilibrium phase fractions along the path at various temperatures as predicted by Thermo-Calc's TCHEA2 database. From these plots, it is evident that the linear gradient experiences several regions of 100% phase fraction of both laves and mu phases. These phases are known to be brittle and can lead to cracking during the build and severely compromised parts.

To avoid these phases, it is necessary to consider additional elements in the search for a feasible gradient path. Preliminary exploration by QuesTek determined that adding small amounts of aluminum can destabilize the sigma phase that tends to form at compositions rich in iron and chromium. Similarly, vanadium was determined to destabilize the laves and mu phases, but stabilize sigma phase. Due to vanadium's expense in comparison to the other elements in this system, it was decided to only consider the Fe-Cr-W-Al system.

5.2.2 Design Space Exploration

Once the design space was chosen, samples of relevant thermodynamic information were gathered from Thermo-Calc's TCHEA2 database.

5.2.2.1 Phase Exploration

More than 275,000 uniform random samples were taken from the Fe-Cr-W-Al composition space and a uniform temperature distribution from 300 to 3700 K (the melting point of pure W is 3695 K). Phase equilibria were predicted at these samples to determine where deleterious phase regions are located. Figure 5.2 displays marginal distributions of each dimension in thermodynamic space (i.e. each composition and temperature normalized between 300 and 3700 K (T_{norm})) subject to different phase criteria.

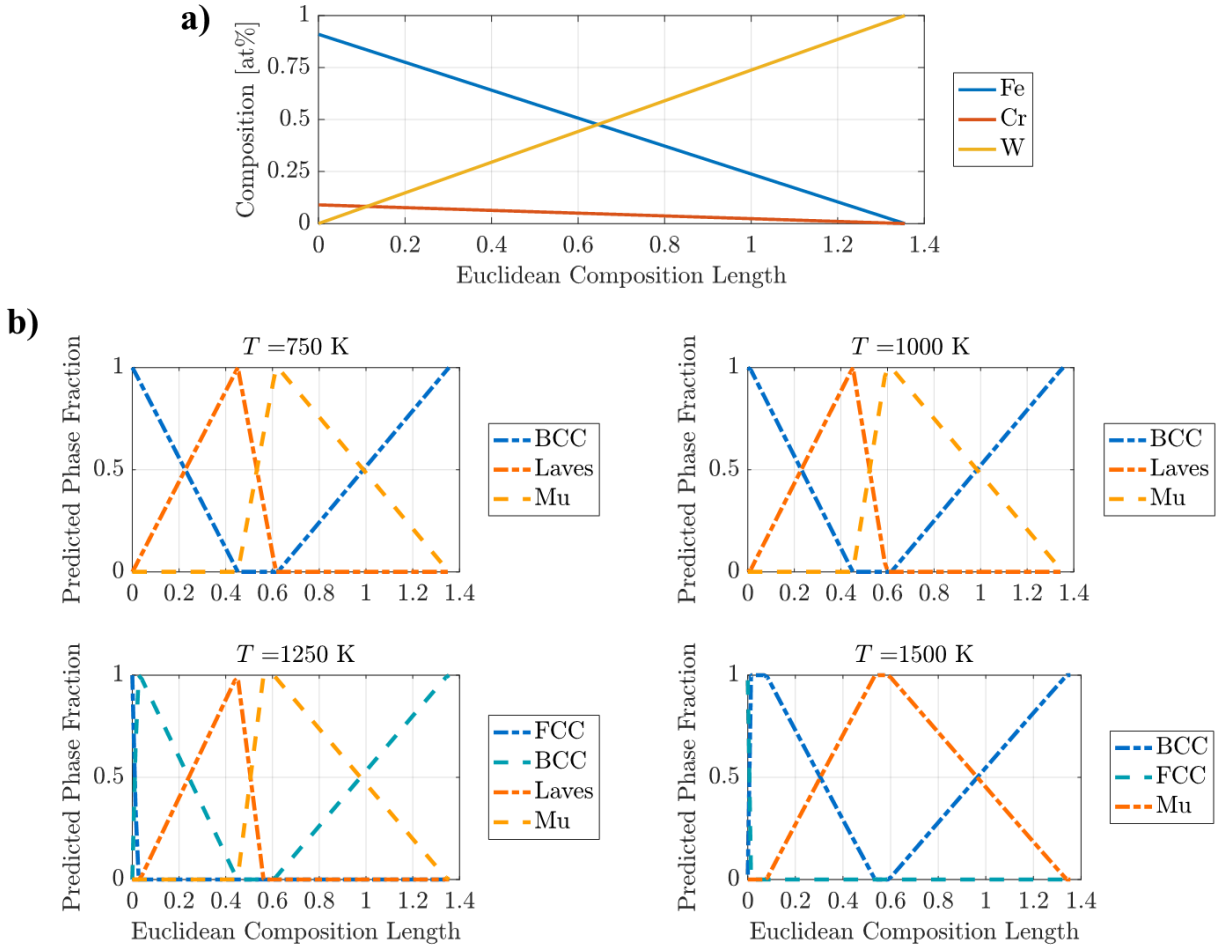

Figure 5.1: a) Compositions of the linear gradient path between Fe9Cr and pure W. The x-axis represents the length in composition space along the path from Fe9Cr to pure W. b) Equilibrium phase fractions along the linear gradient path at various temperatures.

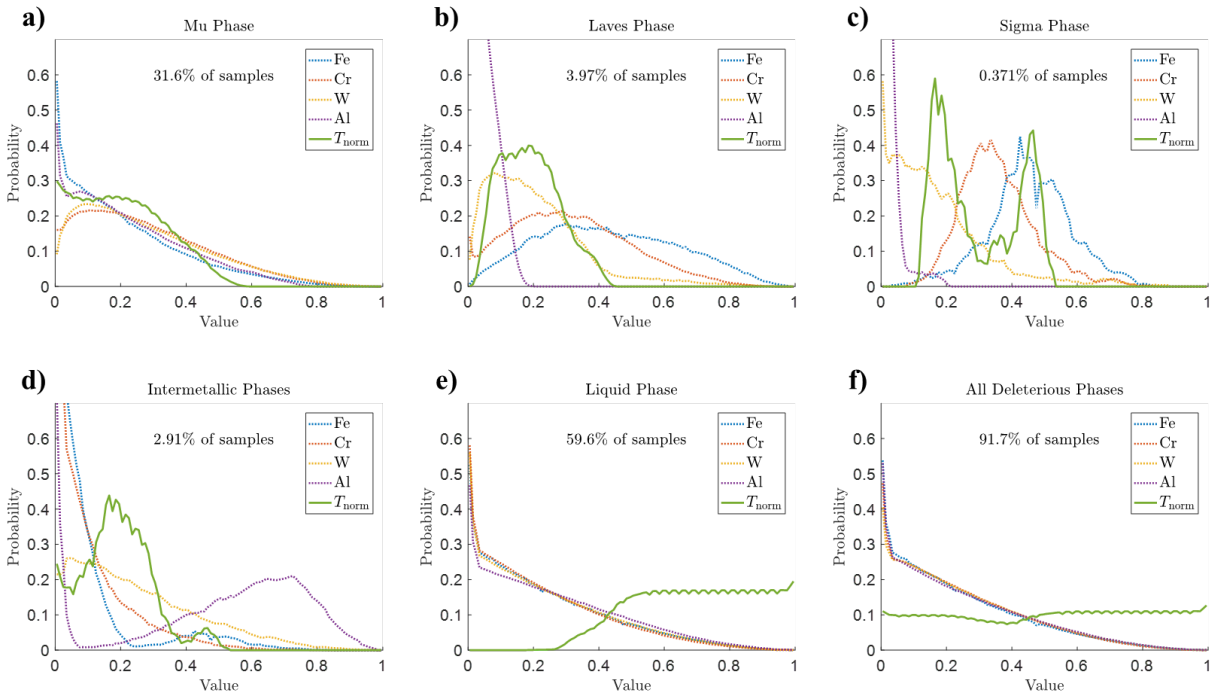

Figure 5.2: Distributions of samples in Fe-Cr-W-Al-Temperature space that contained greater than 0.01 mole fraction of a) mu phase, b) laves phase, c) sigma phase, d) intermetallic phases, e) liquid phase, and f) any deleterious phase. Temperatures are normalized between 300 and 3700 K.

For example, Fig. 5.2a displays the marginal distributions of all samples that contain greater than 0.01 mole fraction of mu phase, which were 31.6% of all samples. The marginal distributions of composition in Fig. 5.2a are all relatively wide, indicating mu phase is present at a large range of compositions. However, the distributions for Cr and W show much fewer compositions near zero, indicating that mu phase is not present when there are negligible concentrations of Cr and W.

Figure 5.2b shows the marginal distributions where laves phase is present, a much smaller proportion of the total samples (only 3.97%). These distributions indicate that laves phase is present in samples with significant amounts of Fe and Cr, but small amounts of Al. Similarly, Fig. 5.2c visualizes the samples where sigma phase is present, an even smaller subset (0.371%). These distributions show sigma phase behaves very similarly to laves and is only present when Fe and Cr are in significant amounts and Al is almost negligible. These plots support the idea that Al can destabilize the formation of sigma and laves phases in a potential gradient.

Figure 5.2d illustrates the marginal distributions of samples where intermetallic phases (e.g. Al4W) are present (2.91% of samples). The distribution of Al in the samples shows that intermetallic phases are present in samples with high fractions of Al. As such, the addition of Al to the gradient must be carefully managed so that enough Al is added to avoid sigma and laves phases, but not so much that intermetallics begin to appear.

While Fig. 5.2 can give an idea of where deleterious phases are located in composition-temperature space, a clearer picture of which compositions produce deleterious phases can be obtained by visualizing which compositions produce a certain phase at any temperature. By collapsing the temperature dimension in this way, phase regions can be visualized in three-dimensions as in Fig. 5.3. The regions plotted in Fig. 5.3 were found by training k-nearest neighbors classifiers (k=3) on the points sampled from composition-temperature space and then testing those classifiers on a full sampling of composition space at a dense range of temperatures from 300 to 3700 K.

Figure 5.3a depicts the region in Fe-Cr-W-Al space where mu phase is present (in greater than 0.01 mole fraction) at some temperature between 300 and 3700 K. Mu phase is present in 96.% of the tested compositions, even those that are very close to the gradient endpoints (Fe9Cr and

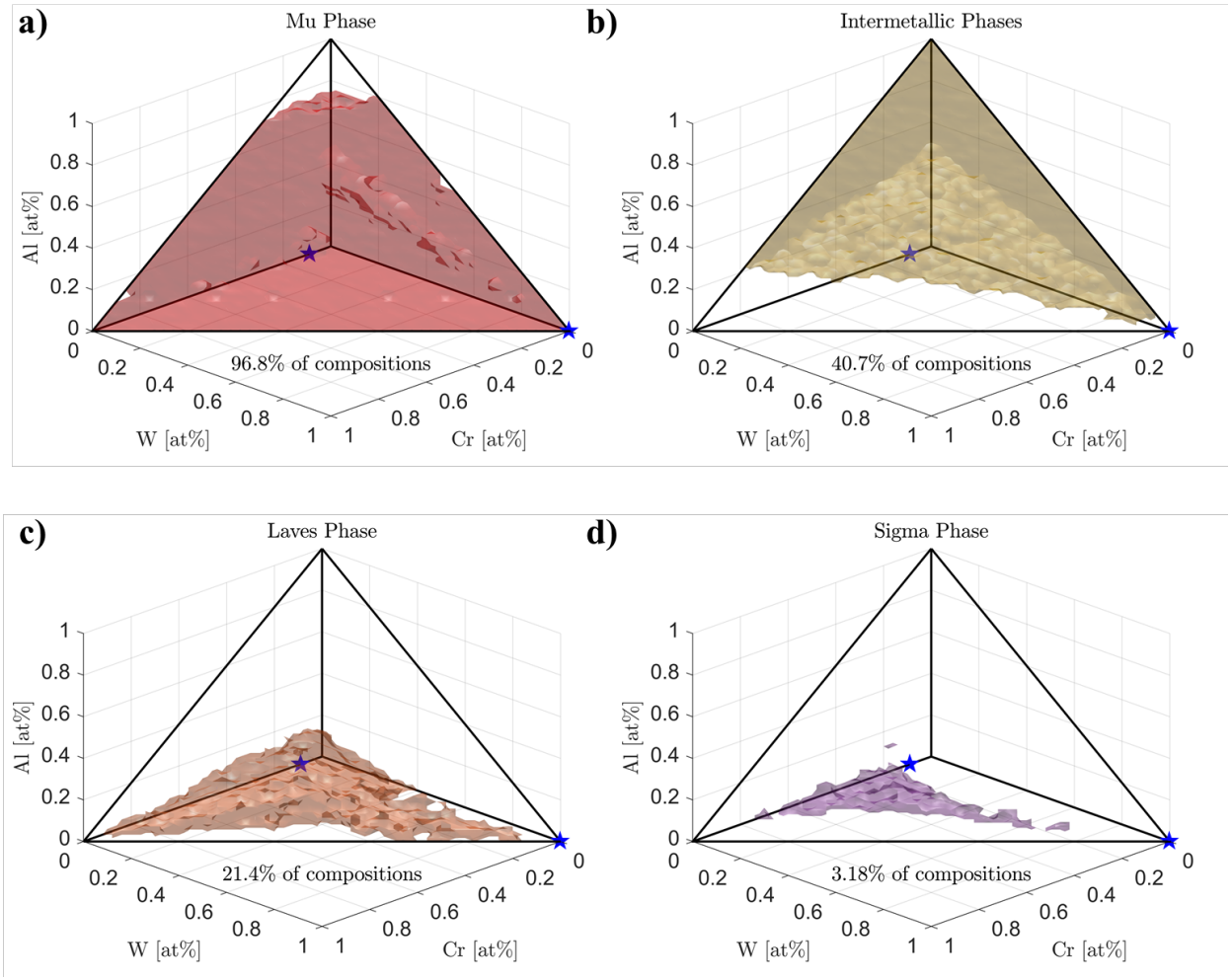

Figure 5.3: Locations in Fe-Cr-W-Al space where greater than 0.01 mole fraction of a) mu phase, b) intermetallic phases, c) laves phase, and d) sigma phase is present at any temperature between 300 and 3700 K. The endpoints of the gradient (Fe9Cr and pure W) are marked with stars.

pure W). This is an issue if the gradient will experience the relevant temperatures long enough to approach equilibrium and produce mu phase. As seen in Fig. 5.3a, there are very few possible gradient paths from Fe9Cr to pure W that could avoid mu phase at all possible temperatures.

Figure 5.3b illustrates the region occupied by intermetallic phases (40.7% of compositions). This region dominates the Al-rich portion of the composition space. Also, less Al is needed to form intermetallics as compositions approach pure W.

Figures 5.3c and 5.3d visualize the laves phase (21.4% of compositions) and sigma phase (3.18% of compositions) regions respectively. Both phases are common near the Fe-Cr-W ternary region, but dissipate as the Al content increases. The laves phase is present at compositions very close to Fe9Cr, meaning it will be difficult to avoid the laves phase completely at all temperatures in compositions near Fe9Cr.

5.2.2.2 Solidification Range Exploration

As discussed in Section 5.1, the solidification range of an alloy is a predictor of its suitability to additive manufacturing. In general, smaller solidification ranges reduce the potential for cracking during solidification. In this system, solidification range is of particular interest because of large differences in the melting temperatures of the relevant elements. Pure W has a melting point of 3695 K while Fe, Cr, and Al have melting points of 1808 K, 2130 K, and 933 K respectively. These differences can lead to large solidification ranges as W will solidify well before elements with lower melting temperatures.

To estimate the solidification ranges of compositions in the Fe-Cr-W-Al system, Thermo-Calc was used to perform equilibrium solidification calculations for over 60,000 uniform random compositions. Ten thousand of these compositions were used to train a Gaussian process regression model that predicts solidification range when given composition. This model was tested on the remaining data and was found to have a coefficient of determination (R^2) of 0.996 and a Root Mean Square Error (RMSE) of 32.6 K on the test set.

Figure 5.4 visualizes solidification range throughout the Fe-Cr-W-Al composition space. This visualization was created by using the Gaussian process model to predict solidification range for

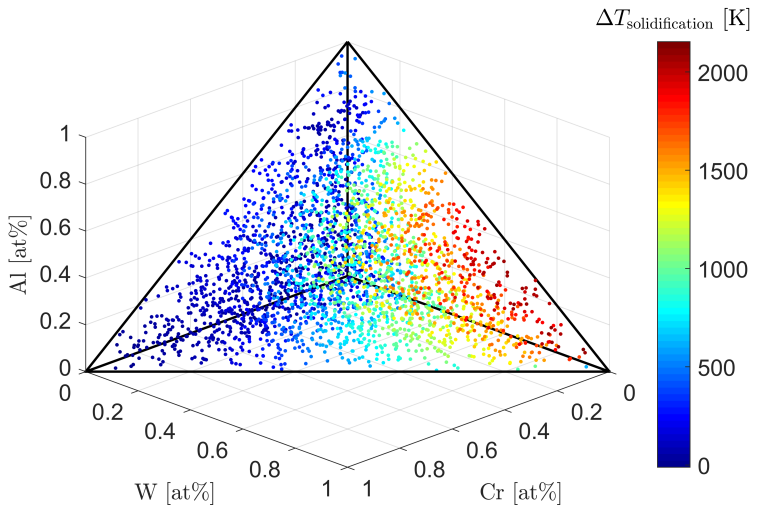

Figure 5.4: Estimated solidification ranges at various compositions in Fe-Cr-W-Al space.

3,000 uniform random compositions. Figure 5.4 demonstrates that solidification range increases as compositions approach pure W and the difference between pure element melting points increases. The highest region of solidification range occurs near the Al-W binary edge where the difference in pure element melting points is highest. Ultimately, a significant portion of the compositions in Fe-Cr-W-Al space have predicted solidification ranges above that of most successfully printed alloys (10-200 K). As such, large solidification ranges are practically unavoidable in this system, but designed gradients should minimize solidification range as much as possible.

5.2.2.3 Hot Cracking Susceptibility Exploration

In an effort to predict hot cracking more accurately than simply predicting solidification range, QuesTek has developed a Hot Cracking Susceptibility (HCS) criterion. Like the cracking susceptibility metrics discussed in Section 5.1.3, QuesTek's HCS considers the fraction of solidification time spent on the final stages of solidification as well as other material properties that can influence crack initiation.

A surrogate model for Hot Cracking Susceptibility was created by first performing Scheil solidification simulations in Thermo-Calc. As discussed previously, Scheil simulations more accurately

model rapid cooling rates of an additive manufacturing process. However, Scheil simulations also take about two to three orders of magnitude more time to perform than simple equilibrium calculations. For this reason, only 1082 simulations were run for randomly selected compositions in the Fe-Cr-W-Al system. HCS was calculated from these simulations using QuesTek's proprietary criterion. A Gaussian random process regressor was trained on a randomly selected subset of 1000 compositions. The model had a coefficient of determination (R^2) of 0.803 when tested on a test set formed from the remaining 82 compositions.

While the details of QuesTek's HCS criterion are proprietary, its approximate value throughout the composition space can be seen qualititatively in Fig. 5.5. In a similar fashion to Fig. 5.4, Fig. 5.5 was created by inputting 3,000 random compositions into the Gaussian process model to visualize HCS in the Fe-Cr-W-Al system. While the trends in HCS are less obvious than those in solidification range, there are still definitive regions where HCS is highest. These regions are primarily centered around two locations. One region is where Cr and W are present in near equal proportions and other elements are present only in minor fractions. Similarly, another region of high HCS occurs where Fe and W are present in near equal proportions, but other elements are minimal. These regions are likely where a small fraction of an Al-containing phase is present which requires lower temperatures and therefore more time to solidify. Overall, there are many compositions with suitably low HCS, but the high HCS regions leave limited paths to approach pure W from Fe-rich compositions.

5.2.3 Optimization Problem

The objective of the path planning problem formulation was to find the shortest length path that satisfied the constraints. Shorter gradient paths are desirable because shorter gradients can lead to less material use and smaller parts. The length of each linear segment in the path, l_k, was calculated as the Euclidean distance between the compositions at each end of the segment. All n segment lengths were then summed to compute a total path length which was used as the cost function, $c(\sigma)$, considered by the path planning algorithm.

Multiple constraints were considered in the optimization problem formulation. First, a model of

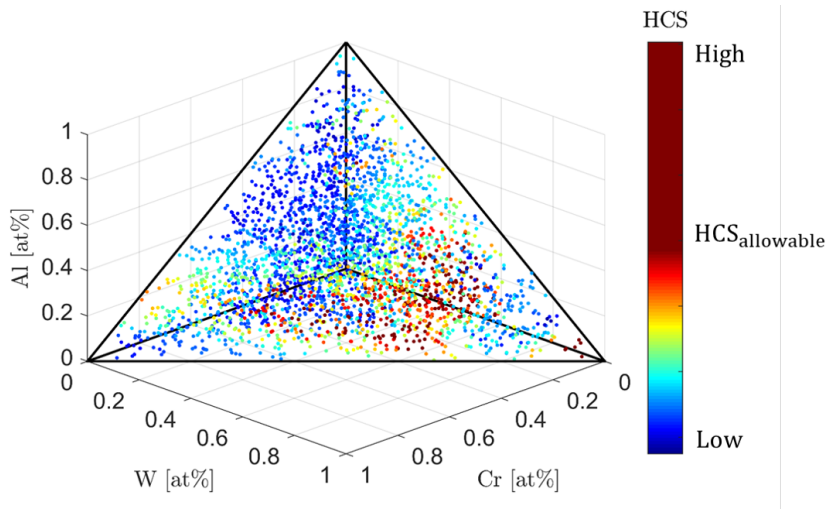

Figure 5.5: Estimated Hot Cracking Susceptibility (HCS) criterion at various compositions in Fe-Cr-W-Al space. $HCS_{allowable}$ represents the maximum allowable value of HCS. Precise values of HCS have been removed to protect QuesTek's proprietary information.

phases near each composition's solidus temperature, $T_{solidus}$, was created from the more than 60,000 Thermo-Calc solidification calculations used to create the solidification range model. The first constraint uses this model to ensure that the path does not form any significant deleterious phase fraction (f<0.01) near its solidus temperature or, in other words, just after solidifying during the manufacturing process. Collapsed temperature models were constructed from the initial sampling of over 275,000 composition-temperature combinations. These models were used to ensure the path avoided deleterious phases at all temperatures from 300 to 3700 K. Constraints on the sigma and intermetallic phases were set to be less 0.01 phase fraction as these phases are easily avoidable. The constraint on laves phase was set to be less than 0.10 to accommodate the close proximity of laves phase to Fe9Cr. Lastly, the constraint on mu phase was set to be less than 0.50. This constraint on mu phase is necessarily relaxed in comparison to the other phases due to the pervasiveness of mu phase in the composition space. A more restrictive constraint would eliminate all but the boundaries of the composition space and create an insurmountable obstacle for the path planning algorithm in its current state.

In addition to phase constraints, constraints were also placed on solidification range, $\Delta T_{solidification}$,

and Hot Cracking Susceptibility (HCS) in order to promote manufacturabilty of the gradient. Due to the large melting point differences in the design space, feasible paths were constrained to experience solidification ranges of less than 900 K, as lower constraints are unlikely to be met in the W-rich portions of the space. The maximum allowable HCS was chosen in a similar fashion. The gradient design problem formulation is summarized below.

$$z = \left\{ x_{\text{Cr}}, x_{\text{W}}, x_{\text{Al}} : x_{\text{Fe}} = 1 - \sum_{i=1}^{3} x_i \text{ and } x_i \geq 0 \; \forall \, i \right\} \tag{5.4}$$

$$\begin{aligned}
\textbf{Find} \quad & \sigma_{\text{best}} = \underset{\sigma}{\textbf{arg min}} \left[c(\sigma) = \sum_{k=1}^{n} l_k \right] \\
\textbf{subject to} \quad & \sigma(\alpha) \in Z_{\text{free}} \; \forall \, \alpha \in [0,1], \\
& Z_{\text{free}} = \Big\{ z : f_{\text{mu}}(z,T), f_{\text{sigma}}(z,T), f_{\text{laves}}(z,T), f_{\text{i.m.}}(z,T) < 0.01 \; \forall \, T \approx T_{\text{solidus}}(z), \\
& \qquad f_{\text{sigma}}(z,T), f_{\text{i.m.}}(z,T) < 0.01 \; \forall \, T \in [300\text{K}, 3700\text{K}], \\
& \qquad f_{\text{laves}}(z,T) < 0.10 \; \forall \, T \in [300\text{K}, 3700\text{K}], \\
& \qquad f_{\text{mu}}(z,T) < 0.50 \; \forall \, T \in [300\text{K}, 3700\text{K}], \\
& \qquad \Delta T_{\text{solidification}}(z) < 900\text{K}, \\
& \qquad \text{HCS}(z) < \text{HCS}_{\text{allowable}} \Big\}, \\
& \sigma(0) = z_{\text{init}} = \left\{ x_{\text{Cr}} = 0.09, x_{\text{W}} = 0, x_{\text{Al}} = 0 \right\}, \\
& \sigma(1) = z_{\text{goal}} = \left\{ x_{\text{Cr}} = 0, x_{\text{W}} = 1, x_{\text{Al}} = 0 \right\}.
\end{aligned}$$

5.2.4 Optimal Gradient Path

5.2.4.1 Algorithm Results

The constraint model given to the path planning algorithm was a single k-nearest neighbors ($k = 3$) classifier trained on 10,000 random compositions. Each composition was labeled as satisfying or failing the constraints listed in the problem formulation. The constraints were evaluated

for each composition by the respective surrogate models for each constraint: k-nearest neighbor classifiers for phase fractions and Gaussian process regressors for solidification range and HCS.

After 500,000 iterations of the path planning algorithm, the optimal path was determined to have the compositions shown in Fig. 5.6a. The optimal path exploits Al in Fe-rich portion of the path to avoid sigma and laves and then transitions to significant amounts of Cr to satisfy constraints on solidification and mu phase. Figure 5.6b displays both the solidification range and predicted HCS along the optimal path. The solidification range is predicted directly from Thermo-Calc, but the HCS is predicted from a Gaussian process regressor. The maximum solidification range is shown to satisfy the constraint of less than 900 K, however the HCS constraint is shown to be met by most of the path, but eventually violated as the HCS exceeds $HCS_{allowable}$ near pure W. This violation was not missed by the path planning algorithm, because the planned path stopped short of pure W, at around 70 at.% W. Usually, the end of the planned path can be simply connected to the goal composition, but that connection happened to violate a constraint in this case. Nevertheless, Fig. 5.5f displays a cluster of high HCS compositions near pure W indicating that high HCS cannot be avoided in this region. As such, the optimal path was deemed to remain the best feasible path. The phase fractions along the path at temperatures 100 K below the solidus temperature predicted by the machine learning model are shown in Fig. 5.6c. These phase fractions were computed directly from Thermo-Calc, but the solidus temperature was approximated from a Gaussian process regressor. This plot confirms that the first constraint on significant deleterious phase fractions near the solidus temperature was not violated by the algorithm.

Figure 5.7 shows equilibrium phase fractions along the optimal path at various temperatures. While deleterious phases are present at some of these temperatures, none of them violate the constraints set in the problem formulation. For example, at a temperature of 750 K, the optimal path experiences a maximum laves phase fraction of about 0.10 and a maximum mu phase fraction of 0.50. These values are the same values set as the maximum allowable phase fractions of their respective phases. Because the objective of the design problem was to minimize path length, the optimal path will necessarily be the path closest to the constraint boundaries without violating the

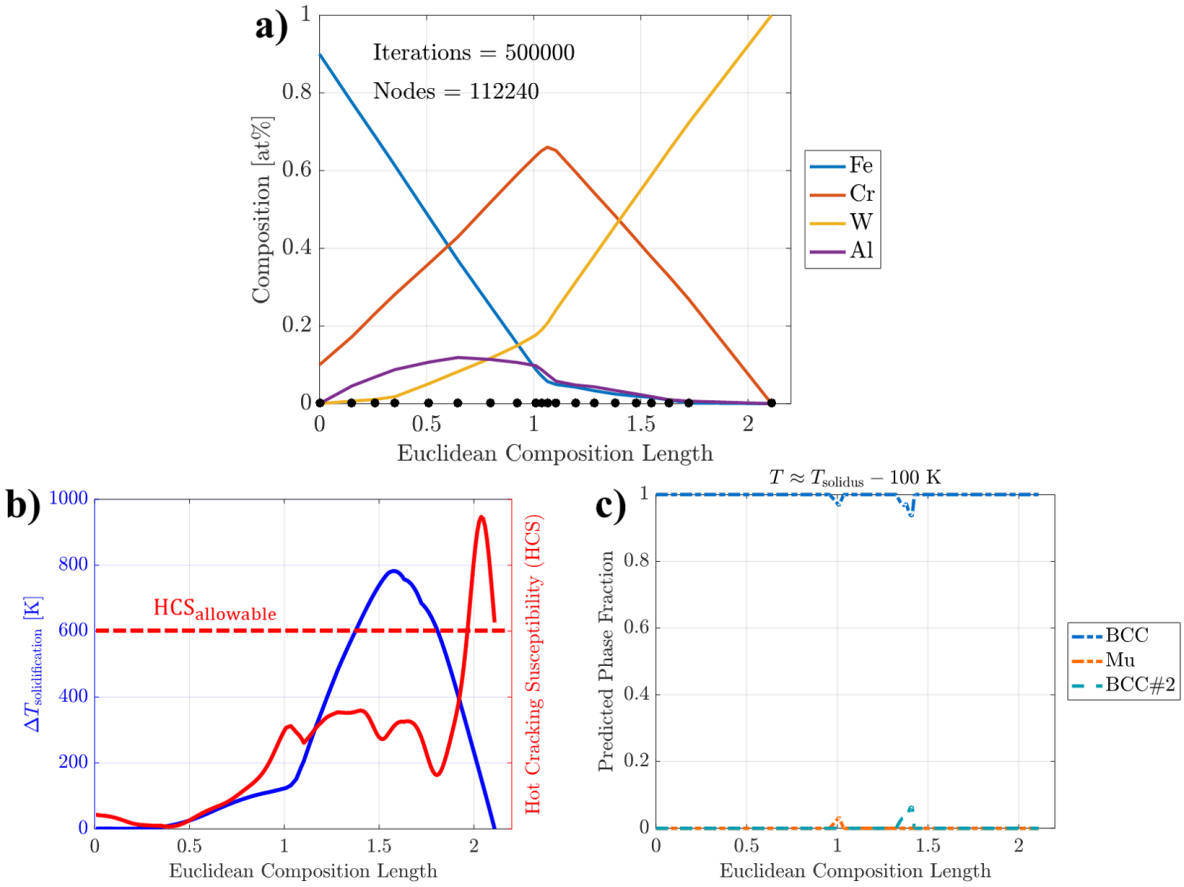

Figure 5.6: a) The optimal gradient path as planned by the algorithm in Fe-Cr-W-Al space after 500,000 iterations. The black dots along the x-axis represent the actual points sampled by the path planner. b) Predicted solidification range and Hot Cracking Susceptibility along the optimal path. c) Predicted phase fractions along the path 100 K below the predicted solidus temperature.

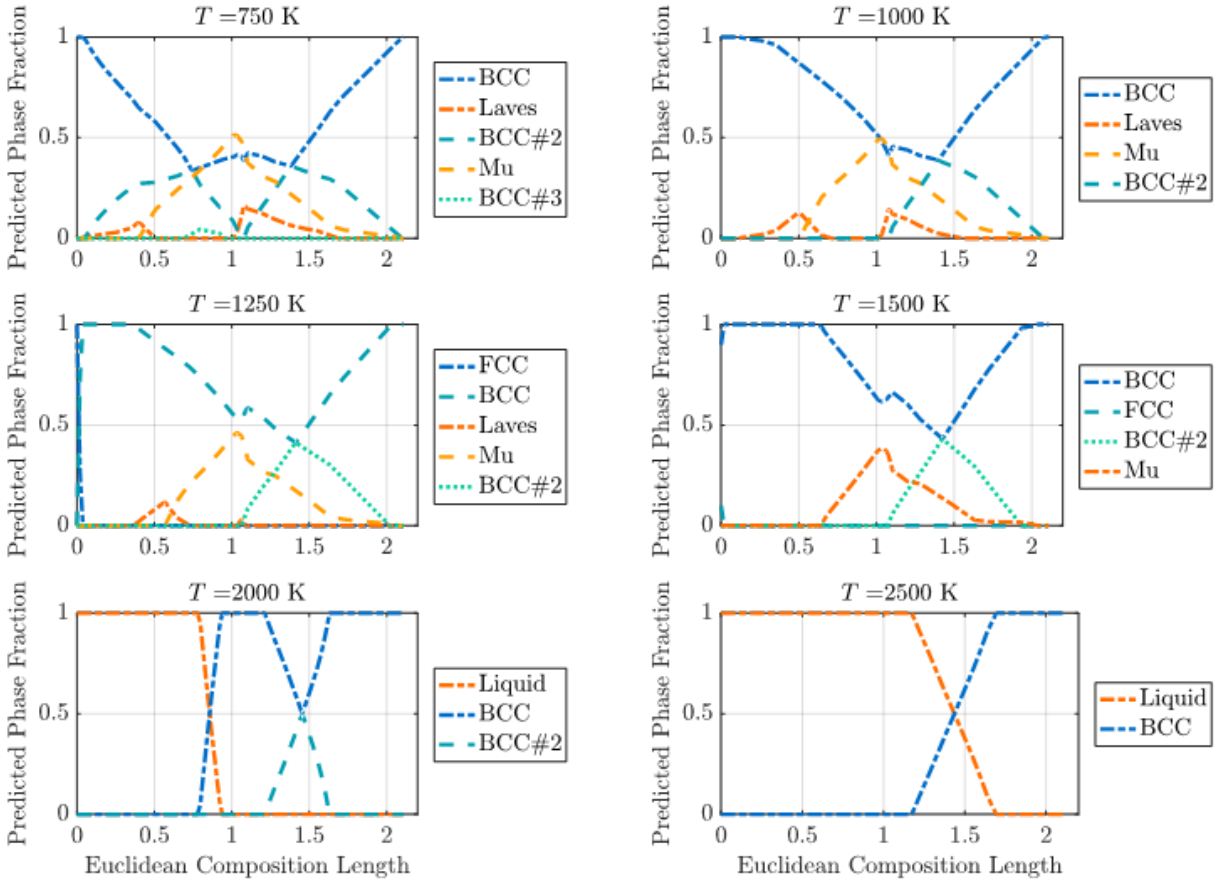

Figure 5.7: Equilibrium phase fractions along the optimal path (shown in Fig. 5.6a) at various temperatures. Note that the numbers assigned to common phases are numbered by descending fraction and might not be consistent with constitution.

constraints. Other objectives, like obstacle clearance, could provide paths that are farther away from constraint boundaries if avoiding constraints is of high priority.

5.2.4.2 Path Simplification

After analyzing the results of the path planning algorithm, the optimal path was simplified to make manufacturing easier and to maximize separation from constraint boundaries. To simplify the path, excess W was removed from the first half of the path and excess Fe and Al were removed from the second half of the path, then compositions were linearized where possible. The simplified

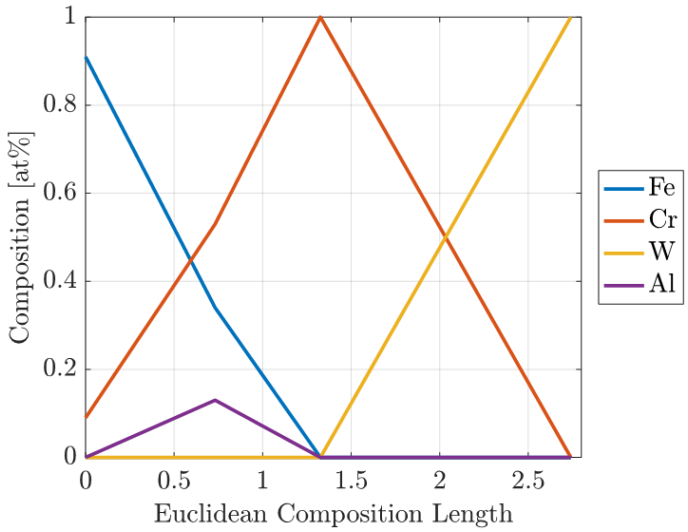

Figure 5.8: The optimal path (shown in Fig. 5.6a) simplified for experimentation.

path is shown in Fig. 5.8 and its critical compositions are listed in Table 5.1. The simplified path begins by traversing the Fe-Cr-Al ternary from Fe9Cr to pure Cr and then simply following the Cr-W binary from pure Cr to pure W. This path lies on the exactly on the edges and boundaries of the Fe-Cr-W-Al composition space and, as such, is impossible to discover via uniform random sampling of Fe, Cr, W, and Al. For a path planning algorithm to discover such a path, it would need to sample the lower dimensional subspaces (i.e. ternary and binary regions) directly.

Table 5.1: Critical compositions in simplified path from steel to tungsten

Sequence	x_{Fe} [at%]	x_{Cr} [at%]	x_{W} [at%]	x_{Al} [at%]
1	91	9		
2	34	53		13
3		100		
4			100	

The phase fractions along the simplified path at various temperatures are shown in Fig. 5.9.

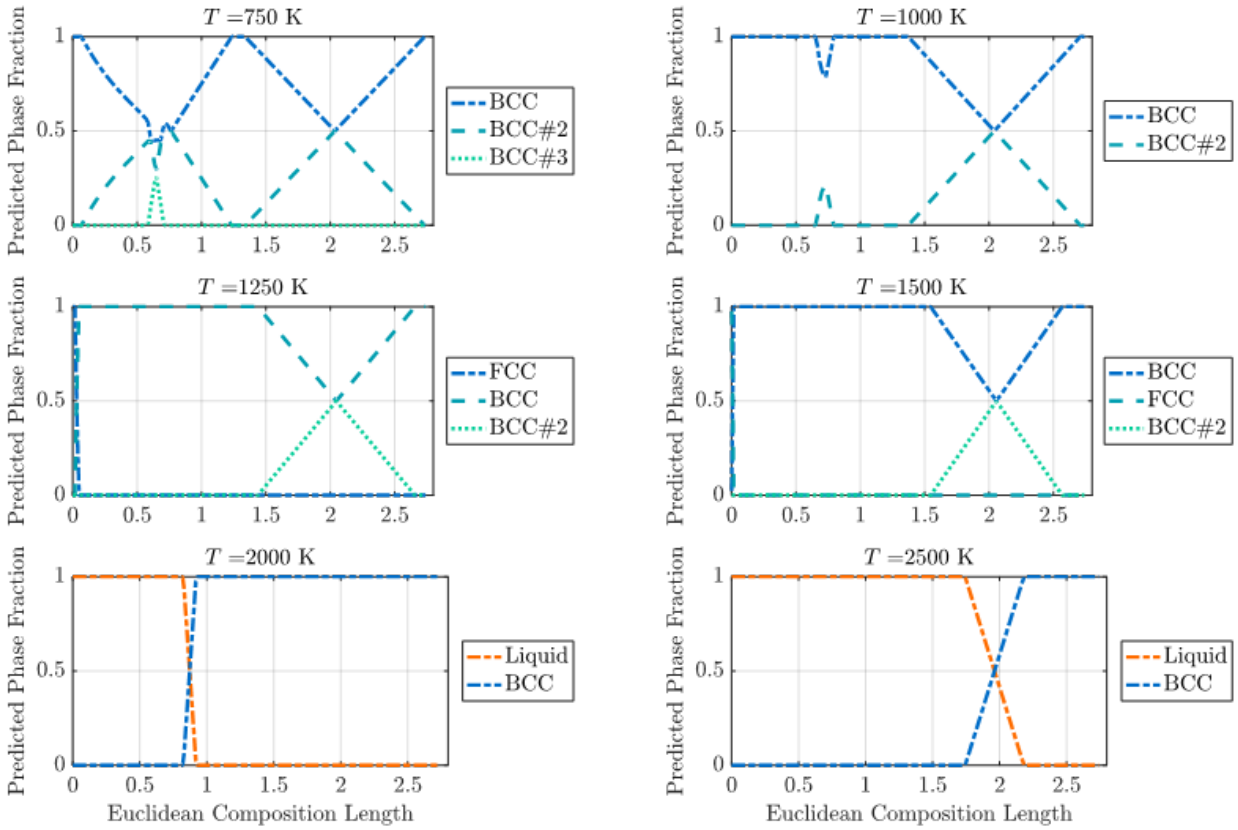

Figure 5.9: Equilibrium phase fractions along the simplified path (shown in Fig. 5.8) at various temperatures. Note that the numbers assigned to common phases are numbered by descending fraction and might not be consistent with constitution.

These plots show no deleterious phases at any of the selected temperatures. This is a significant improvement over the original optimal path, which showed up to 0.50 mole fraction of mu phase and up to 0.10 of laves. However, this simplified path is about 25% longer than the original path, indicating it is suboptimal to the original optimal path with respect to its problem formulation.

5.2.5 Experimental Results [†]

After the simplified path was designed and verified to satisfy design constraints, experiments were conducted by colleagues in Texas A&M University's Materials Science and Engineering

[†]Experiments and analysis conducted by Olga Eliseeva, Nick Barta, Prof. Ibrahim Karaman, and colleagues

Department to determine the success of the design. An Optomec LENS® MR-7 Directed Energy Deposition (DED) system was used to print prototype gradients from elemental powders of Fe, Cr, W and Al 6061 powder. Aluminum and tungsten are novel materials for DED manufacturing that have seen few successful demonstrations in DED. As such, a significant amount of work was done to calibrate processing parameters like feeder speeds as well as laser power, speed, and hatch spacing. While most parameters were able to be successfully calibrated, significant soot formation was observed in the Cr-W binary section of the gradient. This sooting was attributed to the vaporization of chromium powders at the temperatures required to melt tungsten and prevented the printing of the complete gradient to 100% W.

To test the portion of the planned gradient that could be manufactured, a gradient sample of 55 layers was printed from Fe9Cr to 50Cr50W [at%] on a steel substrate, with 5 layer dwells at each of the critical points listed in Table 5.1. This sample is shown as printed in Fig. 5.10a. While some surface cracks were observed as tungsten was added to the gradient, none of the cracks propagated into the sample and the build was successfully completed without catastrophic failures. The phases within the gradient were confirmed with XRD testing to be BCC, as predicted in Fig. 5.9. A 0.5-inch diameter, 0.5-inch tall cylinder was cut from a printed sample to produce the cylinder shown in Fig. 5.10.

Ultimately, the experiments confirm a significant portion of the gradient can be successfully manufactured. However, the most problematic portion of the gradient, as W becomes the majority element, was unable to be printed without defects. The vaporization temperature or boiling point of Cr is about 2945 K, more than 700 K below the melting point of W. This means these elements are practically incompatible to a significant extent. Unfortunately, this incompatibility was not recognized or captured in the design process. To get to pure tungsten, other elements like vanadium can offer similar avoidance of deleterious phases as chromium, with boiling points that are significantly higher (e.g. 3680 K for V).

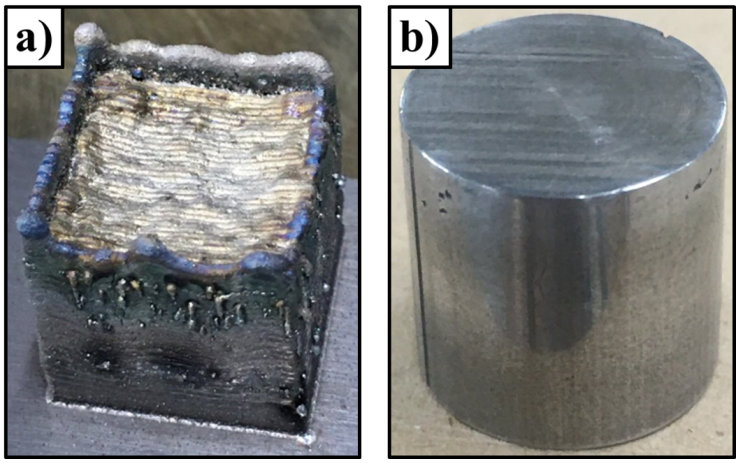

Figure 5.10: Simplified gradient path from Fe9Cr to 50Cr50W shown a) in a 55 layer sample as printed from a DED machine and b) in a 0.5-inch diameter, 0.5-inch tall sample machined by wire EDM.

5.3 Chapter Summary

Finding an alloy composition that can be printed via additive manufacturing without defects is often a difficult task. The challenge of finding a printable alloy is significantly amplified when designing a compositionally graded alloy, as a gradient represents a continuous range of compositions that each must be printable. There are several manufacturing metrics that can be used to assess the printability of a composition. The proposed gradient design methodology can incorporate these metrics into the constraint formulation to avoid compositions that are not likely to be printable.

Constraints that consider manufacturing were demonstrated in the design of a gradient between steel and tungsten. These metrics, solidification range and a Hot Cracking Susceptibility (HCS) criterion, predict hot tearing and can be computed with CALPHAD models. The large variance in melting temperatures in the Fe-Cr-W-Al composition space poses many unique challenges for additive manufacturing that can be predicted by these metrics. Nevertheless, a feasible gradient was found that satisfied the design constraints. This gradient was simplified by exploiting the Cr-W binary edge to eliminate deleterious phases at lower temperatures. It is nearly impossible to

discover the boundaries of the space (i.e. binary edges) with the current implementation of the methodology. Possible techniques around this limitation are discussed in Chapter 8.

A significant portion of the designed gradient was printed with a directed energy deposition process and was shown to be printable with no deleterious phases. However, the tungsten-rich portion of the gradient produced critical sooting and loss of chromium due to chromium vaporization, which has a vaporization temperature 700 K less than the melting temperature of tungsten. Unfortunately, this was not recognized and represented in the design methodology, but similar elements with higher vaporization temperatures, like vanadium, could be added to the design space to likely reach pure tungsten successfully.

Other manufacturing metrics that can be predicted as a function of composition can be easily implemented into the methodology. Although, too many constraints can easily over-constrain the design space and leave little room for feasible paths. Cost functions like path length necessarily produce paths that lie on constraint boundaries, which can be problematic if constraints are not conservative or if there associated uncertainties. The issues of over-constraining the design space or planning near constraint boundaries can both be mitigated by using a cost function that considers constraint violation as an objective, as discussed in the next chapter.

6. OPTIMIZING FOR CONSTRAINT VIOLATION *

If too many constraints are applied to a gradient design problem it can become over-constrained and reduce or eliminate the methodology's ability to find feasible paths. It is sometimes better to represent some design requirements as soft constraints in the form of a penalty cost term. Such a term can be used in the cost function to minimize constraint violation. This chapter demonstrates the use of a penalty constraint on intermetallic phase formation in a gradient between steel and aluminum. While avoiding intermetallics as obstacles is nearly impossible in this system, considering them as penalized costs enabled the discovery of a path with minimal amounts of intermetallics. Experiments conducted on selected compositions from the simplified path validate phase predictions, but the full gradient was unable to be printed due to manufacturing limitations.

6.1 Cost Function: Minimize Constraint Violation

It can be difficult or impossible to find feasible gradient design paths if the state space is over-constrained. For example, gradient design problems in composition spaces with many deleterious phases or large deleterious phase regions can leave little room for valid paths. Composition spaces with incompatible elements or elements with large differences in melting temperature can also pose problems. Even if feasible paths exist, if there are too many hard constraint boundaries or obstacles in the state space then a path planning algorithm can have difficulties finding solutions in narrow passageways. However, the problems introduced by too many hard constraints can be mitigated by treating some constrained variables as soft constraints and considering them in the cost function.

The idea of treating constrained problems as unconstrained by moving constraints into the objective is common in the optimization community. These types of objective functions are called penalty functions because the objective value is penalized if constraints are violated. These penalty

*Part of this research was carried out at the Jet Propulsion Laboratory, California Institute of Technology, and was sponsored by the JPL Summer Internship Program, the JPL Space Technology Office, and the National Aeronautics and Space Administration (80NM0018D0004)

functions typically include the original objective as well as a measure of constraint violation that is multiplied by a penalty parameter. If the penalty parameter is high, the optimizer will prioritize minimizing constraint violation and could even find solutions where constraints are not violated, if they exist.

One issue with including constraint violation in the cost function is the tuning of the penalty parameter. As with other multi-objective problems, this parameter might lead to behavior that is misaligned with designer preferences. Another concern is that the constraint values of the optimal solution might still violate design requirements. Designers should take special care to choose the penalty function and penalty parameters to represent their preferences as well as possible. As a general rule, constrained values that are more important or more detrimental to a successful design should be assigned higher penalty parameters.

6.2 Case Study: Steel to Aluminum

The following case study demonstrates the use of a cost function that minimizes constraint violation. The chosen design space is five-dimensional and is rife with deleterious phases, particularly aluminum intermetallics. It is shown that if all deleterious phase regions were to be treated as hard obstacles very little space would be available for planning. However, a feasible solution can be found by considering the most problematic phases, aluminum intermetallics, as penalized constraints.

6.2.1 Problem Description

6.2.1.1 Motivation

Steel and aluminum alloys are two of the most common metals in engineering applications, but typically serve two contradictory goals in engineering design. Steel is often used to satisfy structural requirements when designs demand high strength and ductility like in buildings, motor vehicles, appliances, tools, etc. Aluminum, on the other hand, is valued for its low density and high specific strength which has led to its prolific use in the aerospace industry. A feasible gradient between steel and aluminum would allow designers to exploit the best characteristics of both

materials simultaneously. Hypothetically, the best multimaterial design would place steel where structural requirements are highest and aluminum elsewhere to minimize the mass of the total design, outperforming either single material solution when mass and strength are both performance objectives.

The following case study was supported by and conducted in collaboration with NASA's Jet Propulsion Laboratory (JPL), which has been a pioneer in the area of compositionally graded alloys [1, 58, 59, 61]. As with many other engineering applications, steel and aluminum are two of the most abundant materials on JPL's spacecraft, but JPL is interested in a potential gradient because of the unique benefits it could offer to spacecraft design. Mass minimization is of the utmost importance when designing for spaceflight so the obvious benefits to light-weighting are even more lucrative. Additionally, gradient materials offer another benefit in that they eliminate the need for traditional joining methods like bolts or welds. These methods require their own rigorous verification and validation procedures which incur high costs in labor and time. Joining parts, like nuts and bolts, also add additional mass to the overall spacecraft. Finally, since JPL's spacecraft are highly designed, custom-built products the specialized manufacturing processes of gradient materials can be afforded if they offer sufficient design improvements.

6.2.1.2 Problem Definition

To begin defining the gradient design problem, the start and goal compositions were initially set to stainless steel (Fe72Cr16Ni12 [at%]) and pure Aluminum. Thermo-Calc's TCHEA2 was used to examine the phases along the linear gradient between these compositions at temperatures that decreased linearly from 1300 K at stainless steel to 900 K at pure aluminum, in order to replicate how manufacturing temperatures might decrease to accommodate the much lower melting temperature of aluminum. The compositions and temperatures along the linear gradient can be seen in Fig. 6.1a, while the equilibrium phases at each condition in the gradient can be seen in Fig. 6.1b. Figure 6.1 demonstrates that the aluminum-rich portion of the gradient is dominated by a multitude of intermetallic compounds. In fact, aluminum is predicted to form multiple intermetallics with each element in the initial stainless steel composition (Fe, Ni, and Cr). These intermetallics are

known to be brittle and have been shown to reduce tensile strength and initiate cracks in dissimilar welds between aluminum and steel [126, 69, 51].

Given aluminum's tendency to form intermetallics with iron, nickel, and chromium, it is evident that a new element needs to be introduced to find a gradient that avoids these phases. To this end, a search was conducted through Al-X binary phase diagrams to find a new candidate element. While aluminum forms intermetallics with many metals, titanium was eventually selected after the identification of Al3Ti as a potentially promising compound. The Al-Ti binary exhibits a simple, two-phase region between Al3Ti and pure Al, meaning that pure Al can be approached from Al3Ti without producing tertiary phases. Recent evidence also suggests that the ductility of Al3Ti can be significantly improved with addition of excess aluminum [127], indicating that it might be the best Al-rich intermetallic to combine with the FCC phases of common aluminum alloys. For these reasons, titanium was added to the gradient design space and Al3Ti was made to be the goal composition for the path planning algorithm (the Al-Ti binary can then be traversed to reach pure aluminum).

6.2.2 Design Space Exploration

Thermo-Calc's TCHEA2 database was used to gather nearly 150,000 samples of equilibrium phase information from a uniform random sampling of Fe-Ni-Cr-Al-Ti-Temperature space, where each element ranged from 0 to 1 atomic fraction and temperature ranged from 400 to 1800 K. These samples were used to visualize the design space and construct feasible phase constraints. Marginal distributions of the thermodynamic conditions (i.e. compositions and temperature) that produced some amount of each major deleterious phase can be seen in Fig. 6.2. These distributions can be used to see which conditions are likely to produce deleterious phases. For example, Fig. 6.2 shows the conditions predicted to produce G-phase are high aluminum and, to a lesser extent, titanium contents at relatively lower temperatures. In fact, G-phase is present in 56.2% of the Al-rich (Al > 50 at.%) samples. On the other hand, laves phase occurs in mostly in compositions with significant amounts of Fe and Ti, but was present in only 2.44% of Al-rich samples. Sigma phase is commonly associated with steels, but is hardly present in Al-containing alloys. Fig. 6.2d shows

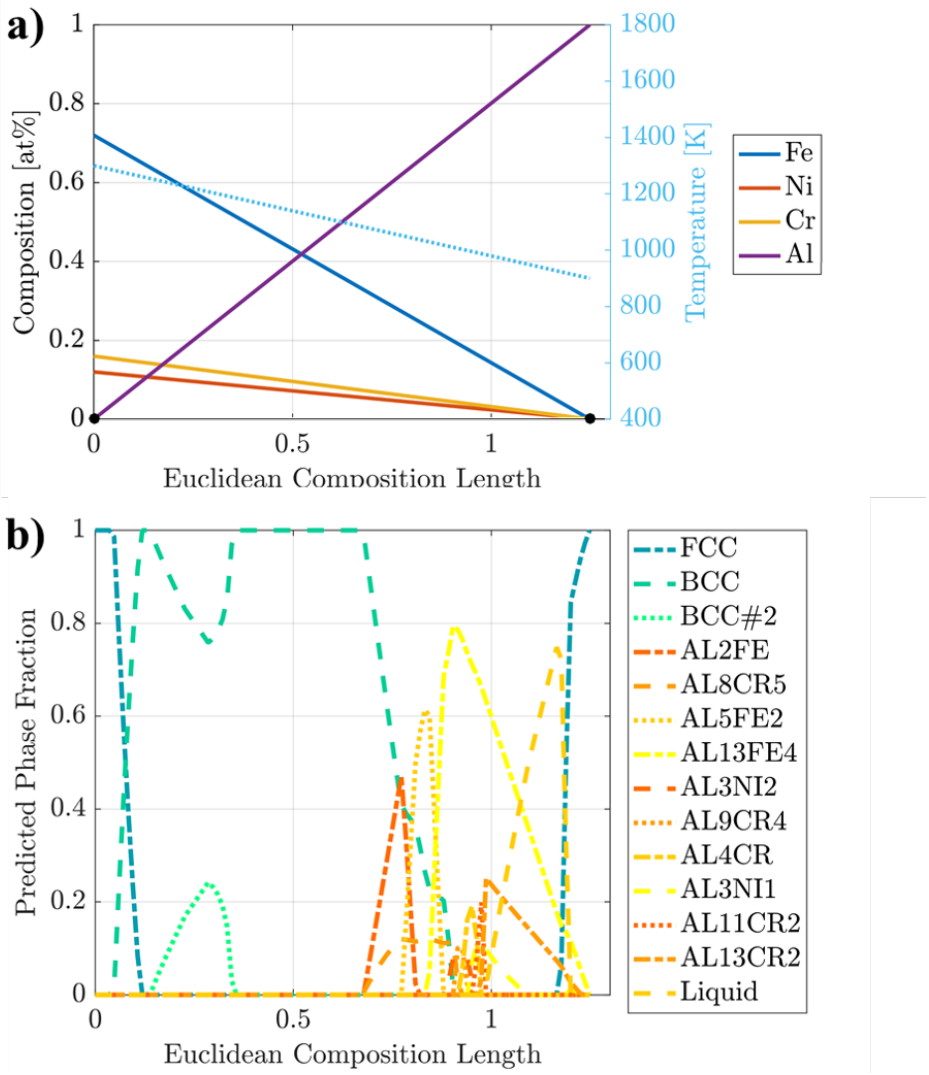

Figure 6.1: a) The compositions and temperatures used to study the phases present in a linear gradient between steel and aluminum. b) The predicted equilibrium phase fractions along the linear gradient. Note that the numbers assigned to common phases are numbered by descending fraction and might not be consistent with constitution.

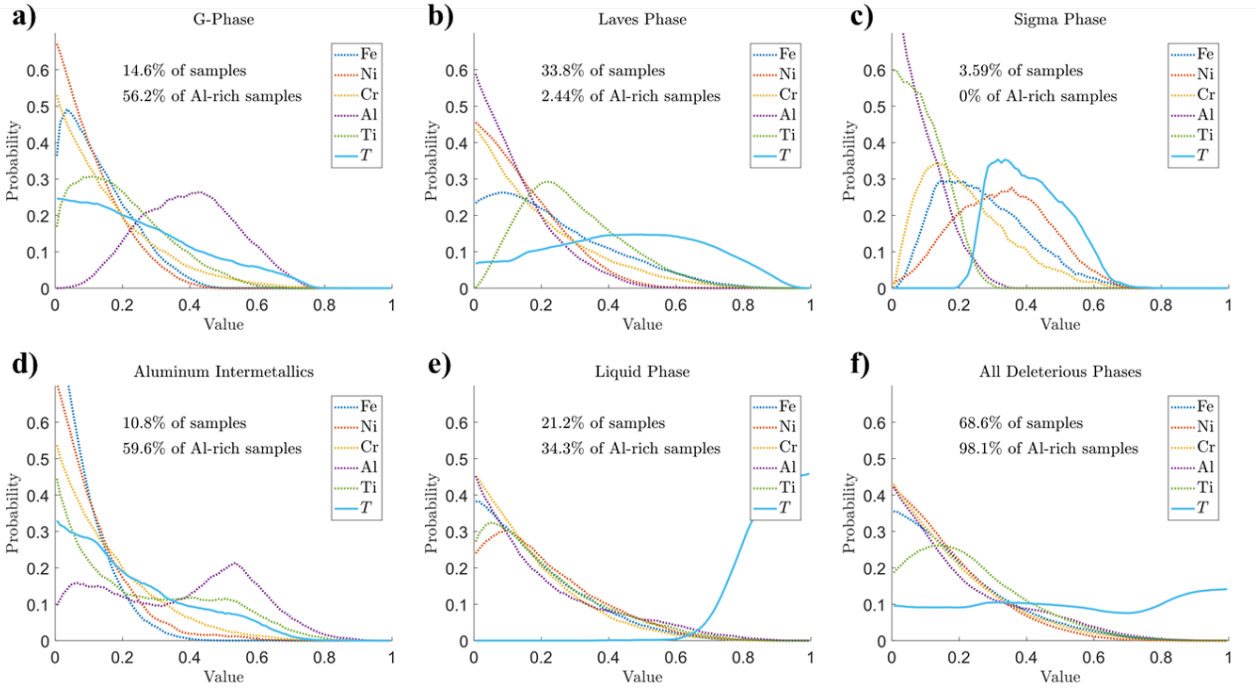

Figure 6.2: Distributions of samples in Fe-Ni-Cr-Al-Ti-Temperature space that contained greater than 0.01 mole fraction of a) G-phase, b) laves phase, c) sigma phase, d) aluminum intermetallic phases, e) liquid phase, and f) any deleterious phase. Temperature values are normalized between 400 and 1800 K.

that, as expected, aluminum intermetallics dominate the Al-rich samples appearing in 59.6% of such compositions.

Figure 6.2f shows the marginal distribution of all conditions that produced any deleterious phase (G-phase, laves, sigma, liquid, or any aluminum intermetallic). Critically, these phases are present in 98.1% of Al-rich space and therefore occupy almost all of the design space near aluminum. Consequently, it is highly unlikely that any path planning algorithm could find a feasible path in Al-rich space if these phases are treated as hard constraints or obstacles.

To address this issue, phases were reevaluated to determine their likely impact on a successful gradient. After this reevaluation, the prevalence of G-phase in Al-rich regions appeared in stark contrast to the available literature. G-phase has long been identified as an intermetallic silicide present in stainless steels, but has, to the author's knowledge, never been observed without sili-

con or associated with Al-rich compositions [128, 129, 130]. Further investigation also revealed that the Fe-Cr-Al and Fe-Cr-Ti ternary phase diagrams had only been "tentatively" assessed in the TCHEA2 database [131], meaning that the phase models in these ternary spaces were not completely fit to experiments in the relevant composition and temperature ranges. These two observations led to the decision to suppress G-phase in the phase modeling, as its presence is likely an artificial projection from phase models fit to steel data.

After deciding to suppress G-phase, new samples were gathered from TCHEA2 with G-phase set to be dormant (i.e. not considered). The marginal distributions of the thermodynamic conditions associated with deleterious phases after setting G-phase to be dormant can be seen in Fig. 6.3. Notably, the number of samples containing laves phase increased after suppressing G-phase, particularly in the Al-rich region where laves phase grew from appearing in just 2.44% to 20% of Al-rich compositions. The presence of sigma phase, liquid phase, and aluminum intermetallic phases, however, did not appear to change significantly after setting G-phase to be dormant. As such, aluminum intermetallic phases still occupied nearly 60% of the Al-rich samples. When these intermetallics are combined with the sigma, laves, and liquid phases, all deleterious phases still occupy more than 95% of Al-rich space. However, the sigma, laves, and liquid phases alone only occupy 53.2% of Al-rich space, as seen in Fig. 6.3f. It was therefore decided to remove aluminum intermetallics as a hard constraint and instead attempt to minimize them in a penalty cost function. In this way, the path planning algorithm has enough free space to plan feasible paths while also minimizing the amount of aluminum intermetallics.

6.2.3 Penalty Cost Function

To minimize the amount of aluminum intermetallics present in the designed gradient path, a penalty cost function was devised that increased cost in proportion to the phase fraction of aluminum intermetallics. The form of the penalty cost function can be seen in Eqn. 6.1, where c_{penalty} is the penalty cost associated with the path segment, σ_k. The key term in Eqn. 6.1 is $\max\left(f_{\text{intermetallic}}(\sigma_k)\right)$ which refers to the maximum phase fraction of aluminum intermetallics along path segment σ_k. The form of Eqn. 6.1 is such that increasing values of this term have

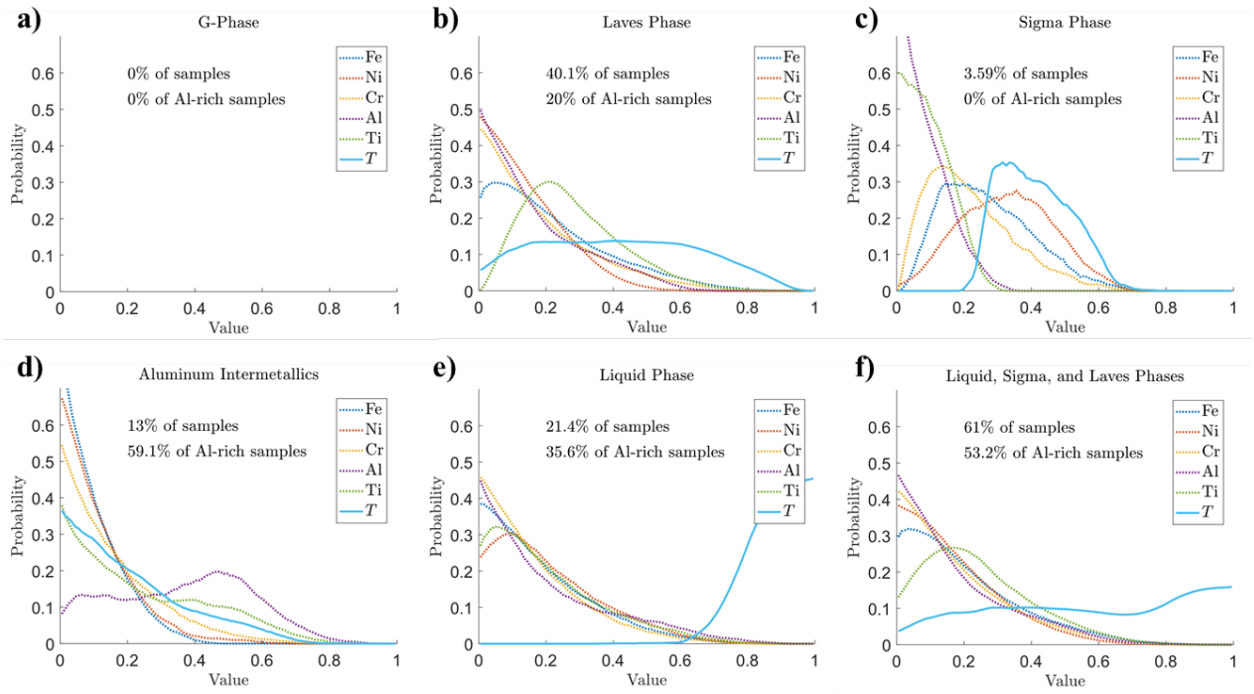

Figure 6.3: Distributions of samples in Fe-Ni-Cr-Al-Ti-Temperature space, after setting G-phase to be dormant, that contained greater than 0.01 mole fraction of a) G-phase, b) laves phase, c) sigma phase, d) aluminum intermetallic phases, e) liquid phase, and f) any of either the liquid, sigma, or laves phases. Temperature values are normalized between 400 and 1800 K.

an increasingly dramatic effect on the cost. Note that the value of c_{penalty} is zero when the phase fraction of aluminum intermetallics is zero and that the limit of c_{penalty} as the phase fraction of aluminum intermetallics increases to one is infinity.

$$c_{\text{penalty}}(\sigma_k) = \frac{1}{\left(1 - f_{\text{intermetallic, avg}}(\sigma_k)\right)^2} - 1 \tag{6.1}$$

Before the penalty cost described in Eqn. 6.1 can be used by a path planning algorithm, it must to be easy to compute for every potential path segment. To reduce computational expense, the nearly 150,000 samples of TCHEA2 used to explore the design space in Fig. 6.3, when G-phase was dormant, were used to train a machine learning regressor to predict the phase fraction of aluminum intermetallics, $f_{\text{intermetallic}}$, as a function of composition and temperature. MATLAB's

support vector machine (SVM) regression tool (`fitrsvm`) was used to train an SVM model with a Gaussian kernel on the aforementioned phase data. The coefficient of determination, R^2, of the model was 0.847 and the model's root mean square error (RMSE) on the training data was 0.0597. The phase fractions predicted by the model for the training data are shown plotted against the actual phase fractions in Fig. 6.4a. Figure 6.4 shows several points with significant errors, but in the context of a much larger sample size and acceptable R^2 and RMSE values, the model was deemed to be sufficiently accurate.

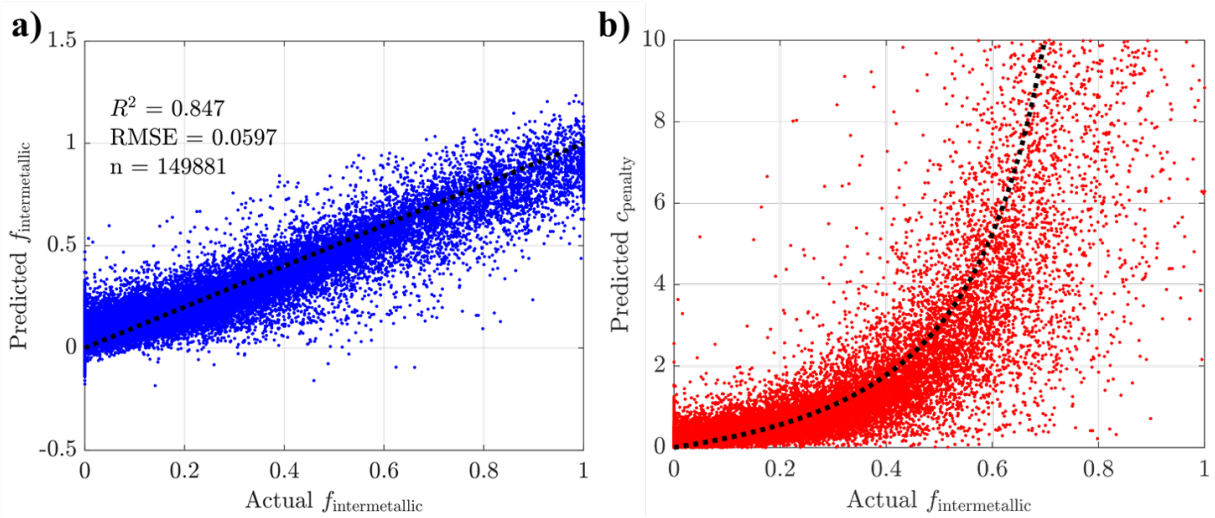

Figure 6.4: a) Predicted versus actual intermetallic phase fraction as predicted by the SVM regressor on the training data. b) The predicted penalty cost (Eqn. 6.1) for each training point versus the actual intermetallic phase fraction. The black dotted lines represent the results a perfect regressor would produce.

Figure 6.4b shows the penalty cost in Eqn. 6.1 for a point path segment ($\sigma_k(0) = \sigma_k(1)$) with $f_{\text{intermetallic}}$ predicted by the trained SVM model plotted against the actual phase fraction. The dotted black line represents the analytical form of Eqn. 6.1. As discussed, the form is such that c_{penalty} approaches infinity as the aluminum intermetallic phase fraction approaches one. As with Fig. 6.4a, Fig. 6.4b shows several points with high intermetallic phase fractions that have low

associated penalty costs and vice versa, but as these points are a small subset of a much larger sample size they were deemed to be insignificant.

6.2.4 Optimization Problem

The chosen design space for the gradient path design problem is represented in Eqn. 6.2. The design space consists of four elements, with iron as a balance element, as well as temperature. Temperature was chosen as a design variable in this problem due to the drastic difference in melting temperatures between aluminum (933 K) and stainless steel ($\sim$1700 K). This large difference means that the temperature at which the gradient is additively manufactured must change during the build and cannot be easily approximated without first knowing the compositions in the gradient. Also, taking a conservative approach to phase avoidance and collapsing the temperature dimension would likely lead to few feasible paths given the prevalence of deleterious phases at low-temperatures that might not even appear during the rapid solidification of the build process.

$$z = \left\{ x_{\text{Ni}}, x_{\text{Cr}}, x_{\text{Al}}, x_{\text{Ti}}, T : x_{\text{Fe}} = 1 - \sum_{i=1}^{4} x_i \text{ and } x_i \geq 0 \ \forall \, i \right\} \tag{6.2}$$

The goal of the gradient path design problem is to find the path through the design space that optimizes the cost function, $c(\sigma)$, while satisfying the constraints. The cost function considered in this case study was multi-objective and minimized path length as well as the penalty incurred by intermetallic phases, c_{penalty} in Eqn. 6.1. The segment-wise path length, l_k, was calculated as the euclidean distance between the endpoints of the segment in the design space, where temperature was normalized between 400 and 1800 K. Including length in the objective function promotes paths that are simpler to manufacture and also minimize the use of excess materials, like titanium in this problem. A scalar weighting of 10 was applied to the length portion of the cost function to better balance the scale of this objective to that of c_{penalty}. Because the path planning algorithm used (RRT*FN [3]) was implemented in a cumulative form, the cost function must be represented as a summation of segment-wise costs (those depending on each linear segment k).

The first set of constraints considered in this case study represent the deleterious phases that

can be easily avoided with hard constraints: the liquid, sigma, and laves phases. Computationally, a MATLAB k-nearest neighbors classifier (`fitcknn`, $k = 3$) was trained on the phase data (G-phase dormant) to represent regions in the design space that produce greater than 0.01 mole fraction of these phases. This classifier was then used to evaluate constraint violation in the path planning algorithm. Another set of constraints ensure that the path starts and ends at the initial and goal conditions: stainless steel and Al3Ti, respectively. The optimization problem formulation is summarized below.

$$
\begin{aligned}
\textbf{Find} \quad & \sigma_{\text{best}} = \underset{\sigma}{\textbf{arg min}} \ \left[c(\sigma) = \sum_{k=1}^{n} \left(10 l_k + c_{\text{penalty}}(\sigma_k) \right) \right] \\
\textbf{subject to} \quad & \sigma(\alpha) \in Z_{\text{free}} \ \forall \, \alpha \in [0,1], \\
& Z_{\text{free}} = \Big\{ z : f_{\text{liquid}}(z), f_{\text{sigma}}(z), f_{\text{laves}}(z) < 0.01 \Big\}, \\
& \sigma(0) = z_{\text{init}} = \big\{ x_{\text{Ni}} = 0.12, x_{\text{Cr}} = 0.16, x_{\text{Al}} = 0, x_{\text{Ti}} = 0, T = 1300K \big\}, \\
& \sigma(1) = z_{\text{goal}} = \big\{ x_{\text{Ni}} = 0, x_{\text{Cr}} = 0, x_{\text{Al}} = 0.75, x_{\text{Ti}} = 0.25, T = 900K \big\}.
\end{aligned}
$$

6.2.5 Optimal Gradient Path

6.2.5.1 Algorithm Results

Figure 6.5a displays the cost of the optimal path versus the number of algorithm iterations. The total cost quickly approaches an asymptote after around 100,000 iterations, but small improvements are made to the penalty term even after 500,000 iterations. The algorithm was stopped after 700,000 iterations as only marginal improvements in the costs were being achieved. The wall-clock time taken by the algorithm on a quad-core, 3.40 GHz processor with 12 GB RAM is plotted against algorithm iterations in Fig. 6.6 along with the number of collision checks. The total runtime is on the order of days or weeks as the number of iterations exceeds several hundred thousand.

The optimal gradient path found after 700,000 iterations of the path planning algorithm is

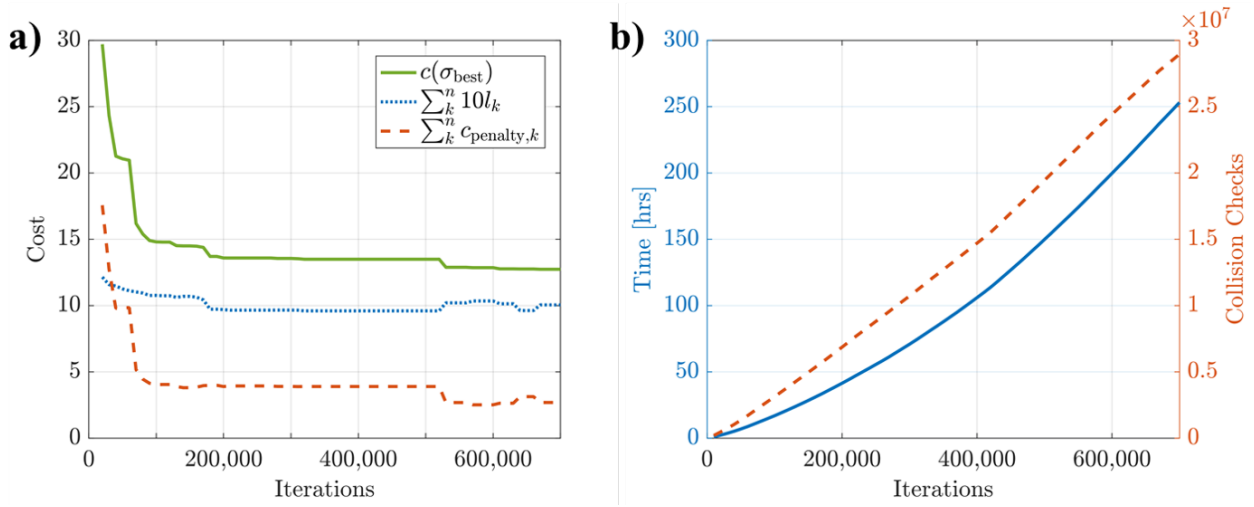

Figure 6.5: a) The total cost of the best path, as well the length and penalty contributions to the cost, plotted versus algorithm iterations. b) The runtime of the algorithm in hours and the number of collision checks plotted versus algorithm iterations.

shown in Fig. 6.6a. In that time, over 255,000 nodes or feasible conditions were added to the tree. The algorithm successfully reached the goal condition, Al3Ti, but to make a complete path from steel to aluminum the path was manually extended though the Al-Ti binary by increasing aluminum while holding the temperature constant.

Figure 6.6b shows the equilibrium phase fractions along the optimal path as predicted by Thermo-Calc's TCHEA2 database. As shown in Fig. 6.6b, the algorithm successfully avoided the deleterious phases considered as hard constraints (liquid, laves, or sigma). However, several intermetallics (Al13Fe4, Al5Fe2, Al3Ni2, and Al2Ti) appear in the gradient as the path approaches Al3Ti (referred to as BCT in phase plots due to its Body Centered Tetragonal structure). These intermetallics occupy a relatively small portion of the gradient, contained to about 15% of the total composition length. They also appear in concentrations of no more than 0.2 mole fraction. For comparison, in the linear gradient between steel and aluminum, shown in Fig. 6.1, ten different intermetallics appear in nearly half the compositional length of the gradient. The intermetallics in the linear gradient also appear in a mole fraction of up to 0.8 and a section of the linear gradient is entirely composed of intermetallic phases. The algorithm was able to find a path with much less

intermetallics than the linear gradient, though the penalty cost function was unable to eliminate intermetallics entirely.

6.2.5.2 Path Simplification

After examining the optimal path found by the algorithm, the path was simplified to minimize the amount of intermetallic phases and to streamline manufacturing. The intermetallics encountered by the optimal path with the largest phase fractions involve only aluminum and iron: Al13Fe4 and Al5Fe2. In an effort to reduce the concentration of these phases, the amount of both aluminum and iron was reduced slightly in the region just before the gradient path reaches Al3Ti. Otherwise, the optimal path was simplified by merely linearizing the sections of the optimal path that were already nearly linear. The resulting simplified path is shown in Fig. 6.7a while critical points are shown in Table 6.1.

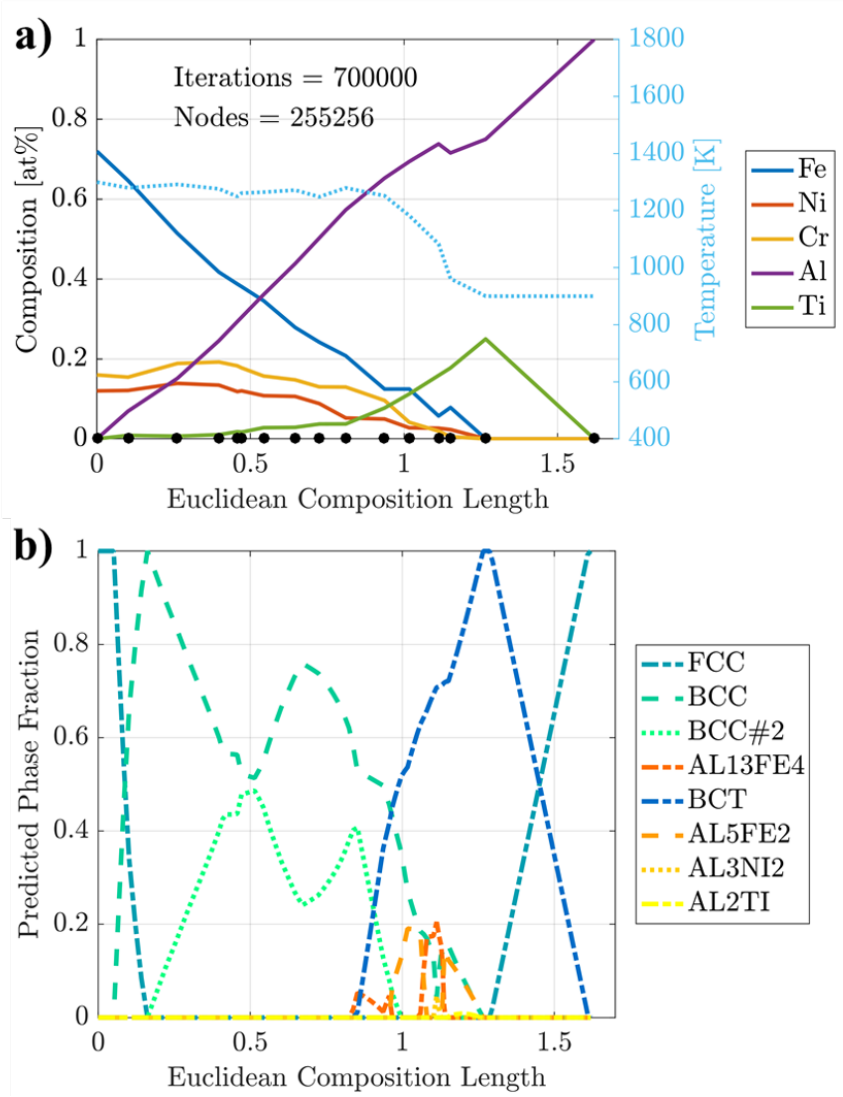

Figure 6.6: a) The optimal gradient path as planned by the algorithm in Fe-Ni-Cr-Al-Ti-Temperature space after 700,000 iterations. The black dots along the x-axis represent the actual points sampled by the path planner. b) Equilibrium phase fractions along the optimal gradient path as predicted by Thermo-Calc's TCHEA2. Note that the numbers assigned to common phases are numbered by descending fraction and might not be consistent with constitution.

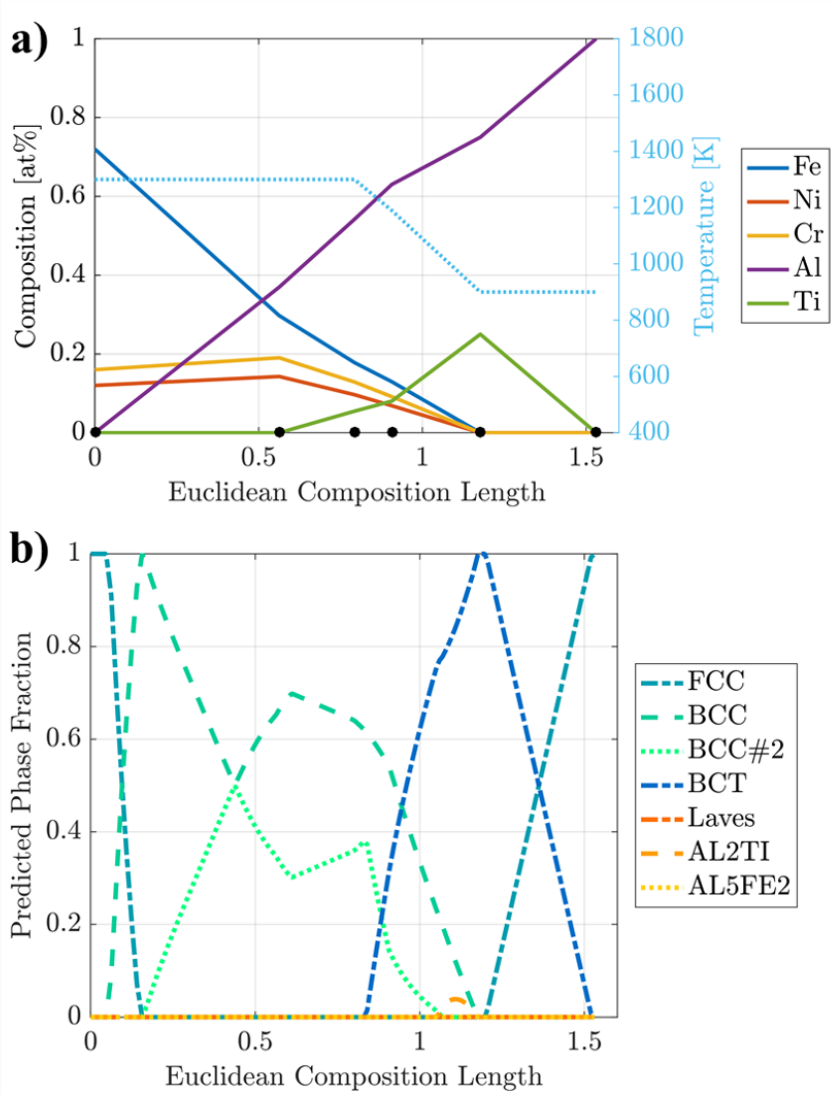

Figure 6.7: a) The simplified gradient path in Fe-Ni-Cr-Al-Ti-Temperature space. The black dots along the x-axis represent the critical points in the simplified path. b) Equilibrium phase fractions along the simplified gradient path as predicted by Thermo-Calc's TCHEA2. Note that the numbers assigned to common phases are numbered by descending fraction and might not be consistent with constitution.

The phases predicted by TCHEA2 to appear in the simplified path are shown in Fig. 6.7b. The slight simplifications from the optimal path found by algorithm, shown in Fig. 6.6, reduced the amount of intermetallic phases below any significant threshold. As discussed, this can be attributed to the slight reduction in aluminum and iron concentrations before the path reaches Al3Ti. Even

Table 6.1: Critical conditions in simplified path from steel to aluminum

Sequence	x_{Fe} [at%]	x_{Ni} [at%]	x_{Cr} [at%]	x_{Al} [at%]	x_{Ti} [at%]	T [K]
1	72	12	16			1300
2	29.7	14.3	19.0	37.0		1300
3	17.8	9.7	12.9	54.2	5.5	1300
4	12.9	6.9	9.2	63.0	8.0	1190
5				75	25	900
6				100		900

though the algorithm did not find this simplified path, it appears to be optimal with respect to the specified problem formulation.

6.2.6 Experimental Results[†]

6.2.6.1 Arc Melting to Validate Phase Predictions

Experiments were conducted by colleagues at Texas A&M University to validate the simplified gradient in Fig. 6.7 and its predicted phase fractions. Before attempting to print the full gradient, four alloy compositions were selected at critical locations in the gradient for closer study. These alloys represent critical regions where the phases of the gradient can be easily tested. The compositions of all four alloys and their predicted phase fractions near solidification are listed in Table 6.2. The locations of each alloy in the gradient are marked and visualized with relation to predicted phase fraction in Fig. 6.8.

To validate the predicted phases, samples of each alloy were arc melted and heat treated at 950 °C for a long period of time to allow kinetics to reach equilibrium. Scanning Electron Microscopy (SEM) with Backscattered Electron (BSE) imaging was used to examine the microstructures and phases of each alloy, as seen in Fig. 6.9.

[†]Experiments and analysis conducted by Olga Eliseeva, Nick Barta, Prof. Ibrahim Karaman, and colleagues

Table 6.2: Selected compositions for arc melting experiments

Alloy	x_{Fe} [at%]	x_{Ni} [at%]	x_{Cr} [at%]	x_{Al} [at%]	x_{Ti} [at%]	Predicted Phases
Alloy 1	29.7	14.3	19.0	37.0		100% BCC
Alloy 2	16.6	8.9	11.9	56.5	6.1	100% BCC
Alloy 3	11.0	5.8	7.7	65.5	10.0	50% BCC, 50% BCT
Alloy 4	4.8	2.2	2.9	71.5	18.6	25% BCC, 75% BCT

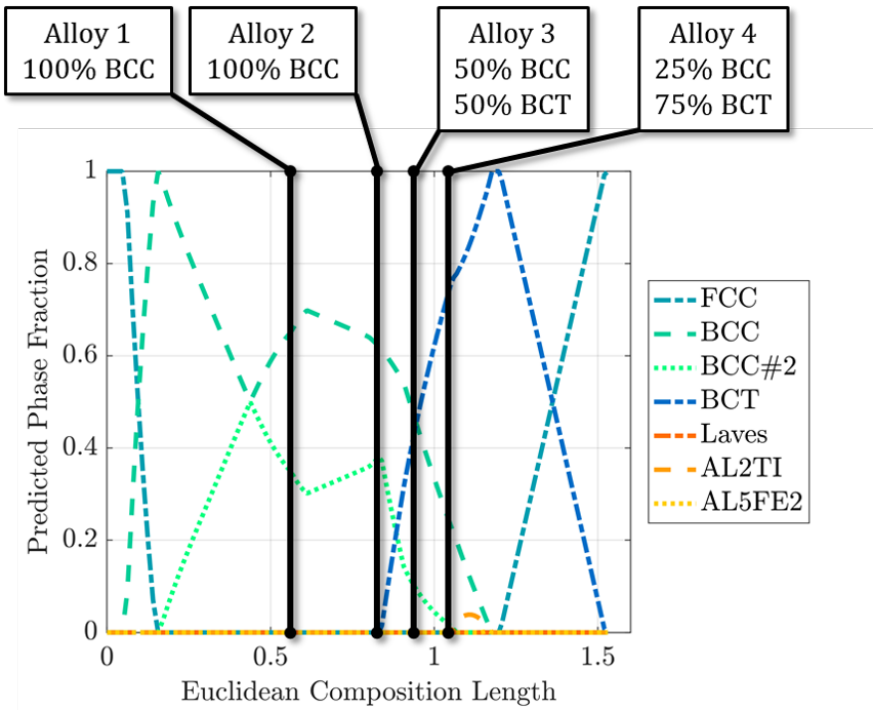

Figure 6.8: Approximate locations of the arc melted alloys in Table 6.8 along the planned gradient in relation to predicted phase fraction near solidification.

Alloy 1 lies near the middle of the BCC portion of the planned gradient and is predicted to form only BCC phases between 1000 and 1600 K. The microstructure of the arc melted sample, shown in Fig. 6.9a, is very finely structured. XRD phase analysis of the sample also agreed very well with theoretical BCC peaks. Both of these results indicate that this alloy indeed contains only BCC as predicted.

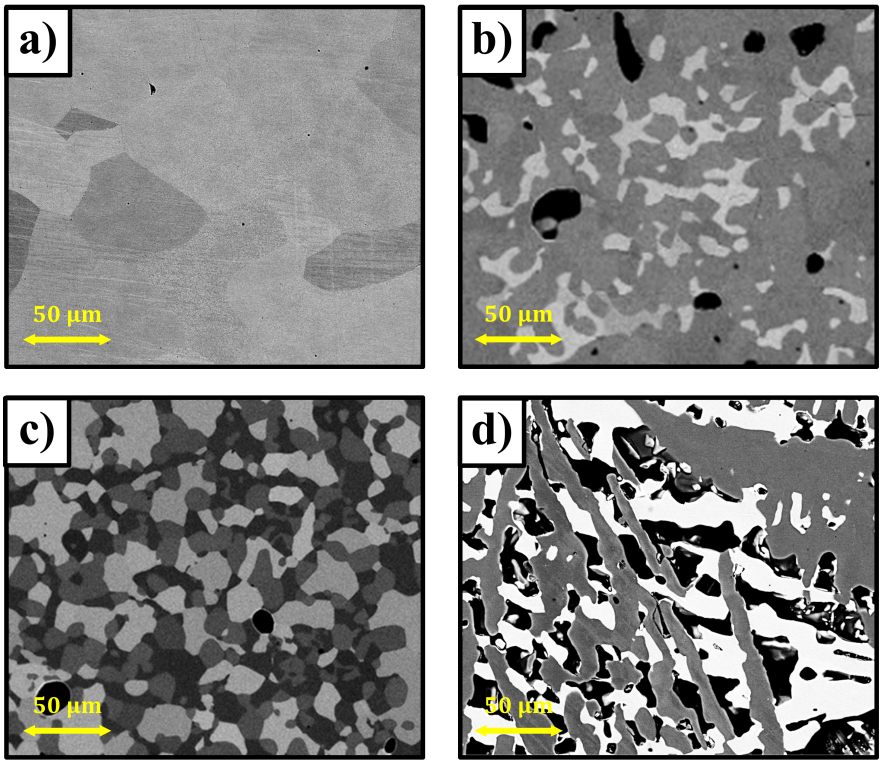

Figure 6.9: SEM (BSE) images of arc melted microstructures of a) Alloy 1 b) Alloy 2 c) Alloy 3 d) Alloy 4 as defined in Table 6.2.

Alloy 2 is also predicted to be entirely BCC, but lies just at the portion of the gradient where the BCT phase (Al3Ti) is predicted to appear. At 950 °C, Thermo-Calc's TCHEA2 database predicts this alloy to produce two BCC phases: one with a composition of approximately 9Fe-1Ni-24Cr-14Ti-52Al [at%] at 37% molar fraction and another with a composition of 21Fe-13Ni-5Cr-2Ti-59Al [at%] at 63% molar fraction. Figure 6.9b shows the SEM imaged microstructure of the arc melted sample for this alloy. The darkest portions of the image are actually pores induced during melting. The other two shades indicate two distinct phases that were present after heat treatment. Energy-dispersive X-ray spectroscopy (EDS) was used to measure the composition of each phase in these images. The lighter phase was measured to have a composition of approximately 19Fe-10Ni-13Cr-2Ti-56Al [at%] and the darker phase was found to have a composition of 13Fe-7Ni-

4Cr-17Ti-58Al [at%]. XRD phase analysis showed some agreement with BCC peaks and slightly better agreement with the BCT structure, which is common for Al_3X intermetallics. These results do not exactly agree with the predicted phases, but the presence of two phases is promising and more investigation is required.

The third alloy was chosen because it is predicted to produce equal fractions of BCC and BCT phase. CALPHAD predicts three phases to form in Alloy 3 at 950°C: a BCT phase with a composition of 7Cr-19Ti-74Al [at%], a BCC phase with a composition of 21Fe-12Ni-5Cr-2Ti-60Al [at%], and a small fraction of a second BCC phase with a composition of 9Fe-1Ni-24Cr-12Ti-54Al [at%]. The microstructure shown in Fig. 6.9c also shows three phases. The composition of each phase, from lightest to darkest, was estimated to be 19Fe-13Ni-9Cr-1Ti-59Al [at%], 14Fe-1Ni-20Cr-2Ti-64Al [at%], and 12Fe-7Ni-5Cr-16Ti-59Al [at%]. These compositions align relatively well with the predicted majority BCC phase, the minority BCC phase, and the BCT phase respectively.

The last alloy, Alloy 4, was selected because it is predicted to produce 25% BCC phase and 75% BCT phase and the remaining gradient compositions between Alloy 4 and pure aluminum lie primarily in the Al-Ti binary, which is well understood. At 950 °C, the BCC phase is predicted to have a composition of 24Fe-12Ni-2Cr-1Ti-60Al [at%] while the prediction for the BCT phase is 3Cr-22Ti-75Al [at%]. Figure 6.9d shows the microstructure of the Alloy 4 sample. As in Fig. 6.9b, the darkest regions depict pores. The microstructure seems severely striated with elongated grains and many pores. ESD compositional analysis estimated the composition of the lightest phase to be 16Fe-4Ni-5Cr-3Ti-72Al [at%] and that of the darker phase to be 2Cr-23Ti-75Al [at%], which also aligns relatively well with predictions.

The phases and microstructure of the arc melted samples seemed to largely agree with CALPHAD predictions. The number of present phases was always predicted accurately and their proportions qualitatively agree. The compositions of some phases, particularly those in Alloy 2, did not agree well, but XRD peaks had good agreement with either BCC or BCT phases for all samples.

6.2.6.2 Attempted Printing of Partial Gradient

In order to print the planned gradient in the laboratory's Optomec LENS® MR-7 DED system, it needed to be printable with four powders as only the machine only has four powder feeders. Fortunately, the simplified gradient path in Fig. 6.7a has a near fixed ration of Ni to Cr, which allows for the premixing of a Ni-Cr blend mixed at 3:4 molar ratio. The four powders used were the mixed Ni-Cr powder, pure Fe powder, pure Ti powder, and Al 6061 powder.

Before printing the gradient, considerable work was done to determine the optimal process parameters for the steel and aluminum sides of the gradient. Because aluminum has a much higher reflectivity and thermal conductivity as well as a lower density, process parameters like laser power and speed need to be modified significantly from those for steel. Rectangular builds of just steel and aluminum were both attempted to optimize the processing parameters. Unfortunately, the best processing parameters found for aluminum still resulted in significant defects like insufficient melting, gas entrapment, and oxidation. Aluminum is notoriously difficult to print via additive manufacturing, with Al-10Si-Mg being the only aluminum alloy with widespread use [70].

For these reasons, only a partial portion of the gradient was printed to approximately 60 wt.% aluminum, until defects prevented further addition of aluminum. The process parameters for steel were used until about 30 wt.% aluminum, from which point the aluminum process parameters were used. Significant pore formation and oxidation was observed during the build, but no catastrophic cracking was observed. Wavelength Dispersive X-Ray Spectroscopy (WDS) was used to measure the composition along the gradient and substantial deviations from the target compositions were observed, particularly in Al-rich regions, which could be attributed to suboptimal process parameters.

These results exemplify just how difficult a gradient from steel to aluminum is to achieve with current additive manufacturing technologies. Due to drastic changes in material properties, process parameters need to be changed nearly continuously to prevent defects. Furthermore, the high reflectivity and conductivity of Al-rich compositions complicate their manufacturability via additive methods. As technologies develop and new methods for printing aluminum are discovered, future

attempts at achieving a successful gradient can be made. Although, new elements, constraints, or properties might need to be included in the gradient design problem description if the methodology is to find a feasible path.

6.3 Chapter Summary

Gradient design problems can easily become over-constrained in complex state spaces with many deleterious phases or manufacturing complications. Treating all constraints as hard obstacles in these spaces can restrict the free space to narrow passages between obstacles which can impede an algorithm's ability to plan feasible paths, if any even exist. Considering some constraints as soft constraints in a penalty cost term can alleviate some of these difficulties by minimizing constraint violation.

A gradient design problem from steel to aluminum was chosen to demonstrate the effectiveness of minimizing constraint violation because of the abundance of deleterious intermetallics. The state space of the design problem was five-dimensional as titanium was included to exploit the favorable intermetallic Al3Ti and temperature was added to plan for differences in melting temperature. Considering all deleterious phases as hard constraints leaves very little room in the Al-rich portion of the state space. A penalty cost term was formulated with a limit towards infinity as the predicted phase fraction of aluminum intermetallics increases. Using this term to minimize intermetallic phases and setting hard constraints on other deleterious phases leaves about half of the Al-rich state space available for path planning.

The optimal path found by the path planning algorithm dramatically reduced the predicted phase fraction of intermetallics as compared to the linear gradient and all other deleterious phases were successfully avoided. Manually simplifying the path by slightly reducing Al and Fe compositions near Al3Ti and linearizing elsewhere saw a reduction of intermetallic phases to near zero. The algorithm might not have discovered the more optimal, simplified gradient because the cost function was ill-formed or not enough iterations were taken. The cost function could be improved by considering a non-additive term, like the maximum intermetallic fraction of a total path, or by improving the regression model for intermetallic phase fractions. The balance between path length

and intermetallic fraction in the cost function could also be explored.

Experiments were conducted in an attempt to validate some characteristics of the planned gradient. First, four compositions from the simplified gradient were selected for arc melting to examine their phases and verify predicted phase fractions. The arc melted samples generally agreed with the number and structure of the predicted phases, but some discrepancies were observed in phase composition, particularly at the onset of the BCT phase. An attempt was made to print the full gradient from steel to aluminum, but large changes in material properties produced many defects in the Al-rich portion of the gradient. Although two sets of process parameters were optimized, a continuous change in processing might produce better results. Novel techniques or compositions for printing aluminum alloys are also necessary to overcome the challenges induced by aluminum's high reflectivity and conductivity. Future design problems that incorporate processing parameters or manufacturing challenges might be solvable by the presented methodology to produce paths that address these issues.

7. OPTIMIZING FOR PROPERTIES: PROPERTY MONOTONICITY*

The primary benefit of compositionally graded alloys is the gradients they provide in properties. However, the gradient regions of these materials often exhibit worse properties than either end material and can diminish the potential usefulness of the gradient. This chapter presents a novel cost function for gradient design that optimizes gradient paths for properties. The fundamental concept of the cost function is the value of monotonic property gradients. The properties of monotonic gradients are guaranteed to be no worse than the end materials and can be transformed by controlling deposition rate. This ability to transform means such gradients can be used as fundamental recipe to achieve any bounded change in properties across a material. The cost function is first demonstrated in a synthetic case study to visualize trade-offs between length and property monotonicity. The cost function is then applied to a real material system to show how it can be used to minimize stresses induced by differences in thermal expansion.

7.1 Property Monotonicity as a Design Objective

Functionally Graded Materials, including compositionally graded alloys, are desired primarily for the gradients they produce in properties and therefore function [7, 10, 13]. As such, the consideration of properties should be a primary component of FGM design. Even properties that are not directly relevant to performance can be critical to manufacturability and part integrity. One such property is the Coefficient of Thermal Expansion (CTE), which often varies dramatically with composition in alloys. In fact, large discontinuities in CTE are often present at phase boundaries in gradient materials. During the high-temperature additive manufacturing process, FGMs experience large thermal gradients. Consequently, these discontinuities in CTE often lead to cracking during manufacturing [61, 62].

The compositional path that minimizes the stresses induced by property gradients is one that

*Contains material reprinted with permission from T. Kirk, R. Malak, and R. Arróyave. "Computational Design of Compositionally Graded Alloys for Property Monotonicity." *Journal of Mechanical Design.* 143, no.3 (March 2021) [6].

minimizes the property gradients themselves. Let y represent the position in physical space along a gradient part and $p(z)$ represent some property of interest that is a function of material composition (e.g. CTE). If the local change in the property p along the physical part, $\frac{\mathrm{d}p}{\mathrm{d}y}$, is too large, then significant stress gradients can form. Therefore, the gradient path that minimizes property-induced stresses is that which minimizes $\frac{\mathrm{d}p}{\mathrm{d}y}$. The maximum property gradient $\frac{\mathrm{d}p}{\mathrm{d}y}$ along a part, and consequently the maximum induced stress, is minimized when the property is graded linearly along the part and $\frac{\mathrm{d}p}{\mathrm{d}y}$ is constant everywhere. However, it is unlikely that there exists a compositional gradient path $\sigma(\alpha)$ for which an arbitrary property varies linearly as a function of path index α and $\frac{\mathrm{d}p}{\mathrm{d}\alpha}$ is constant.

Fortunately, the rate at which the compositional gradient is deposited on the physical part is an accessible design parameter that can be varied during the build. Consider $\frac{\mathrm{d}\alpha}{\mathrm{d}y}$ to be the local change in path index per unit length along a gradient part (i.e. per build layer). Because path index scales proportionally with length in composition space (Eq. 2.1) and each path index directly corresponds to a specific material composition, this rate is analogous to deposition rate: the rate that material composition is changing per unit length along a gradient part. This rate can be approximated by measuring the composition of two adjacent layers in a gradient part and dividing the difference in the associated path indices by the layer thickness. Controlling this deposition rate could allow designers to vary properties linearly along the dimensions of the part even if the property does not vary linearly with composition or path index. For example, due to the relationship shown in Eqn. 7.1, one could achieve a constant $\frac{\mathrm{d}p}{\mathrm{d}y}$ by adjusting $\frac{\mathrm{d}\alpha}{\mathrm{d}y}$ in inverse proportion with $\frac{\mathrm{d}p}{\mathrm{d}\alpha}$ as α increases from 0 to 1.

$$\frac{\mathrm{d}p}{\mathrm{d}y} = \frac{\mathrm{d}p}{\mathrm{d}\alpha}\left(\frac{\mathrm{d}\alpha}{\mathrm{d}y}\right) \tag{7.1}$$

However, this is only possible if the condition shown in Eqn. 7.2 is true, where $\Delta p_{\text{total}} = p(z_{\text{goal}}) - p(z_{\text{init}})$.

$$\operatorname{sgn}\left(\frac{\mathrm{d}p}{\mathrm{d}\alpha}\right) = \operatorname{sgn}(\Delta p_{\text{total}}) \,\forall\, \alpha \in [0, 1] \tag{7.2}$$

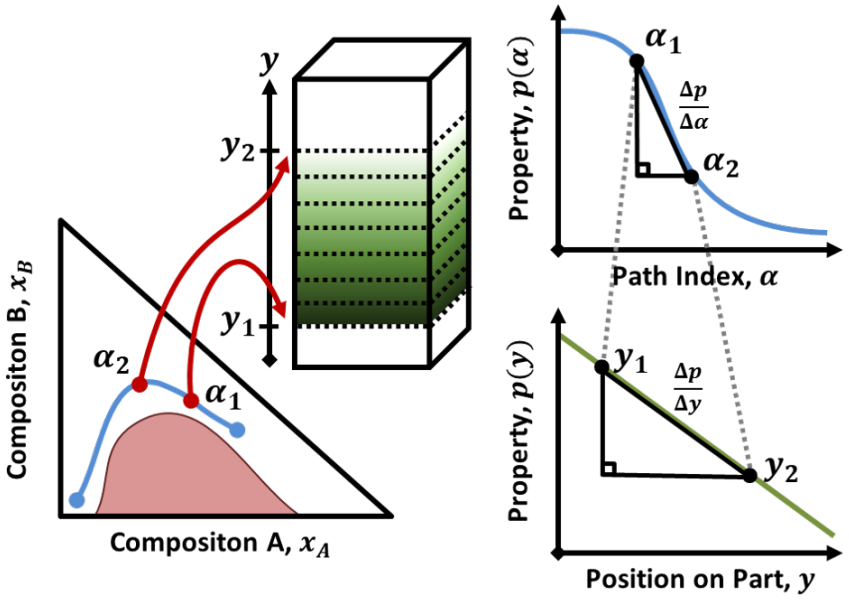

Figure 7.1: An example of how a pathwise property profile, $p(\alpha)$, that is monotonic with path index, α, can be made to vary linearly with position on a part, y. Note that the region where $\frac{\mathrm{d}p}{\mathrm{d}\alpha}$ is highest occupies the largest region of the part. This is where deposition rate, $\frac{\mathrm{d}\alpha}{\mathrm{d}y}$, must be slowest to achieve a constant $\frac{\mathrm{d}p}{\mathrm{d}y}$. Reprinted with permission from Kirk et al. (2021) [6].

This condition mandates that properties vary *monotonically* along the compositional gradient path, meaning they either always decrease or always increase with path index, α. It also suggests that any property that is monotonic with path index can be mapped into a linear property gradient on the physical part by controlling material deposition rate, subject to the maximum and minimum achievable deposition rates. This process is depicted visually in Fig. 7.1.

Pathwise property profiles, $p(\alpha)$, that are monotonic with path index can not only be transformed to be linear along a part, they can also be mapped into any partwise property profile, $p(y)$, that is monotonic with y. Furthermore, as illustrated in Fig. 7.2, pathwise property profiles that are monotonic with path index can even be transformed to vary non-monotonically along a part, given that the non-monotonic part profile is still bounded by the property values at z_{init} and z_{goal}. This capability means that a pathwise property profile, $p(\alpha)$, that is monotonic with path index can be mapped into nearly any properly bounded partwise profile, $p(y)$. This characteristic is critical to

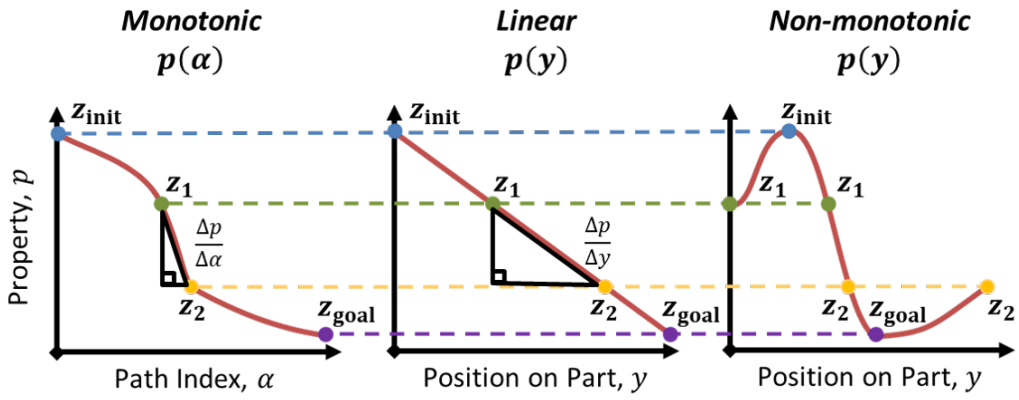

Figure 7.2: Visualizations of how a pathwise property profile, $p(\alpha)$, that is monotonic with path index can be mapped into a linear partwise property profile, $p(y)$, or, more generally, an arbitrary non-monotonic partwise property profile, $p(y)$, that is bounded by $p(z_{\text{init}})$ and $p(z_{\text{goal}})$. Reprinted with permission from Kirk et al. (2021) [6].

the design of functionally graded parts. If a designer knows the desired maximum and minimum properties of a part, a material gradient with monotonic properties between those extrema can be used as a kind of "designer's palette" of materials with which any spatial distribution of properties within the part can be created, subject to machine deposition rates.

To determine the deposition plan needed to achieve a desired partwise property profile, one need only manipulate the relationship shown in Eqn. 7.1. In practice, the deposition of a gradient path might be designed such that practical constraints on the maximum property gradient $\left|\frac{\mathrm{d}p}{\mathrm{d}y}\right|_{\max}$ and maximum deposition rate $\left|\frac{\mathrm{d}\alpha}{\mathrm{d}y}\right|_{\max}$ are satisfied. Equation 7.3 provides a method for determining the deposition plan for a gradient path subject to these constraints. Given the function $p(\alpha)$ that describes the change in the relevant property as a function of path index, one can divide the path in to segments where $p(\alpha)$ is approximately linear. For an arbitrary segment between α_i and α_{i+1}, Eqn. 7.3 describes the minimum length of the gradient part (i.e. the minimum number of layers) needed to print that segment of the gradient path, $\Delta y_{i\to i+1,\min}$.

$$\Delta y_{i\to i+1,\min} = \mathbf{max}\left\{|\alpha_{i+1}-\alpha_i|\left|\frac{\mathrm{d}\alpha}{\mathrm{d}y}\right|_{\max}^{-1}, \left|p(\alpha_{i+1})-p(\alpha_i)\right|\left|\frac{\mathrm{d}p}{\mathrm{d}y}\right|_{\max}^{-1}\right\} \tag{7.3}$$

Equation 7.3 can be calculated for each segment of the path to construct a piecewise linear deposition plan $y(\alpha)$, as shown in Eqn. 7.4, for which every position or layer on a gradient part has an associated path index and therefore material composition.

$$y(\alpha_{i+1}) = y(\alpha_i) + \Delta y_{i \to i+1,\text{min}} \tag{7.4}$$

By controlling deposition rates, gradient paths with monotonic property profiles can be mapped onto a part to achieve practically any spatial distribution of properties a designer might desire, subject to machine limitations. Therefore, to find a compositional gradient path that will provide a desired partwise property profile one need only find a path with properties that vary monotonically with path index. All feasible compositional gradient paths with monotonic property profiles offer this same design freedom and are therefore roughly equivalent in designer preference. Because non-monotonic profiles do not offer this freedom, all paths with monotonic profiles are preferred to those with non-monotonic profiles.

7.2 Lack of Monotonicity

To introduce the ability to find gradient paths with monotonic properties into the current FGM design methodology, a cost function is needed that prioritizes such paths. Davydov and Zitikis [132] have developed a metric to quantify the degree of non-monotonicity possessed by a non-monotonic function. This metric, Lack of Monotonicity (LOM), relies on the calculation of two additional quantities: Lack of Increase (LOI) and Lack of Decrease (LOD).

To calculate the Lack of Increase of a general continuous function g_0 over the interval $[a, b]$ one must integrate the negative part of the first derivative of g_0 over the Lebesgue measure, λ, as seen in Eqn. 7.5 where $\left(g_0'\right)^- = \max\{-g_0', 0\}$. Note that if g_0 is monotonically increasing over the interval $[a, b]$, then $\text{LOI}_{[a,b]}(g_0) = 0$.

$$\text{LOI}_{[a,b]}(g_0) = \int_a^b \left(g_0'\right)^- \text{d}\lambda \tag{7.5}$$

Lack of Decrease is calculated similarly by integrating the *positive* part of the first derivative

of g_0, as seen in Eqn. 7.6 where $\left(g_0'\right)^+ = \max\{g_0', 0\}$.

$$\text{LOD}_{[a,b]}(g_0) = \int_a^b \left(g_0'\right)^+ \mathrm{d}\lambda \tag{7.6}$$

Finally, the Lack of Monotonicity of g_0 over the interval $[a, b]$ is shown in Eqn. 7.7.

$$\text{LOM}_{[a,b]}(g_0) = 2\textbf{min}\big\{\text{LOI}_{[a,b]}(g_0), \text{LOD}_{[a,b]}(g_0)\big\} \tag{7.7}$$

7.3 Cost Function: Minimize Property Non-Monotonicity

These metrics can be used to assess the lack of monotonicity in a pathwise property profile and consequently drive the FGM design methodology towards gradient paths with monotonic properties. The LOI and LOD of the property profile, $p(\alpha)$, for a given path, σ, can be calculated from Eqns. 7.8 and 7.9 respectively.

$$\text{LOI}_\sigma(p) = \int_0^1 \left(\frac{\mathrm{d}p}{\mathrm{d}\alpha}\right)^- \mathrm{d}\alpha \tag{7.8}$$

$$\text{LOD}_\sigma(p) = \int_0^1 \left(\frac{\mathrm{d}p}{\mathrm{d}\alpha}\right)^+ \mathrm{d}\alpha \tag{7.9}$$

To implement these metrics into the current methodology they must be formulated into a compatible cost function. RRT*FN [3] and many other tree- or map-based planners store segment costs independently and then sum the costs of each segment in a path to compute the total path cost. As such, a compatible cost function must be *additive*, satisfying the condition that $c(\sigma_1|\sigma_2) = c(\sigma_1) + c(\sigma_2)$ for all $\sigma_1, \sigma_2 \in \Sigma$. This condition is incompatible with LOM because, as shown in Eqn. 7.7, LOI and LOD must be evaluated for the total path before selecting which is the minimum quantity. For example, a path σ_1 with strictly increasing properties would have $\text{LOM}_{\sigma_1} = 0$ and a path σ_2 with strictly decreasing properties would have $\text{LOM}_{\sigma_2} = 0$, but their concatenated path would have $\text{LOM}_{(\sigma_1|\sigma_2)} \neq 0$.

To remedy this issue, the change in properties between the initial and goal compositions can

be evaluated and then either LOI or LOD could be used alone in place of LOM. For example, if $\Delta p_{\text{total}} > 0$ (i.e. $p(z_{\text{init}}) < p(z_{\text{goal}})$), any monotonic profile between $p_(z_{\text{init}})$ and $p_(z_{\text{goal}})$ must be non-decreasing. In this case, LOI will measure the deviation from a monotonic property profile because all monotonic profiles must be non-decreasing (i.e. LOI $= 0$), while all non-monotonic profiles must increase somewhere (i.e. LOI > 0). Similarly, if $\Delta p_{\text{total}} > 0$ (i.e. $p(z_{\text{init}}) > p(z_{\text{goal}})$), LOD will measure the deviation from all monotonic profiles, which are all non-increasing.

As reviewed previously, in order for a cost function to ensure asymptotic optimality with an optimal sampling-based planner like PRM*, RRT*, or RRT*FN it must be strictly positive, monotonic, and bounded [91, 3]. Both LOI and LOD are bounded by $\int_a^b \left|g_0'\right| d\lambda$ [132] and monotonic for concatenated paths, but neither are strictly positive. This is because $\text{LOI}_\sigma(p) = 0$ and $\text{LOD}_\sigma(p) = 0$ for non-decreasing and non-increasing property profiles respectively. As such, there is no way for LOI or LOD to discriminate between monotonic property profiles.

However, by including path length (i.e. the Euclidean distance traversed by the path in composition space) into the cost function with LOI or LOD, shorter monotonic paths will become preferred to longer ones. Also, the cost function itself becomes strictly positive as path length is strictly positive and both LOI and LOD are non-negative. Designers can diminish the effect of path length in the cost function by introducing a weighting parameter, w, with very low magnitude. Such a parameter could effectively ensure path length is an active objective only when LOI or LOD are zero. A study on the magnitude of this parameter is presented later in this work.

Equation 7.10 presents a cost function that satisfies all the aforementioned criteria. As such, it can be easily implemented into the current methodology to obtain gradient paths with monotonic property profiles.

$$c(\sigma) = \begin{cases} \text{LOI}_\sigma(p) + wl & \text{if } \Delta p_{\text{total}} > 0 \\ \text{LOD}_\sigma(p) + wl & \text{if } \Delta p_{\text{total}} < 0 \end{cases} \tag{7.10}$$

7.4 Synthetic Case Study: Testing the Effect of Cost Function Weighting

The cost function shown in Eq. 7.10 was designed to seek the shortest gradient path with a monotonic property profile. A simple synthetic case study was created to test the ability of the cost function to find such paths. The case study was also used to examine the effect of the parameter w on the cost function's tendency to balance length and lack of monotonicity.

7.4.1 Problem Description

An artificial property model was generated for a two-dimensional input space, $x_1, x_2 \in [0, 1]$. The property model was created to have non-monotonic regions, but still enable monotonic paths from $z_{\text{init}} = (1, 1)$ to $z_{\text{goal}} = (0, 0)$. This model, $p(x_1, x_2)$, was created from an initial planar surface rotated along the line $x_1 + x_2 = 1$ to be monotonic with both x_1 and x_2. A non-monotonic region was created on the planar surface by modelling a semi-ellipsoid on the surface of the plane that was oriented normal to the plane with a major axis parallel to the line $x_1 + x_2 = 1$. The semi-ellipsoid was sized to be small enough to allow for monotonic paths from $z_{\text{init}} = (1, 1)$ to $z_{\text{goal}} = (0, 0)$, but large enough to make the straight-line, shortest length path non-monotonic. The final model has values ranging from approximately 0.3 to 0.7 for $x_1, x_2 \in [0, 1]$. Figure 7.3 illustrates the surface of the synthetic property model.

To test the cost function presented in Eq. 7.10, the path planning algorithm, RRT*FN, was used to plan several paths in x_1 and x_2 from $z_{\text{init}} = (1, 1)$ to $z_{\text{goal}} = (0, 0)$. For simplicity, no obstacle region was considered. Because the synthetic property model has a lower value at z_{goal} than z_{init}, Lack of Decrease (LOD) was used to measure non-monotonicity. Each of the seven runs of the path planning algorithm used a different value of the parameter w in the cost function, increasing in magnitude from 10^{-6} to 1. As such, each run had a different weighting between lack of decrease and path length. Each run of RRT*FN generated 5000 random samples with the same random seed, meaning each run used the same points to generate a tree and find an optimal path.

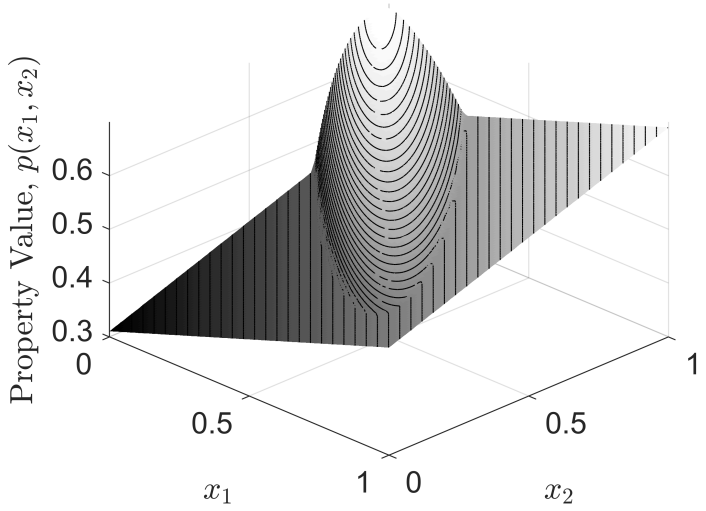

Figure 7.3: Surface of sythentic property model, $p(x_1, x_2)$, in x_1 and x_2 dimensions. The surface is generally monotonic with x_1 and x_2 except for the non-monotonic region formed by the semi-ellipsoid. Reprinted with permission from Kirk et al. (2021) [6].

7.4.2 Results and Discussion

The paths planned by each run of RRT*FN are shown in Fig. 7.4 and their respective pathwise property profiles are shown in Fig. 7.5. The values of each term in the cost function for the optimal paths in each run are listed in Table 7.1. When the weighting parameter is very small ($w \leq 10^{-3}$), the cost function seems to perform as intended and prioritize monotonicity before path length. In fact, the paths produced when $w = 10^{-6}, 10^{-5}, 10^{-4},$ and 10^{-3} are exactly the same and resemble the desired path: the shortest monotonic path between z_{init} and z_{goal}. As w increases to 10^{-2} and 10^{-1}, the paths become slightly shorter by encroaching into the ellipsoidal region, but also produce non-monotonic property profiles ($\text{LOD}_\sigma(p) > 0$). When w is further increased to 1, the length term in the cost function completely dominates and the path produced is the straight-line, shortest length path between z_{init} and z_{goal}.

In practice, w should be set as low as possible to make minimizing length a secondary objective to promoting monotonicity. However, these results indicate that a value of $w \leq 10^{-3}$ should produce the desired behavior for similarly scaled problems. All composition spaces are bounded

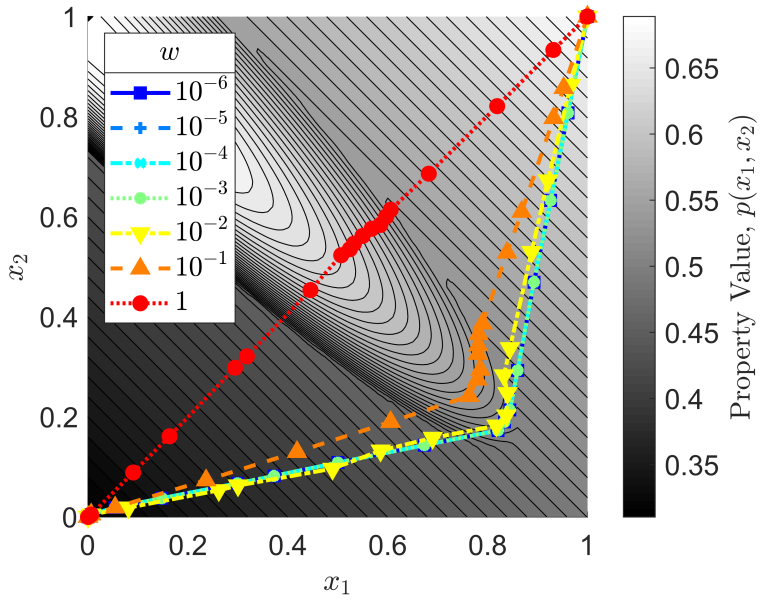

Figure 7.4: Paths planned from $z_{\text{init}} = (1, 1)$ to $z_{\text{goal}} = (0, 0)$ to examine the effect of the weighting parameter w in the proposed cost function, seen in Eq. 7.10. Note that the paths corresponding to $w = 10^{-6}, 10^{-5}, 10^{-4},$ and 10^{-3} are exactly the same. Reprinted with permission from Kirk et al. (2021) [6].

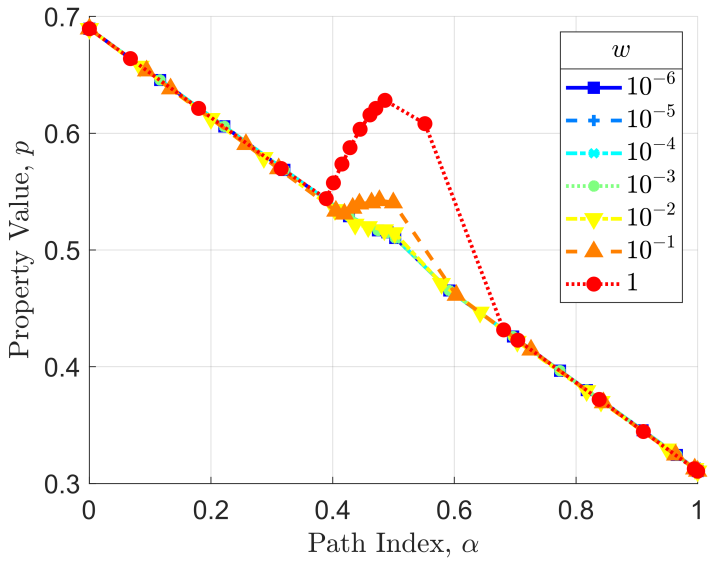

Figure 7.5: The value of the synthetic property, $p(x_1, x_2)$, along each planned path. Note that the property profiles where $w = 10^{-6}, 10^{-5}, 10^{-4},$ and 10^{-3} are identical. Reprinted with permission from Kirk et al. (2021) [6].

Table 7.1: Values of cost function terms for optimal paths in synthetic case study

w	l	$\text{LOD}_\sigma(p)$	$c(\sigma)$ (Eqn. 7.10)
10^{-6}	1.6882	0	1.6882×10^{-6}
10^{-5}	1.6882	0	1.6882×10^{-5}
10^{-4}	1.6882	0	1.6882×10^{-4}
10^{-3}	1.6882	0	1.6882×10^{-3}
10^{-2}	1.6841	1.6223×10^{-5}	1.6857×10^{-2}
10^{-1}	1.5995	6.3248×10^{-3}	1.6627×10^{-1}
1	1.4164	4.4215×10^{-2}	1.4606

by 0 and 1, so most FGM design problems should be of similar scale if the property model is scaled to have bounds near 0 and 1.

7.5 Case Study: Fe-Co-Cr System

A second case study was conducted to examine the performance of the proposed cost function in a realistic FGM design problem. Specifically, a compositionally graded alloy was designed with a monotonic gradient in Coefficient of Thermal Expansion (CTE). As discussed earlier, steep gradients in CTE can often lead to detrimental stress gradients during the additive manufacturing process [61, 62] and are therefore of critical importance to all compositionally graded alloys.

7.5.1 Problem Description

The iron-cobalt-chromium (Fe-Co-Cr) ternary system was chosen for this case study because it is easily visualized in two dimensions and has significant relevance to many engineering materials. It is important to note that the methodology can be applied to a higher dimensional system with more elements, but a simpler system was chosen to visualize how optimal paths navigate the space. The end points of the designed gradient path, z_{init} and z_{goal}, were chosen to be Fe95Co5 [at%] and Fe10Co60Cr30 [at%], respectively. The initial point, Fe95Co5 [at%], is representative of many steels including high speed steels used in cutting tools for their high temperature resistance and hardness [133]. The goal point, Fe10Co60Cr30 [at%], represents cobalt-chrome alloys which exhibit exceptional corrosion, wear and thermal resistance as well as high specific strength and

are often used in biomedical applications [134]. A gradient between these two materials could conceivably be employed in a surgical device or a device with significant thermal requirements like a drill or turbine.

To apply the FGM design methodology to this system, phase regions were first modeled with CALPHAD software, specifically Thermo-Calc's TCHEA2 database [110, 111]. The CALPHAD model was sampled 1275 times in a regular grid throughout the Fe-Co-Cr composition space. Phase equilibria were calculated at a temperature of 1000 K, which was chosen to approximate the temperature of the manufacturing process. Sigma (σ) phase was chosen as an undesirable phase due to its detrimental mechanical properties including high brittleness [117, 118]. A surrogate obstacle model was created by labeling the samples with greater than one percent mole fraction of sigma phase and then training a k-nearest neighbors ($k = 3$) classifier to represent the sigma phase region.

Thermo-Calc's TCHEA2 can also predict Coefficients of Thermal Expansion (CTE) for any composition in its database [111]. This capability was leveraged to gather predictions of CTE at 1000 K at the same 1275 compositions that were sampled for phase information. The CTE data was made to lie within $1 \times 10^{-6} K^{-1}$ and $1 \times 10^{-4} K^{-1}$ by rounding outlying data to the bounds and was then scaled to range from 0 to 1. An interpolant model was then created from the data that linearly interpolates between the data to predict CTE at any composition in the Fe-Co-Cr composition space.

Given a model of the obstacle region and a model of the relevant property, the path planning algorithm, RRT*FN [3], was used to plan paths for two different cost functions. The first cost function was simply path length and was planned to assess the properties of a path planned without any consideration of optimal properties. The second cost function was that proposed in Eqn. 7.10, which seeks to find the shortest path with monotonic properties. Because the CTE at z_{init} is greater than that at z_{goal}, $LOD_{\sigma}(p)$ was chosen to measure non-monotonicity. As in the synthetic case study, the random seed was fixed for both cases so the same 5000 nodes were used to construct the tree and find the optimal path.

7.5.2 Planned Gradients

The paths found to optimize each cost function are displayed in Fig. 7.6 and the value of CTE along each path is shown in Fig. 7.7. The path planned for the first cost function, $c(\sigma) = l$, resembles the straight-line path between z_{init} and z_{goal}. While this is the shortest feasible path, it experiences a large increase in CTE as it approaches z_{goal}, as seen in Fig. 7.7. This makes the property profile significantly non-monotonic. The second cost function however, succeeds in producing the shortest path with a monotonic CTE profile.

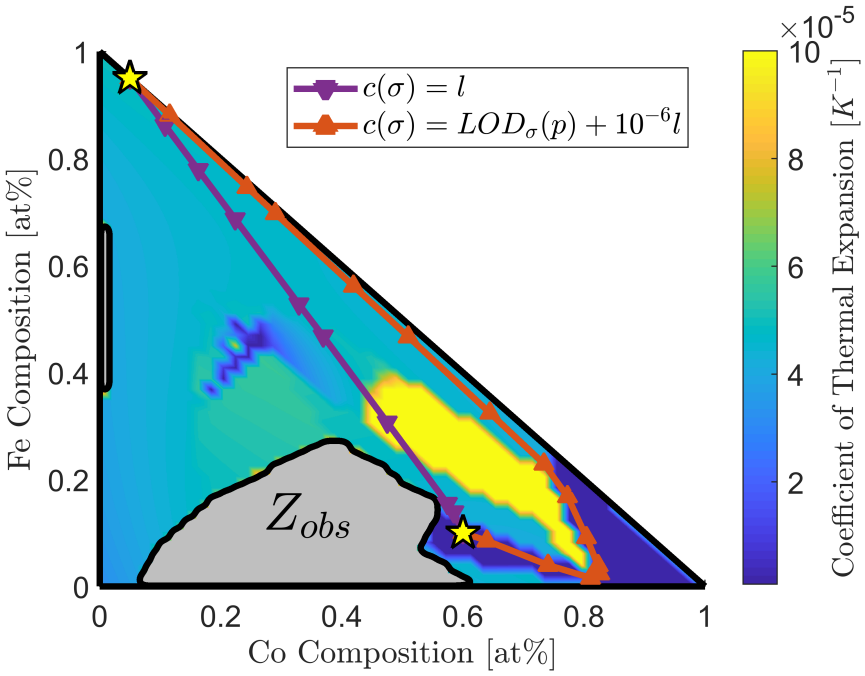

Figure 7.6: Paths planned by RRT*FN to be optimal with respect to two cost functions: one intended to find the shortest path and the other to find the shortest path that has a monotonic CTE profile. The obstacle region (Z_{obs}) and the values of CTE throughout the composition space are also plotted. Cr composition can be inferred as the remainder (pure Cr located at the origin). Reprinted with permission from Kirk et al. (2021) [6].

While the path planned with the proposed cost function is monotonic, Fig. 7.7 does show a sharp decrease in CTE. However, the shortest length path also experiences a similar drop in CTE.

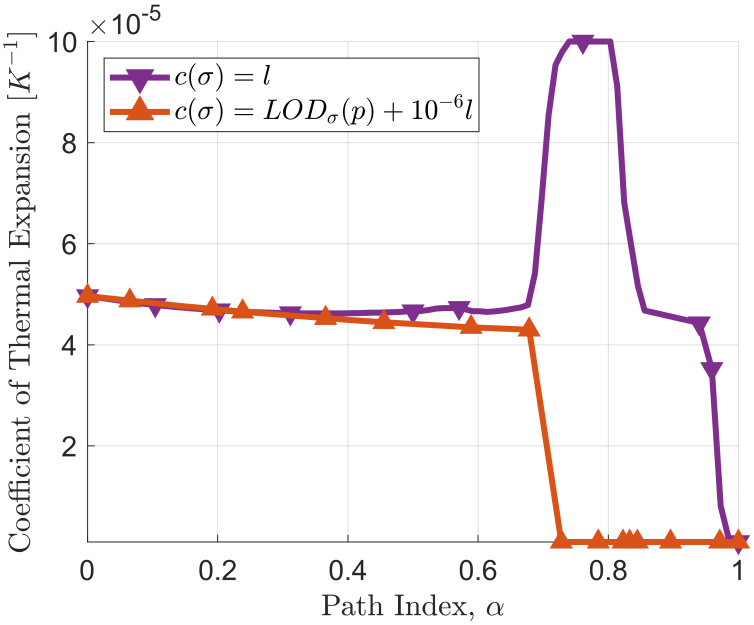

Figure 7.7: The CTE profiles along both optimal paths. Reprinted with permission from Kirk et al. (2021) [6].

In fact, by examining the CTE contours in Fig. 7.6, it appears that such a drop is unavoidable as every feasible path to z_{goal} would experience a steep decrease in CTE. Fortunately, these steep regions can be mitigated by decreasing the deposition rate in these regions. Although the first path is shorter, it has more steep changes in CTE and might actually need more layers to print due to the need to decrease deposition rates in steep regions. In addition to potentially requiring less layers to print, a part made with the monotonic compositional gradient could be made to have nearly any properly bounded CTE profile, subject to machine limitations on deposition rate, as shown in Fig. 7.2.

7.5.3 Deposition Plan

To demonstrate how one could determine deposition rates, the deposition of the monotonic path was planned for a hypothetical part. While the path could be deposited so that the partwise property, $p(y)$, was linear, it would require extreme differences in the deposition rates because of the differences in $\frac{\mathrm{d}p}{\mathrm{d}\alpha}$ between the steep drop in CTE and the comparatively flat regions at the

beginning and end of the path, as seen in Fig. 7.7. This would lead to a relatively enormous region of the part dedicated to a small portion of the compositional gradient.

Instead, reasonable constraints for the partwise property gradient and deposition rate were used to determine the deposition plan. The position on the part, y, was measured in build layers for simplicity. The maximum property gradient on the part, $\left|\frac{\mathrm{d}p}{\mathrm{d}y}\right|_{\max}$, was chosen to be $4 \times 10^{-7}\mathrm{K}^{-1}$ per layer. The achievable change in composition per layer was estimated to be 1 atomic percent [at%]. This number was then divided by the total length of the path to estimate a maximum deposition rate $\left|\frac{\mathrm{d}\alpha}{\mathrm{d}y}\right|_{\max}$. These two constraints were then used with Eqn. 7.3 to determine how many layers should be used to print each segment of the path.

Figure 7.8 displays the resulting gradients of path index, α, and CTE along the planned gradient part. Note that there are three distinct regions where a different constraint was active. In the first part of the gradient, where $\frac{\mathrm{d}p}{\mathrm{d}\alpha}$ is small, the deposition rate is at its maximum. This is where the gradient is deposited as fast as possible because the associated property gradient $\frac{\mathrm{d}p}{\mathrm{d}y}$ is insignificant. Once the steep decline in CTE is reached, the deposition rate is slowed for about 100 layers so that the property gradient is at its maximum acceptable value, $\left|\frac{\mathrm{d}p}{\mathrm{d}y}\right|_{\max}$. After the steep change in CTE has been navigated, the deposition rate is once again maximized. The compositions of the corresponding part are shown in Fig. 7.9. From layers 100 to 200, where deposition rate is slowest, the compositions barely change. This is to diminish the effects of the steep property gradient, $\frac{\mathrm{d}p}{\mathrm{d}\alpha}$, seen in Fig. 7.7.

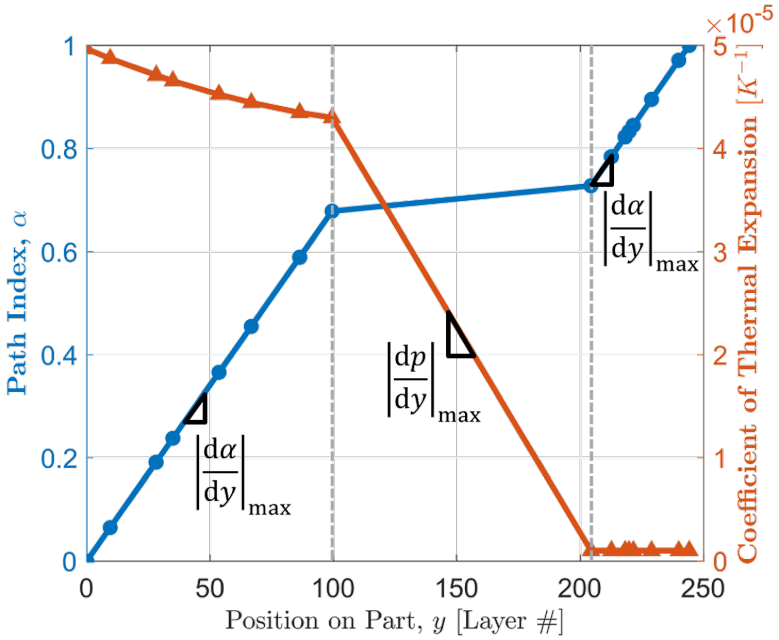

Figure 7.8: Path index and Coefficient of Thermal Expansion of the monotonic gradient path deposited along a hypothetical part. Note that there are three distinct regions where either maximum deposition rate or maximum property gradient is the active constraint, according to Eq. 7.3. Reprinted with permission from Kirk et al. (2021) [6].

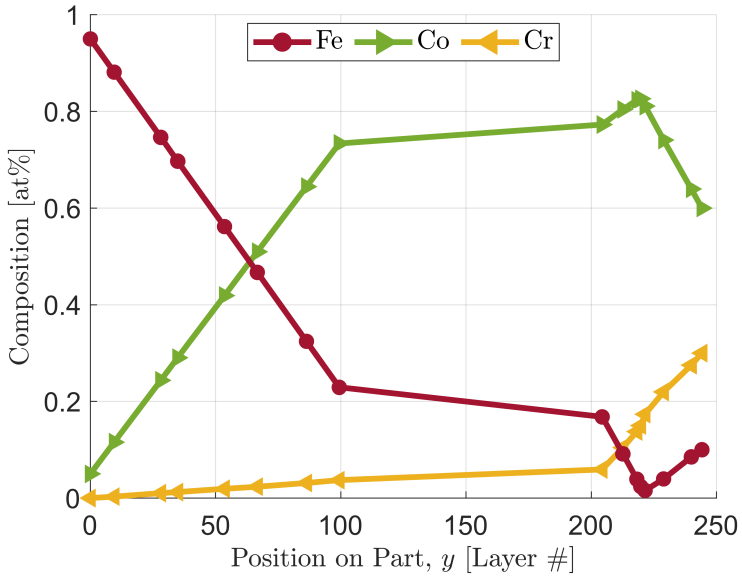

Figure 7.9: Compositions along the planned gradient part. Reprinted with permission from Kirk et al. (2021) [6].

7.6 Chapter Summary

A novel cost function was presented that optimizes gradient paths to have monotonic property profiles. By controlling material deposition rate, compositional paths with monotonic property profiles can be made into gradient parts with nearly any properly bounded spatial distribution of properties. Consequently, a material gradient with a monotonic change in properties can be used as a kind of "designer's palette" of materials, wherein a one-to-one correspondence of property to material can be exploited to design properties locally. Because of this design freedom, designing a single gradient with monotonic properties avoids the need to design a new material gradient for every property gradient a designer might desire.

When using a gradient with monotonic properties, controlling the spatial distribution of properties is simply a matter of controlling material deposition. In the Fe-Co-Cr case study, a straightforward, one-dimensional deposition strategy was employed to satisfy constraints on maximum deposition rate and maximum property gradient. However, more complex deposition strategies

can be easily designed to achieve desired property distributions by inverting the monotonic, and therefore one-to-one, material-property relationship. This enables the use of gradient alloys in optimal part design strategies, like topology optimization, that optimize local property distributions for global part performance.

8. SUMMARY OF CONTRIBUTIONS AND LIMITATIONS

8.1 Research Summary

Compositionally graded alloys are promising materials that enable many design opportunities through the spatial variation of properties. However, compositional gradients between metals are often difficult to achieve due to the presence of deleterious phases and the stringent material requirements of additive manufacturing. Current design methods struggle to overcome these issues because they rely solely on human intuition and visualization. This research presents a novel computational methodology for the design of compositionally graded alloys that can plan gradients in large, multi-component spaces, while ensuring gradients meet design requirements and optimizing them for user-defined objectives.

The first contribution of this research, that enabled the creation of a computational design methodology, is the formulation of gradient design as a path planning problem. This formulation enabled the use of algorithms from the motion planning or path planning community to solve gradient design problems in an efficient and consistent manner.

The methodology itself employs a sampling-based planner to construct a tree in state space of feasible paths. This path planning algorithm, RRT*FN [3], is more efficient than other algorithms because it minimizes the samples of the state space, but it still provides guarantees of probabilistic completeness and asymptotic optimality. The methodology can consider design intent in the formulation of both constraints and objectives as obstacles and cost functions, respectively. Modeling tools, like CALPHAD, can predict relevant quantities such as phase fractions and material properties, but surrogate models are needed to make models tractable for path planning.

A constraint formulation is given for the avoidance of deleterious phases that is compatible with the presented methodology. Phase fractions can be set by the user to avoid phases at a specific temperature, within a specified temperature range, or directly at solidification. Such constraints are demonstrated in an illustrative example in the Fe-Ni-Cr system. Multiple paths are planned

between steel and pure chromium that each avoid deleterious phases while minimizing path length or maximizing obstacle clearance. One planned gradient was manufactured and confirmed to avoid the brittle $CrNi_2$ and sigma phases.

Manufacturing metrics that can be represented in terms of state space, like solidification range and Hot Cracking Susceptibility, are also formulated as constraints. A gradient path between steel and pure tungsten is planned which utilizes these constraints to avoid issues brought about by large differences in melting temperatures. The planned gradient successfully satisfies constraints on both phases and manufacturing metrics, but unforeseen issues in the vaporization temperature of chromium prevented a successful build.

In the case of an over-constrained problem, a cost function is demonstrated that minimizes constraint violation. Such a cost function is used to plan a path between steel and aluminum in a five-dimensional state space. Intermetallics, which are prevalent in the Al-rich portion of the space, were successfully minimized in the optimal gradient by considering them in a penalty cost term. Experimental evidence confirmed the phase predictions, but manufacturing complications associated with aluminum prevented a full gradient build.

Lastly, a novel cost function is derived to optimize gradients for property monotonicity. Gradient alloys with monotonic property gradients can be used to achieve nearly any bounded property distribution in a gradient part. A synthetic case study is presented to illustrate the use of the cost function in a simple system and to explore the balance between path length and property monotonicity. The cost function is also demonstrated to design a compositionally graded alloy in the Fe-Co-Cr system with a monotonic change in Coefficient of Thermal Expansion.

8.2 Limitations and Future Work

While the proposed methodology offers many advantages over traditional design techniques, there are still many limitations that define the problems the methodology is suited for and the solutions it can provide. This section describes these limitations and also suggests future research directions to address them.

8.2.1 Path Planning Algorithm

8.2.1.1 Cost Functions

Using the optimal Rapidly-exploring Random Tree (RRT*) as the path planning algorithm imposes certain restrictions on the cost function, if the guarantee of asymptotic optimality is to be upheld. Compatible cost functions are described in Section 3.2.2.3 to be strictly positive, monotonic, and bounded. In addition, the current implementation of RRT*FN can only consider costs that are additive or stored per segment, but this is not a strict requirement to satisfy guarantees. The implementation can be changed to accommodate non-additive cost functions by changing the procedures for calculating and storing costs, but it could increase time or space complexity.

A simple, but prohibitive condition for cost functions is that they must be computable for any point in state space. As such, if properties are to be considered in the cost function, a property model must be provided that is valid for all of free space. This prohibits the inclusion of many material properties that are difficult to predict as a function of composition like ultimate strength, fatigue, etc. However, machine learning and experimental data can help bridge this gap by fitting regression models across composition space.

Another limitation of the methodology is that it has no defined stopping criteria. It is possible to know when the goal composition is reached, but it is not possible to know when the optimal path has reached the global optimum. Like in the optimization community, a convergence criterion can be applied to stop after a minimum iterative change in cost value, but this provides no guarantees of a global optimum. Similarly, it is not possible to know if a feasible path exists or to stop if none exists.

8.2.1.2 Constraints

The constraint formulations given in this dissertation rely on a definition of free space, Z_{free}. This means that constraints must be formulated in terms of the state space (e.g. composition and temperature). Other types of constraints, like those that depend on the total path, could be conceived, but might not be easily implemented into the current methodology if they cannot be

used to define an obstacle region in state space.

8.2.1.3 Sampling

While a sampling-based planner was determined to provide many benefits to solving the gradient design problem, random sampling has disadvantages to gradient design that might not be relevant to motion planning. One such disadvantage is the neglect of design space boundaries when generating potential paths. The motion planning analogy has no use for these boundaries as they typically represent walls or otherwise unnavigable space. However, in gradient design, the design space boundaries represent valid subspaces that could be used in the potential gradient. For example, the boundaries of a ternary space represent binary spaces, the boundaries of quaternary spaces represent ternaries, and so on. In fact, spaces with less elements often have less complex phase spaces and could be valuable pieces of the optimal solution, as seen with the Cr-W and Al-Ti binaries in Chapters 5 and 6 respectively.

One method of sampling the boundaries of the space is to artificially extend the boundaries of the sampling procedure. Those samples that are generated outside of the true boundaries can then projected onto them. Some heuristic parameter would be needed to define how far to extend the artificial boundary of the sampling and it would need to be carefully tuned so as to properly balance the number of samples generated on boundaries with the number of samples generated elsewhere in the space.

8.2.1.4 Multiple Queries

As with most engineering design problems, it is common to change the cost and constraint formulations of a gradient design problem as more information about the space or designer preferences is discovered. However, RRT* is a single-query algorithm. This means that a new tree needs to be made for every new definition of the constraints or the cost function. If the new formulations rely on the same model data (e.g. CALPHAD), then new model calculations might not be needed, but new surrogate models need to be trained on the obstacle definition. But the real expense of a new query lies in rerunning RRT*, as each of the likely hundreds of thousands or millions of

collision checks and cost evaluations need to be computed again, which can take days or weeks of processing time.

A potential multi-query solution that retains the same properties as RRT* is the optimal Probabilistic Roadmap (PRM*) [91]. As discussed in Section 3.2.1.6, this algorithm has a higher space complexity than RRT*, but it stores many more connections between nodes. Nevertheless, the advantages of a multi-query algorithm might outweigh increased memory usage.

To make a PRM* truly multi-query a few changes would need to be made to the conventional algorithm. Typically, 'multi-query' motion planners use the same definition of the costs and constraints for every query, where each query is defined by new start and goal points. If these definitions were to change, each connection in the roadmap would need to be rechecked for collision and reevaluated for cost. To reduce sampling the cost and constraint models, an efficient roadmap would store the relevant information for collision and cost evaluation in each segment. Then constraint violation and cost calculations could be determined through simple operations.

For example, a roadmap for gradient design could store all relevant phase and property information (e.g. maximum fraction of each phase, maximum CTE) in each connecting segment. Then connections that violate constraints (e.g. phase fractions that exceed the allowable) could simply be removed from the roadmap or "turned off" for that query. Similarly, new costs (e.g. a new weighting parameter) could be computed very quickly for each segment in the roadmap if new property models do not need to be sampled. Reducing the expense of new queries will greatly expedite the total design time and could lead to gradient designs that are more aligned with designer or customer preference.

There is an additional, somewhat ambitious benefit of a roadmap paradigm. If general material information is stored in a constructed roadmap, it is plausible that the same roadmap could be used for other gradient design problems. In fact, roadmaps of subspaces could possibly be connected together and to larger spaces to address the aforementioned boundary sampling issue. If roadmaps can made to be generalizable to other gradient design problems and new roadmaps can be partially constructed from subspace roadmaps, then a database of gradient roadmaps could offer powerful

benefits to gradient design. Such a database could be constructed a priori in a large composition space containing all common elements and then searched efficiently for optimal gradient paths. New elements could be added without having to recompute information in any of the old subspaces. However, the combinatorial explosion in memory requirements needed to construct such a database presents a significant challenge.

8.2.2 CALPHAD Modeling

8.2.2.1 Database Assessment

CALPHAD is the fundamental modeling technique underpinning the presented methodology. No other technique can rival CALPHAD's ability to predict phase formation and thermodynamic properties for large state spaces. The accuracy of a CALPHAD database relies on its assessment or comparison to well trusted data like experiments or high fidelity simulations. Multi-component databases that contain four or more elements and are well assessed are rare in the CALPHAD community.

No other database rivals the size and scope of Thermo-Calc's High Entropy Database (TCHEA) [111], which has been used in all of the applications of the presented methodology to date. Such large databases are necessary to almost any gradient design problem because of the typical number of elements involved in any two modern engineering alloys. The third iteration of TCHEA, TCHEA3 [112], contains 26 elements and 400 assessed ternaries. Of those 400, only 136 are assessed in the full range of composition and temperature. However, there are ${}_{26}C_3 = 2600$ possible ternary combinations of 26 elements. This leaves a vast majority of ternaries that have not be assessed against empirical data at all.

8.2.2.2 CALPHAD Uncertainties

The ability of the presented methodology to avoid deleterious phases is fundamentally dependent on the accuracy of the underlying CALPHAD models. As such, the state space of any new gradient design problem should be at least reasonably assessed against empirical data. Unfortunately, the composition space of the periodic table is extremely large and there is unlikely to be

experimental information available for most of arbitrary regions of this space. While new information can be generated from experiments or simulation, some consideration of uncertainty in the planning process is strongly desirable in poorly assessed spaces.

The quantification of uncertainty is of increasing interest to the CALPHAD community [135]. For example, given the parameters of a CALPHAD model, Honarmandi et al. [135] report a method of quantifying phase predictions probabilistically via Markov Chain Monte Carlo methods. These methods require information about the underlying parameters used in the CALPHAD model. Unfortunately, the most accessible and largest CALPHAD databases (e.g. TCHEA) are owned by private companies who are incentivized to keep model parameters as valuable trade secrets. For CAPLHAD uncertainty to be widely applicable in gradient design, these proprietary databases need to also contain uncertainty information or open multi-component databases need to be developed.

The motion planning community has also examined the impact of uncertainty on path planning [136, 137, 138, 139, 140]. By considering phase uncertainty, the optimal problem motion planning problem changes from deterministic to probabilistic. With a probabilistic model for equilibrium phase fraction, the probability that the path does not collide with an obstacle (i.e. lies entirely in free space) can be approximated in a worst-case approach by discretizing the path and computing the maximum probability of producing undesirable phase fractions. This probability can then be compared to a specified threshold to determine constraint violation.

8.2.3 Process Planning

Because material properties can change drastically across a compositionally graded alloy, optimal processing parameters can also vary significantly. This was demonstrated in the gradient from steel to pure tungsten in Chapter 5 and again in the gradient from steel to aluminum in Chapter 6. Optimizing process parameters like laser power, speed, and hatch spacing is often an arduous cycle of trial and error. The ability to predict the optimal processing parameters of a design gradient could greatly expedite alloy development and even realize gradients that might otherwise be essentially impossible to build successfully.

Most of the common defects experienced during additive manufacturing can be predicted from the dimensions of the melt pool. As such, thermal models that can predict melt pool geometry have been shown to be accurate at predicting defects and defect-free regions in processing space (i.e. printability maps) [122]. However, these models are dependent on material properties to predict melt pool parameters for new compositions. Any model that can predict processing parameters for a gradient path will therefore need a model that, given composition, predicts material properties like density, melting temperature, specific heat capacity, thermal conductivity, and absorptivity. Many of these properties (e.g. density, melting temperature, specific heat) can be predicted via CALPHAD techniques [141, 142]. Others may require less accurate analytical models (e.g. rules of mixing), but recent work has shown the promise of predicting material properties, like thermal conductivity [143], with machine learning, provided appropriate physics-based features.

If thermal properties can be predicted as a function of composition, a thermal model can be used to predict melt pool parameters. Many such models exist for powder bed process [122, 144, 145], but few are available for Directed Energy Deposition (DED). The development of a thermal model of the DED process is the main barrier to process prediction in compositionally graded alloys.

Once a model chain is created that can predict defection formation, the processing space (e.g. laser power and speed) can be explored to find the region that is expected to be defect-free. If the thermal model is computationally inexpensive, a gridded sampling of processing parameters can map the defect-free region. The centroid of this region then approximates process parameters that are robust to defect formation. Parameters can be predicted in this way as a post-processing step for a designed gradient or, if models are fast enough, proccessing could even be incorporated into the gradient design problem formulation or state space.

8.2.4 Integration with Part Design

The ultimate goal of designing functional gradients between materials is to leverage them in the design of novel multi-material parts. While the current methodology just designs the gradient material itself, designed gradients could be incorporated into a part design strategy to optimize a functionally graded metal part for part-scale objectives.

Many design optimization techniques have been developed to optimize the material distribution of an FGM within a part of fixed geometry [12, 13, 25]. Methods have also been developed to optimize material distribution and part geometry simultaneously [146, 147, 148, 149]. These methods, referred to as Multi-Material Topology Optimization (MMTO) [147], utilize all design freedoms afforded by additive manufacturing to produce truly optimal functionally graded parts.

MMTO methods can be discrete, where a finite number of distinct materials are optimally placed, or continuous, where the material composition becomes a spatial design variable. Continuous MMTO methods [146, 149] typically assume only two materials are mixed and the properties of the gradient are dependent on just one variable: the volume fraction ratio. Despite this apparent difference from non-linear gradient alloys, these methods can be extended to more complicated compositional gradients by replacing the volume fraction variable with path index.

While material properties along linearly mixed gradients of polymers or ceramics can and have been modeled relatively simply [146, 149], they will likely vary in a much more complicated manner for compositionally graded alloys. It is unclear what forms of the property profile these methods are well suited for. However, as discussed in Section 7.1, if a property varies monotonically with path index along a gradient path it can be transformed into a linear profile and vice versa. As such, the MMTO method can be applied assuming properties vary linearly with path index and a post-processing step can transform the optimized distribution of the path index variable into the true path index. Integrating the design of compositional gradients with the part-scale optimization of material distribution and topology will create a truly end-to-end framework for the design of functionally graded metal parts.

REFERENCES

[1] D. C. Hofmann, J. Kolodziejska, S. Roberts, R. Otis, R. P. Dillon, J.-O. Suh, Z.-K. Liu, and J.-P. Borgonia, "Compositionally graded metals: A new frontier of additive manufacturing," *Journal of Materials Research*, vol. 29, no. 17, pp. 1899–1910, 2014.

[2] O. V. Eliseeva, T. Kirk, P. Samimi, R. Malak, R. Arróyave, A. Elwany, and I. Karaman, "Functionally Graded Materials through robotics-inspired path planning," *Materials & Design*, vol. 182, p. 107975, Nov. 2019.

[3] O. Adiyatov and H. Varol, "Rapidly-exploring random tree based memory efficient motion planning," in *Mechatronics and Automation (ICMA), 2013 IEEE International Conference on*, pp. 354–359, 2013.

[4] T. Kirk, E. Galvan, R. Malak, and R. Arroyave, "Computational Design of Gradient Paths in Additively Manufactured Functionally Graded Materials," *Journal of Mechanical Design*, vol. 140, Nov. 2018.

[5] E. Galvan, R. J. Malak, S. Gibbons, and R. Arroyave, "A Constraint Satisfaction Algorithm for the Generalized Inverse Phase Stability Problem," *Journal of Mechanical Design*, vol. 139, no. 1, p. 011401, 2017.

[6] T. Kirk, R. Malak, and R. Arroyave, "Computational design of compositionally graded alloys for property monotonicity," *Journal of Mechanical Design*, vol. 143, no. 3, 2021.

[7] N. Oxman, "Variable property rapid prototyping," *Virtual and Physical Prototyping*, vol. 6, pp. 3–31, Mar. 2011.

[8] M. Niino, A. Suzuki, T. Hirai, R. Watanabe, T. Hirano, and N. Kuroishi, "Method of producing a functionally gradient material," June 1988.

[9] M. Koizumi and M. Niino, "Overview of FGM Research in Japan," *MRS Bulletin*, vol. 20, pp. 19–21, Jan. 1995.

[10] M. Vaezi, S. Chianrabutra, B. Mellor, and S. Yang, "Multiple material additive manufacturing – Part 1: a review," *Virtual and Physical Prototyping*, vol. 8, pp. 19–50, Mar. 2013.

[11] D. Mahmoud and M. A. Elbestawi, "Lattice Structures and Functionally Graded Materials Applications in Additive Manufacturing of Orthopedic Implants: A Review," *Journal of Manufacturing and Materials Processing*, vol. 1, p. 13, Dec. 2017.

[12] S. Tammas-Williams and I. Todd, "Design for additive manufacturing with site-specific properties in metals and alloys," *Scripta Materialia*, vol. 135, pp. 105–110, July 2017.

[13] G. H. Loh, E. Pei, D. Harrison, and M. D. Monzón, "An overview of functionally graded additive manufacturing," *Additive Manufacturing*, vol. 23, pp. 34–44, Oct. 2018.

[14] A. Bandyopadhyay and B. Heer, "Additive manufacturing of multi-material structures," *Materials Science and Engineering: R: Reports*, vol. 129, pp. 1–16, July 2018.

[15] T. A. Schaedler and W. B. Carter, "Architected Cellular Materials," *Annual Review of Materials Research*, vol. 46, no. 1, pp. 187–210, 2016.

[16] A. Mortensen and S. Suresh, "Functionally graded metals and metal-ceramic composites: Part 1 Processing," *International Materials Reviews*, vol. 40, pp. 239–265, Jan. 1995.

[17] S. Suresh and A. Mortensen, "Functionally graded metals and metal-ceramic composites: Part 2 Thermomechanical behaviour," *International Materials Reviews*, vol. 42, pp. 85–116, Jan. 1997.

[18] Y. Miyamoto, W. A. Kaysser, B. H. Rabin, A. Kawasaki, and R. G. Ford, *Functionally Graded Materials: Design, Processing and Applications*. Springer Science & Business Media, Nov. 2013.

[19] J. J. Sobczak and L. Drenchev, "Metallic Functionally Graded Materials: A Specific Class of Advanced Composites," *Journal of Materials Science & Technology*, vol. 29, pp. 297–316, Apr. 2013.

[20] F. Erdogan, "Fracture Mechanics of Functionally Graded Materials," *MRS Bulletin*, vol. 20, pp. 43–44, Jan. 1995.

[21] J. N. Reddy, "Analysis of functionally graded plates," *International Journal for Numerical Methods in Engineering*, vol. 47, no. 1-3, pp. 663–684, 2000.

[22] A. J. Markworth and J. H. Saunders, "A model of structure optimization for a functionally graded material," *Materials Letters*, vol. 22, pp. 103–107, Jan. 1995.

[23] J. Huang, G. M. Fadel, V. Y. Blouin, and M. Grujicic, "Bi-objective optimization design of functionally gradient materials," *Materials & Design*, vol. 23, pp. 657–666, Oct. 2002.

[24] J. R. Cho and D. Y. Ha, "Optimal tailoring of 2D volume-fraction distributions for heat-resisting functionally graded materials using FDM," *Computer Methods in Applied Mechanics and Engineering*, vol. 191, pp. 3195–3211, May 2002.

[25] V. Birman and L. W. Byrd, "Modeling and Analysis of Functionally Graded Materials and Structures," *Applied Mechanics Reviews*, vol. 60, pp. 195–216, Sept. 2007.

[26] X. Y. Kou and S. T. Tan, "A systematic approach for Integrated Computer-Aided Design and Finite Element Analysis of Functionally-Graded-Material objects," *Materials & Design*, vol. 28, pp. 2549–2565, Jan. 2007.

[27] X. Y. Kou, G. T. Parks, and S. T. Tan, "Optimal design of functionally graded materials using a procedural model and particle swarm optimization," *Computer-Aided Design*, vol. 44, pp. 300–310, Apr. 2012.

[28] M. Mott and J. R. G. Evans, "Zirconia/alumina functionally graded material made by ceramic ink jet printing," *Materials Science and Engineering: A*, vol. 271, pp. 344–352, Nov. 1999.

[29] M. M. Mohebi and J. R. G. Evans, "A Drop-on-Demand Ink-Jet Printer for Combinatorial Libraries and Functionally Graded Ceramics," *Journal of Combinatorial Chemistry*, vol. 4, pp. 267–274, July 2002.

[30] M. C. Leu, B. K. Deuser, L. Tang, R. G. Landers, G. E. Hilmas, and J. L. Watts, "Freeze-form extrusion fabrication of functionally graded materials," *CIRP Annals*, vol. 61, pp. 223–226, Jan. 2012.

[31] C. Petit, L. Montanaro, and P. Palmero, "Functionally graded ceramics for biomedical application: Concept, manufacturing, and properties," *International Journal of Applied Ceramic Technology*, vol. 15, no. 4, pp. 820–840, 2018.

[32] H. Chung and S. Das, "Functionally graded Nylon-11/silica nanocomposites produced by selective laser sintering," *Materials Science and Engineering: A*, vol. 487, pp. 251–257, July 2008.

[33] C. Zhou, Y. Chen, Z. Yang, and B. Khoshnevis, "Digital material fabrication using mask-image-projection-based stereolithography," *Rapid Prototyping Journal*, vol. 19, pp. 153–165, Jan. 2013.

[34] N. A. Meisel, D. A. Dillard, and C. B. Williams, "Impact of material concentration and distribution on composite parts manufactured via multi-material jetting," *Rapid Prototyping Journal*, vol. 24, pp. 872–879, Jan. 2018.

[35] L. J. Gibson and M. F. Ashby, *Cellular Solids: Structure and Properties*. Cambridge University Press, July 1999.

[36] T. C. Lim, "Functionally graded beam for attaining Poisson-curving," *Journal of Materials Science Letters*, vol. 21, pp. 1899–1901, Dec. 2002.

[37] A. Ajdari, P. Canavan, H. Nayeb-Hashemi, and G. Warner, "Mechanical properties of functionally graded 2-D cellular structures: A finite element simulation," *Materials Science and Engineering: A*, vol. 499, pp. 434–439, Jan. 2009.

[38] N. Sudarmadji, J. Y. Tan, K. F. Leong, C. K. Chua, and Y. T. Loh, "Investigation of the mechanical properties and porosity relationships in selective laser-sintered polyhedral for functionally graded scaffolds," *Acta Biomaterialia*, vol. 7, pp. 530–537, Feb. 2011.

[39] C. Lira, F. Scarpa, and R. Rajasekaran, "A Gradient Cellular Core for Aeroengine Fan Blades Based on Auxetic Configurations:," *Journal of Intelligent Material Systems and Structures*, July 2011.

[40] S. Arabnejad Khanoki and D. Pasini, "Multiscale Design and Multiobjective Optimization of Orthopedic Hip Implants with Functionally Graded Cellular Material," *Journal of Biomechanical Engineering*, vol. 134, Mar. 2012.

[41] H. Niknam, A. H. Akbarzadeh, D. Rodrigue, and D. Therriault, "Architected multidirectional functionally graded cellular plates," *Materials & Design*, vol. 148, pp. 188–202, June 2018.

[42] L. Li, Q. Sun, C. Bellehumeur, and P. Gu, "Composite Modeling and Analysis for Fabrication of FDM Prototypes with Locally Controlled Properties," *Journal of Manufacturing Processes*, vol. 4, pp. 129–141, Jan. 2002.

[43] M. Srivastava, S. Maheshwari, and T. K. Kundra, "Virtual Modelling and Simulation of Functionally Graded Material Component using FDM Technique," *Materials Today: Proceedings*, vol. 2, pp. 3471–3480, Jan. 2015.

[44] J. C. Steuben, A. P. Iliopoulos, and J. G. Michopoulos, "Implicit slicing for functionally tailored additive manufacturing," *Computer-Aided Design*, vol. 77, pp. 107–119, Aug. 2016.

[45] J. J. Lewandowski and M. Seifi, "Metal Additive Manufacturing: A Review of Mechanical Properties," *Annual Review of Materials Research*, vol. 46, no. 1, pp. 151–186, 2016.

[46] F. A. List, R. R. Dehoff, L. E. Lowe, and W. J. Sames, "Properties of Inconel 625 mesh structures grown by electron beam additive manufacturing," *Materials Science and Engineering: A*, vol. 615, pp. 191–197, Oct. 2014.

[47] T. Traini, C. Mangano, R. L. Sammons, F. Mangano, A. Macchi, and A. Piattelli, "Direct laser metal sintering as a new approach to fabrication of an isoelastic functionally graded material for manufacture of porous titanium dental implants," *Dental Materials*, vol. 24, pp. 1525–1533, Nov. 2008.

[48] C. D. Lundin, "Dissimilar Metal Welds— Transition Joints Literature Review," *Welding Journal*, vol. 61, pp. 58–63, Feb. 1982.

[49] Z. Sun and J. C. Ion, "Laser welding of dissimilar metal combinations," *Journal of Materials Science*, vol. 30, pp. 4205–4214, Sept. 1995.

[50] J. N. DuPont, "Microstructural evolution and high temperature failure of ferritic to austenitic dissimilar welds," *International Materials Reviews*, vol. 57, pp. 208–234, July 2012.

[51] J. Singh, K. S. Arora, and D. K. Shukla, "Dissimilar MIG-CMT weld-brazing of aluminium to steel: A review," *Journal of Alloys and Compounds*, vol. 783, pp. 753–764, Apr. 2019.

[52] R. Vilar, "Laser cladding," *Journal of Laser Applications*, vol. 11, pp. 64–79, Mar. 1999.

[53] L. Santo, "Laser cladding of metals: a review," *International Journal of Surface Science and Engineering*, vol. 2, pp. 327–336, Jan. 2008.

[54] S. Kaierle, A. Barroi, C. Noelke, J. Hermsdorf, L. Overmeyer, and H. Haferkamp, "Review on Laser Deposition Welding: From Micro to Macro," *Physics Procedia*, vol. 39, pp. 336–345, Jan. 2012.

[55] K. I. Schwendner, R. Banerjee, P. C. Collins, C. A. Brice, and H. L. Fraser, "Direct laser deposition of alloys from elemental powder blends," *Scripta Materialia*, vol. 45, no. 10, pp. 1123–1129, 2001.

[56] P. C. Collins, R. Banerjee, S. Banerjee, and H. L. Fraser, "Laser deposition of compositionally graded titanium–vanadium and titanium–molybdenum alloys," *Materials Science and Engineering: A*, vol. 352, pp. 118–128, July 2003.

[57] R. Banerjee, P. C. Collins, D. Bhattacharyya, S. Banerjee, and H. L. Fraser, "Microstructural evolution in laser deposited compositionally graded / titanium-vanadium alloys," *Acta Materialia*, vol. 51, pp. 3277–3292, June 2003.

[58] D. C. Hofmann, S. Roberts, R. Otis, J. Kolodziejska, R. P. Dillon, J.-o. Suh, A. A. Shapiro, Z.-K. Liu, and J.-P. Borgonia, "Developing gradient metal alloys through radial deposition additive manufacturing," *Scientific reports*, vol. 4, p. 5357, 2014.

[59] B. E. Carroll, R. A. Otis, J. P. Borgonia, J.-o. Suh, R. P. Dillon, A. A. Shapiro, D. C. Hofmann, Z.-K. Liu, and A. M. Beese, "Functionally graded material of 304L stainless steel and inconel 625 fabricated by directed energy deposition: Characterization and thermodynamic modeling," *Acta Materialia*, vol. 108, pp. 46–54, 2016.

[60] B. Chen, Y. Su, Z. Xie, C. Tan, and J. Feng, "Development and characterization of 316L/Inconel625 functionally graded material fabricated by laser direct metal deposition," *Optics & Laser Technology*, vol. 123, p. 105916, Mar. 2020.

[61] L. D. Bobbio, R. A. Otis, J. P. Borgonia, R. P. Dillon, A. A. Shapiro, Z.-K. Liu, and A. M. Beese, "Additive manufacturing of a functionally graded material from Ti-6Al-4V to Invar: Experimental characterization and thermodynamic calculations," *Acta Materialia*, vol. 127, pp. 133–142, 2017.

[62] W. Meng, Y. Xiaohui, W. Zhang, F. Junfei, G. Lijie, M. Qunshuang, and C. Bing, "Additive manufacturing of a functionally graded material from Inconel625 to Ti6Al4V by laser synchronous preheating," *Journal of Materials Processing Technology*, vol. 275, p. 116368, Jan. 2020.

[63] A. Reichardt, R. P. Dillon, J. P. Borgonia, A. A. Shapiro, B. W. McEnerney, T. Momose, and P. Hosemann, "Development and characterization of Ti-6Al-4V to 304L stainless steel gradient components fabricated with laser deposition additive manufacturing," *Materials & Design*, vol. 104, pp. 404–413, 2016.

[64] A. Reichardt, A. A. Shapiro, R. Otis, R. P. Dillon, J. P. Borgonia, B. W. McEnerney, P. Hosemann, and A. M. Beese, "Advances in additive manufacturing of metal-based functionally graded materials," *International Materials Reviews*, vol. 0, pp. 1–29, Jan. 2020.

[65] L. Yan, Y. Chen, and F. Liou, "Additive manufacturing of functionally graded metallic materials using laser metal deposition," *Additive Manufacturing*, vol. 31, p. 100901, Jan. 2020.

[66] D. Wu, X. Liang, Q. Li, and L. Jiang, "Laser Rapid Manufacturing of Stainless Steel 316L/Inconel718 Functionally Graded Materials: Microstructure Evolution and Mechanical Properties," Jan. 2011.

[67] K. Shah, I. u. Haq, A. Khan, S. A. Shah, M. Khan, and A. J. Pinkerton, "Parametric study of development of Inconel-steel functionally graded materials by laser direct metal deposition," *Materials & Design (1980-2015)*, vol. 54, pp. 531–538, Feb. 2014.

[68] B. Onuike, B. Heer, and A. Bandyopadhyay, "Additive manufacturing of Inconel 718—Copper alloy bimetallic structure using laser engineered net shaping (LENS™)," *Additive Manufacturing*, vol. 21, pp. 133–140, May 2018.

[69] Q. M. Nguyen and S.-C. Huang, "An Investigation of the Microstructure of an Intermetallic Layer in Welding Aluminum Alloys to Steel by MIG Process," *Materials*, vol. 8, pp. 8246–8254, Dec. 2015.

[70] D. Zhang, S. Sun, D. Qiu, M. A. Gibson, M. S. Dargusch, M. Brandt, M. Qian, and M. Easton, "Metal Alloys for Fusion-Based Additive Manufacturing," *Advanced Engineering Materials*, vol. 20, no. 5, p. 1700952, 2018.

[71] J. Zhang, B. Song, Q. Wei, D. Bourell, and Y. Shi, "A review of selective laser melting of aluminum alloys: Processing, microstructure, property and developing trends," *Journal of Materials Science & Technology*, vol. 35, pp. 270–284, Feb. 2019.

[72] T. Mukherjee, J. S. Zuback, A. De, and T. DebRoy, "Printability of alloys for additive manufacturing," *Scientific Reports*, vol. 6, p. 19717, Jan. 2016.

[73] M. A. Easton, M. A. Gibson, S. Zhu, and T. B. Abbott, "An A Priori Hot-Tearing Indicator Applied to Die-Cast Magnesium-Rare Earth Alloys," *Metallurgical and Materials Transactions A*, vol. 45, pp. 3586–3595, July 2014.

[74] Z. Sun, X. P. Tan, M. Descoins, D. Mangelinck, S. B. Tor, and C. S. Lim, "Revealing hot tearing mechanism for an additively manufactured high-entropy alloy via selective laser melting," *Scripta Materialia*, vol. 168, pp. 129–133, July 2019.

[75] M. J. Benoit, S. M. Zhu, T. B. Abbott, and M. A. Easton, "Evaluation of the Effect of Rare Earth Alloying Additions on the Hot Tearing Susceptibility of Aluminum Alloy 7150 During Rapid Solidification," *Metallurgical and Materials Transactions A*, vol. 51, pp. 5213–5227, Oct. 2020.

[76] Y. Fang, X. Jiang, D. Mo, D. Zhu, and Z. Luo, "A review on dissimilar metals' welding methods and mechanisms with interlayer," *The International Journal of Advanced Manufacturing Technology*, vol. 102, pp. 2845–2863, June 2019.

[77] N. Özdemir and B. Bilgin, "Interfacial properties of diffusion bonded Ti-6Al-4V to AISI 304 stainless steel by inserting a Cu interlayer," *The International Journal of Advanced Manufacturing Technology*, vol. 41, pp. 519–526, Mar. 2009.

[78] I. Tomashchuk, P. Sallamand, N. Belyavina, and M. Pilloz, "Evolution of microstructures and mechanical properties during dissimilar electron beam welding of titanium alloy to stainless steel via copper interlayer," *Materials Science and Engineering: A*, vol. 585, pp. 114–122, Nov. 2013.

[79] D. Yongqiang, S. Guangmin, and Y. Lijing, "Impulse Pressuring Diffusion Bonding of Titanium to Stainless Steel Using a Copper Interlayer," *Rare Metal Materials and Engineering*, vol. 44, pp. 1041–1045, May 2015.

[80] X. Dai, H. Zhang, H. Zhang, J. Liu, and J. Feng, "Arc assisted ultrasonic seam welding of Mg/Al joints with Zn interlayer," *Materials Science and Technology*, vol. 32, pp. 164–172, Jan. 2016.

[81] Q. Gao and K. Wang, "Influence of Zn Interlayer on Interfacial Microstructure and Mechanical Properties of TIG Lap-Welded Mg/Al Joints," *Journal of Materials Engineering and Performance*, vol. 25, pp. 756–763, Mar. 2016.

[82] L. Kaufman and J. Agren, "CALPHAD, first and second generation–Birth of the materials genome," *Scripta Materialia*, vol. 70, pp. 3–6, 2014.

[83] L. Kaufman and M. Cohen, "The Martensitic Transformation in the Iron-Nickel System," *JOM*, vol. 8, pp. 1393–1401, Oct. 1956.

[84] A. R. Moustafa, A. Durga, G. Lindwall, and Z. C. Cordero, "Scheil ternary projection (STeP) diagrams for designing additively manufactured functionally graded metals," *Additive Manufacturing*, vol. 32, p. 101008, Mar. 2020.

[85] E. Scheil, "Bemerkungen zur schichtkristallbildung," *Zeitschrift für Metallkunde*, vol. 34, no. 3, pp. 70–72, 1942.

[86] B. Bocklund, L. D. Bobbio, R. A. Otis, A. M. Beese, and Z.-K. Liu, "Scheil-Gulliver simulations for the design of functionally graded alloys by additive manufacturing using pycalphad," *arXiv:2001.11611 [cond-mat]*, Jan. 2020.

[87] T. Lozano-Pérez and M. A. Wesley, "An algorithm for planning collision-free paths among polyhedral obstacles," *Communications of the ACM*, vol. 22, no. 10, pp. 560–570, 1979.

[88] E. Masehian and D. Sedighizadeh, "Classic and Heuristic Approaches in Robot Motion Planning A Chronological Review," vol. 1, no. 5, p. 6, 2007.

[89] T. T. Mac, C. Copot, D. T. Tran, and R. De Keyser, "Heuristic approaches in robot path planning: A survey," *Robotics and Autonomous Systems*, vol. 86, pp. 13–28, 2016.

[90] S. M. LaValle, *Planning Algorithms*. Cambridge University Press, May 2006.

[91] S. Karaman and E. Frazzoli, "Sampling-based algorithms for optimal motion planning," *The international journal of robotics research*, vol. 30, no. 7, pp. 846–894, 2011.

[92] Y. K. Hwang and N. Ahuja, "Gross motion planning—a survey," *ACM Computing Surveys*, vol. 24, pp. 219–291, Sept. 1992.

[93] J. M. Porta, L. Jaillet, and O. Bohigas, "Randomized path planning on manifolds based on higher-dimensional continuation," *The International Journal of Robotics Research*, vol. 31, pp. 201–215, Feb. 2012.

[94] D. Koditschek, "Robot Planning and Control Via Potential Functions," *The Robotics Review*, pp. 349–367, Jan. 1989.

[95] M. Zacksenhouse, R. deFigueiredo, and D. Johnson, "A neural network architecture for cue-based motion planning," in *Proceedings of the 27th IEEE Conference on Decision and Control*, (Austin, TX, USA), pp. 324–327, IEEE, 1988.

[96] R. Meyes, H. Tercan, S. Roggendorf, T. Thiele, C. Büscher, M. Obdenbusch, C. Brecher, S. Jeschke, and T. Meisen, "Motion Planning for Industrial Robots using Reinforcement Learning," *Procedia CIRP*, vol. 63, pp. 107–112, Jan. 2017.

[97] D. González, J. Pérez, V. Milanés, and F. Nashashibi, "A Review of Motion Planning Techniques for Automated Vehicles," *IEEE Transactions on Intelligent Transportation Systems*, vol. 17, pp. 1135–1145, Apr. 2016. Conference Name: IEEE Transactions on Intelligent Transportation Systems.

[98] A. Piazzi, C. Lo Bianco, M. Bertozzi, A. Fascioli, and A. Broggi, "Quintic G/sup 2/-splines for the iterative steering of vision-based autonomous vehicles," *IEEE Transactions on Intelligent Transportation Systems*, vol. 3, pp. 27–36, Mar. 2002. Conference Name: IEEE Transactions on Intelligent Transportation Systems.

[99] J.-W. Lee and B. Litkouhi, "A unified framework of the automated lane centering/changing control for motion smoothness adaptation," in *2012 15th International IEEE Conference on Intelligent Transportation Systems*, pp. 282–287, Sept. 2012. ISSN: 2153-0017.

[100] Z. Liang, G. Zheng, and J. Li, "Automatic parking path optimization based on Bezier curve fitting," in *2012 IEEE International Conference on Automation and Logistics*, pp. 583–587, Aug. 2012. ISSN: 2161-816X.

[101] Y. Hu and S. Yang, "A knowledge based genetic algorithm for path planning of a mobile robot," in *IEEE International Conference on Robotics and Automation, 2004. Proceedings. ICRA '04. 2004*, vol. 5, pp. 4350–4355 Vol.5, Apr. 2004. ISSN: 1050-4729.

[102] E. W. Dijkstra and others, "A note on two problems in connexion with graphs," *Numerische mathematik*, vol. 1, no. 1, pp. 269–271, 1959.

[103] M. Elbanhawi and M. Simic, "Sampling-based robot motion planning: A review," *IEEE Access*, vol. 2, pp. 56–77, 2014.

[104] I. Al-Bluwi, T. Siméon, and J. Cortés, "Motion planning algorithms for molecular simulations: A survey," *Computer Science Review*, vol. 6, pp. 125–143, July 2012.

[105] N. M. Amato and G. Song, "Using Motion Planning to Study Protein Folding Pathways," *Journal of Computational Biology*, vol. 9, pp. 149–168, Apr. 2002.

[106] J. Cortés, T. Siméon, M. Remaud-Siméon, and V. Tran, "Geometric algorithms for the conformational analysis of long protein loops," *Journal of Computational Chemistry*, vol. 25, no. 7, pp. 956–967, 2004.

[107] D. Guieysse, J. Cortés, S. Puech-Guenot, S. Barbe, V. Lafaquière, P. Monsan, T. Siméon, I. André, and M. Remaud-Siméon, "A Structure-Controlled Investigation of Lipase Enantioselectivity by a Path-Planning Approach," *ChemBioChem*, vol. 9, pp. 1308–1317, May 2008.

[108] A. Woronow, "Generating random numbers on a simplex," *Computers & Geosciences*, vol. 19, pp. 81–88, Jan. 1993.

[109] R. A. Otis, *Software architecture for CALPHAD modeling of phase stability and transformations in alloy additive manufacturing processes*. PhD thesis, June 2016.

[110] J.-O. Andersson, T. Helander, L. Höglund, P. Shi, and B. Sundman, "Thermo-Calc & DICTRA, computational tools for materials science," *Calphad*, vol. 26, no. 2, pp. 273–312, 2002.

[111] H. Mao, H.-L. Chen, and Q. Chen, "TCHEA1: A Thermodynamic Database Not Limited for "High Entropy" Alloys," *Journal of Phase Equilibria and Diffusion*, vol. 38, no. 4, pp. 353–368, 2017.

[112] "TCHEA3: TCS High Entropy Alloy Database Extended Information Sheet."

[113] A. Abu-Odeh, E. Galvan, T. Kirk, H. Mao, Q. Chen, P. Mason, R. Malak, and R. Arroyave, "Exploration of the High Entropy Alloy Space as a Constraint Satisfaction Problem," *arXiv preprint arXiv:1712.02442*, 2017.

[114] D. M. Tax and R. P. Duin, "Support vector domain description," *Pattern recognition letters*, vol. 20, no. 11-13, pp. 1191–1199, 1999.

[115] V. Vapnik, *The Nature of Statistical Learning Theory*. Springer, New York, 1995.

[116] B. Schölkopf and A. J. Smola, *Learning with kernels: support vector machines, regularization, optimization, and beyond*. MIT Press, Cambridge, MA, 2002.

[117] J. Hou, J. Guo, L. Zhou, and H. Ye, "Sigma phase formation and its effect on mechanical properties in the corrosion-resistant superalloy K44," *Zeitschrift für Metallkunde*, vol. 97, no. 2, pp. 174–181, 2006.

[118] C.-C. Hsieh and W. Wu, "Overview of Intermetallic Sigma Phase Precipitation in Stainless Steels," *ISRN Metallurgy*, vol. 2012, 2012.

[119] D. C. Montgomery, *Design and analysis of experiments*. John Wiley & Sons, 2017.

[120] D. M. Powers, "Evaluation: from precision, recall and F-measure to ROC, informedness, markedness and correlation," *Journal of Machine Learning Technologies*, vol. 2, no. 1, pp. 37–63, 2011.

[121] J. Denny, E. Greco, S. Thomas, and N. M. Amato, "MARRT: Medial Axis biased rapidly-exploring random trees," in *Robotics and Automation (ICRA), 2014 IEEE International Conference on*, pp. 90–97, IEEE, 2014.

[122] L. Johnson, M. Mahmoudi, B. Zhang, R. Seede, X. Huang, J. T. Maier, H. J. Maier, I. Karaman, A. Elwany, and R. Arróyave, "Assessing printability maps in additive manufacturing of metal alloys," *Acta Materialia*, vol. 176, pp. 199–210, Sept. 2019.

[123] C. Olivier, C. Yvan, and B. Michel, "Hot Tearing in Steels During Solidification: Experimental Characterization and Thermomechanical Modeling," *Journal of Engineering Materials and Technology*, vol. 130, Apr. 2008.

[124] T. Clyne and G. Davies, "Comparison between experimental data and theoretical predictions relating to dependence of solidification cracking on composition," in *Solidification and Casting of Metals*, pp. 275–278, 1979.

[125] S. Kou, "A criterion for cracking during solidification," *Acta Materialia*, vol. 88, pp. 366–374, Apr. 2015.

[126] M. Dehghani, A. Amadeh, and S. A. A. Akbari Mousavi, "Investigations on the effects of friction stir welding parameters on intermetallic and defect formation in joining aluminum alloy to mild steel," *Materials & Design*, vol. 49, pp. 433–441, Aug. 2013.

[127] Z. Lu, N. Wei, P. Li, C. Guo, and F. Jiang, "Microstructure and mechanical properties of intermetallic Al3Ti alloy with residual aluminum," *Materials & Design*, vol. 110, pp. 466–474, Nov. 2016.

[128] J. M. Vitek, "G-phase formation in aged type 308 stainless steel," *Metallurgical Transactions A*, vol. 18, pp. 154–156, Jan. 1987.

[129] A. Mateo, L. Llanes, M. Anglada, A. Redjaimia, and G. Metauer, "Characterization of the intermetallic G-phase in an AISI 329 duplex stainless steel," *Journal of Materials Science*, vol. 32, pp. 4533–4540, Sept. 1997.

[130] Y. Matsukawa, T. Takeuchi, Y. Kakubo, T. Suzudo, H. Watanabe, H. Abe, T. Toyama, and Y. Nagai, "The two-step nucleation of G-phase in ferrite," *Acta Materialia*, vol. 116, pp. 104–113, Sept. 2016.

[131] "TCHEA2: TCS High Entropy Alloy Database Extended Information Sheet."

[132] Y. Davydov and R. Zitikis, "Quantifying non-monotonicity of functions and the lack of positivity in signed measures," *Modern Stochastics: Theory and Applications*, vol. 4, pp. 219–231, Sept. 2017.

[133] A. P. Gulyaev and I. K. Kupalova, "Effect of cobalt on the structure and properties of high-speed steels," *Metal Science and Heat Treatment*, vol. 12, pp. 666–671, Aug. 1970.

[134] D. J. Kereiakes, D. A. Cox, J. B. Hermiller, M. G. Midei, W. B. Bachinsky, E. D. Nukta, M. B. Leon, S. Fink, L. Marin, and A. J. Lansky, "Usefulness of a cobalt chromium coronary stent alloy," *The American Journal of Cardiology*, vol. 92, pp. 463–466, Aug. 2003.

[135] P. Honarmandi, N. H. Paulson, R. Arróyave, and M. Stan, "Uncertainty quantification and propagation in CALPHAD modeling," *Modelling and Simulation in Materials Science and Engineering*, vol. 27, p. 034003, Mar. 2019.

[136] S. M. LaValle and S. A. Hutchinson, "An Objective-Based Framework for Motion Planning under Sensing and Control Uncertainties," *The International Journal of Robotics Research*, vol. 17, pp. 19–42, Jan. 1998.

[137] M. Ono and B. C. Williams, "An efficient motion planning algorithm for stochastic dynamic systems with constraints on probability of failure," in *In Proceedings of AAAI-08*, 2008.

[138] A. Bry and N. Roy, "Rapidly-exploring Random Belief Trees for motion planning under uncertainty," in *2011 IEEE International Conference on Robotics and Automation*, pp. 723–730, May 2011.

[139] S. Prentice and N. Roy, "The Belief Roadmap: Efficient Planning in Linear POMDPs by Factoring the Covariance," in *Robotics Research* (M. Kaneko and Y. Nakamura, eds.), Springer Tracts in Advanced Robotics, pp. 293–305, Springer Berlin Heidelberg, 2011.

[140] J. van den Berg, S. Patil, and R. Alterovitz, "Motion planning under uncertainty using iterative local optimization in belief space," *The International Journal of Robotics Research*, vol. 31, pp. 1263–1278, Sept. 2012.

[141] J. Smith, W. Xiong, J. Cao, and W. K. Liu, "Thermodynamically consistent microstructure prediction of additively manufactured materials," *Computational Mechanics*, vol. 57, pp. 359–370, Mar. 2016.

[142] T. Keller, G. Lindwall, S. Ghosh, L. Ma, B. M. Lane, F. Zhang, U. R. Kattner, E. A. Lass, J. C. Heigel, Y. Idell, M. E. Williams, A. J. Allen, J. E. Guyer, and L. E. Levine, "Application of finite element, phase-field, and CALPHAD-based methods to additive manufacturing of Ni-based superalloys," *Acta Materialia*, vol. 139, pp. 244–253, Oct. 2017.

[143] M. W. Gaultois, A. O. Oliynyk, A. Mar, T. D. Sparks, G. J. Mulholland, and B. Meredig, "Perspective: Web-based machine learning models for real-time screening of thermoelectric materials properties," *APL Materials*, vol. 4, p. 053213, May 2016.

[144] J. C. Steuben, A. J. Birnbaum, J. G. Michopoulos, and A. P. Iliopoulos, "Enriched analytical solutions for additive manufacturing modeling and simulation," *Additive Manufacturing*, vol. 25, pp. 437–447, Jan. 2019.

[145] A. M. Rubenchik, W. E. King, and S. S. Wu, "Scaling laws for the additive manufacturing," *Journal of Materials Processing Technology*, vol. 257, pp. 234–243, July 2018.

[146] Q. Xia and M. Y. Wang, "Simultaneous optimization of the material properties and the topology of functionally graded structures," *Computer-Aided Design*, vol. 40, pp. 660–675, June 2008.

[147] J. D. Hiller and H. Lipson, "Multi Material Topological Optimization of Structures and Mechanisms," in *Proceedings of the 11th Annual Conference on Genetic and Evolutionary Computation*, GECCO '09, (New York, NY, USA), pp. 1521–1528, ACM, 2009.

[148] P. D. Dunning, C. J. Brampton, and H. A. Kim, "Simultaneous optimisation of structural topology and material grading using level set method," *Materials Science and Technology*, vol. 31, pp. 884–894, June 2015.

[149] A. Garland and G. Fadel, "Multi-Objective Optimal Design of Functionally Gradient Materials," American Society of Mechanical Engineers Digital Collection, Dec. 2016.